THESE EN CO - TUTELLE
présentée pour obtenir le grade de
Docteur de l'Université de Lille
en Structure et Dynamique des Systèmes Réactifs

par
Rafal TOMASZEK

SUSPENSION PLASMA SPRAYING OF FUNCTIONAL GRADIENT COATINGS

PROJECTION PAR PLASMA DE SUSPENSION POUR OBTENIR LES DEPOTS FONCTIONNELS A GRADIENT

Version finale
Date de soutenance : 20.09.2006

Directeurs de la Thèse :	Prof. Lech PAWLOWSKI, ENSCL, Villeneuve d'Ascq, France Prof. Jerzy ZDANOWSKI, WUT, Wroclaw, Pologne

Rapporteurs :	Prof. Jacky LESAGE, USTL, Lille Prof. Igor SMUROV, ENISE, Saint Etienne Prof. Aleksandra SOKOLOWSKA, Université Technique de Varsovie

Septembre 2006
Villeneuve d'Ascq

I would like to dedicate this doctoral thesis to my beloved wife Agnieszka and daughter Maja

Acknowledgement

It is with great pleasure that I acknowledge the joint supervision of Professor Lech Pawłowski, Professor Jerzy Zdanowski and Doctor Zbigniew Znamirowski. All of them always found the time to provide me with many hours of fruitful discussions. Their advice and help are appreciated.

The research was mostly carried out in Ecole Nationale Superieure de Chimie de Lille and Laurence Burylo, Martine Frère, Leon Gengembre, Jacky Laureyns, Christel Pierlot are thanked for providing access to experimental equipment.

Rafał Tomaszek

LIST OF ABBREVIATIONS

APS	Atmospheric plasma spraying
EMPA	Electron Probe Micro-Analyser
HAp	Hydroxyapatite
LCD	Liquid Crystal Display
PVS	Pressurized Vessel System
SEM	Scanning Electron Microscope
SOFC	Solid Oxide Fuel Cell
SPPS	Solution Precursor Plasma Spraying
SPS	Suspension Plasma Spraying
TCP	Tri-calcium Phosphate
TTCP	Tetra-calcium Phosphate
YIG	Yttrium Iron Garnet
YSZ	Yttria-Stabilized Zirconia
XPS	X-ray Photoelectron Spectroscopy
XRD	X-ray Diffraction

e	electron charge
E	electric field
h	Planck constant
m	electron mass
I	current intensity
J	current density
α	emitting surface area
β	shape coefficient
V	voltage
Φ	work function
W_a	lowest energy of conduction band
W_w	highest energy of valence band
ζ	Fermi energy

LIST OF FIGURES

LIST OF TABLES

CHAPTER 1

INTRODUCTION

Plasma spraying and related processes within the family of thermal spraying techniques are understood as a deposition of partially or full molten particles on the prepared substrate [1].

The history of thermal spraying dates back to second decade of XXth century with an invention of metallization process by Schoop [2]. However, spraying with use of plasma torch was developed over 40 years later by Giannini and Ducati [3] and Gage *et al.* [4]. Due to its versatility and cost-efficiency, plasma spraying become the leading one among thermal spraying techniques, nowadays gathering 50% of 4.8 billion € worth thermal spray global market [5].

One of the recent developments in materials science and engineering is associated with manufacturing of polycrystalline materials having small crystal sizes. The size of crystal grains plays an important role in many properties. A well known example is *Petch-Hall* law which describes increase of yield strength of alloys and metals with decreasing size of grains. Another possible effect, coming from the area of electronic technology, is an intensification of electron emission from small conduction grains inside a dielectric matrix (Figure 1.1).

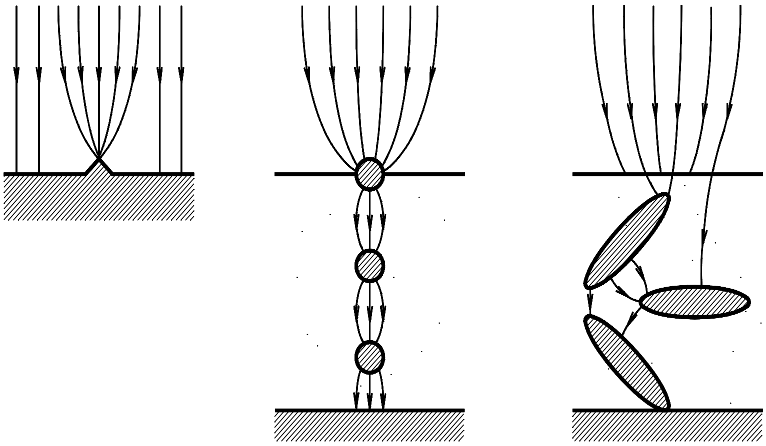

Figure 1.1 Lines of electron emission from conducting grains inside dielectric matrix

The intensification of electron emission results from the formation of local electric field of high intensity that extracts electrons. The field increases its intensity on the surface of very small grains. An adaptation of plasma spraying to obtain materials having such effect can be an interesting alternative for obtaining large area emitters for a relatively cheap price field **[6][7][8]**.

Biomedical coatings are also an example of scientific fields in which nano-structured materials are increasingly tested. The well known application is hydroxyapatite coating onto hip prosthesis (Figure 1.2)

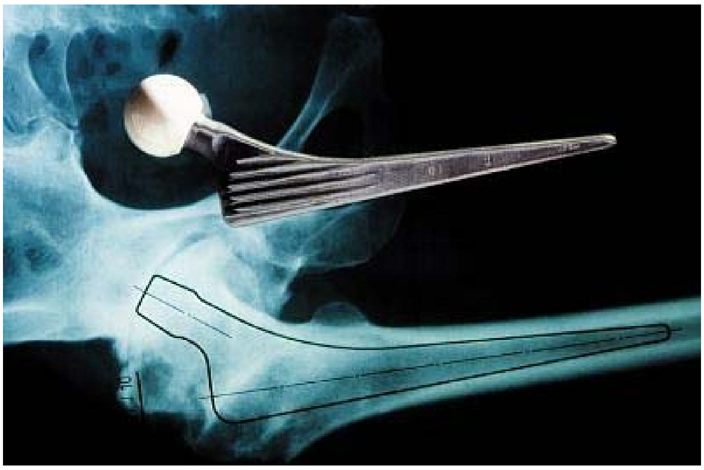

Figure 1.2 Hip prosthesis

The coating is applied onto a part of prosthesis that is implanted into the bone. Hydroxyapatite is used because of its bioactive properties. The coating disappears in some time after the implantation. The influence of grain size onto bioactive properties of hydroxyapatite is not yet well known but an advantage of having relatively thin film of a few tents of micrometers instead of thick film of 150 µm (used industrially) can be indicated. Such a thin film would dissolve in bone in a shorter time.

Moreover, finely structured coatings are expected to present other superior proprieties e.g., mechanical (hardness [9], toughness, wear resistance [10]), chemical (corrosion resistance, photocatalytic efficiency [11]), electrical (performance of electrolyte [12] and electrodes in SOFC[13].

The deposition of fine-grained feedstock with use of conventional pneumatic powder feeders is impossible due to low effectiveness of the process caused by strong agglomeration of the powder leading to poor flowability and insufficient momentum of the particles to penetrate plasma jet. Plasma spray process should be however adapted to produce nano-structured and submicrometer materials.

The main approaches to solve the problem are:

- Spraying of the agglomerates of nanoparticles;
- Spraying the suspensions/solutions

Spraying of the agglomerates has been mainly implemented to ceramic or cermet materials such as: Al_2O_3-TiO_2 studied by Shaw et al. [14], ZrO_2 [15], WC-Co [16].
The problems which are considered for spraying of the agglomerates are:

- the particles geometry: the nanoparticles behave differently depending on their size and shape;
- the selection of powder production method, which influences the microstructure of the powder;
- the plasma spray parameters, which has to carefully selected in order to preserve nanostructure.

The emerging deposition technology of nanostructured materials consists in preparation of the feedstock in form of liquid suspension of submicro/nanometer powder or precursor solution and injection into the plasma. However, handling with suspensions/solutions requires completely new approach to:

- Design of feeding systems, consisting of atomizer, able to generate micrometer sized droplets, and pumping unit sustaining uniform feedstock flow rate during the process.

- Preparation of the feedstock; commercial thermal spray powders with relatively coarse-grained size distribution (>10 µm) are not suitable to form stable suspensions. That is why; the powders have to be mechanically ball milled in order to decrease their size distribution. Additionally, the suspension should contain organic surfactant which absorbed on the powder particles surface prevents the particles agglomeration.

- Selection of plasma spraying parameters; suspension droplets usually contain 80 – 95 wt.% of the solvent which should be completely evaporated in the plasma, which requires relatively high power and high enthalpy of the plasma;

Additionally, suspensions/solutions of different materials can be precisely mixed and dosed with use of specialized pumping systems. The method which uses suspensions as initial material, called suspension plasma spraying, allows to deposit composite coatings with uniform or gradient material composition.

In this thesis, number of aspects related to suspension plasma spraying technology, coatings microstructure as well as its functional properties will be examined. In particular, author will be:

- proposing pressurized vessel based and peristaltic pump based constructions of suspension pumping systems;
- focusing on selection of spraying parameters;
- discussing titania and hydroxyapatite coatings microstructure characterized by SEM, XRD, µ-Raman Spectroscopy, XPS;
- investigating the electron emission and electric conduction mechanism of titania coatings.

CHAPTER 2

PLASMA SPRAYING

2.1. THERMAL SPRAYING TECHNIQUES

Thermal spraying is the family of the processes of the coatings deposition by melting the material into droplets and impinging these droplets on the substrate with use of high temperature source. [1].

Energy source has to fulfil two main conditions :

- should support sufficient amount of thermal energy in order to melt sprayed material,
- should effectively transfer kinetic energy to the material in order to accelerate it towards the substrate.

Through all the thermal spraying techniques, the relation of thermal energy to kinetic energy considerably differ for each technique. For example, plasma spraying is able to support high thermal energy (up to 20000 K) and accelerate the particles up to 300 m/s. On the other hand, in the detonation gun process temperature can reach only 4500 K but the velocity of the particles is relatively higher (up to 900 m/s).

Flame Spraying (FS)

In the flame spraying process, combustion energy of the fuel gas is used to melt the material. The flame temperature can reach up to 3350 K and its velocity up to 100 m/s.

Arc Spraying (AS)

Arc Spraying uses arc discharge energy to melt the electrodes in form of wires made of sprayed material. Molten droplets of the material are then propelled by compressed air onto the substrate. The technology is relatively cheap and simple, however, range of applicable materials is limited to electrically conducting ones.

Detonation Gun (D-gun)

The principles of process are similar to flame spray with the difference that the combustion is ignited in discontinuous mode. The fuel gas, oxygen and a charge of powder are fed into the gun tube. After spark ignition of the mixture, the detonation wave accelerates powder up to about 900 m/s.

High Velocity Oxy-Fuel (HVOF)

In the HVOF process, combustion of fuel gases (e.g. acetylene, kerosene, propane, propylene, etc..) under high pressure generates a high velocity jet, reaching the temperature of about 3400 K and the velocity of 2000 m/s.

Cold Spray

Cold spray process due to low temperature of the particles is questioned if it could be classified as one of thermal spray methods. However, the principle of the process is similar to other thermal spray methods. Cold spray uses the high pressure compressed gas to propel the particles with high velocities up to 1500 m/s.

Plasma Spraying (PS)

Described in details, in further part of the chapter.

2.1.1. Plasma Spraying

Systematics

The process with use of high temperature plasma source is the most developed among the all thermal spray techniques. Due to versatility of plasma based technology, different modifications of the process were developed. The literature of the subject presents general systematics based on process environment-atmosphere:

- Atmospheric Plasma Spraying (APS),
- Vacuum Plasma Spraying (VPS),
- Controlled Atmosphere Plasma Spraying (CAPS),
- Inert Atmosphere Plasma Spraying (IPS),
- High Pressure Plasma Spraying (HPPS).

Additionally, plasma spraying installations are distinguished between Direct Current (DC) and Radio Frequency (RF) torch type. Diversity of the systems allows to spray materials in form of wires, rods and most commonly powders. Finally, lately emerged family of the processes involve liquid feedstock employment , e.g.,:

- Suspension Plasma Spraying (SPS),
- Solution Precursor Plasma Spraying (SPPS).

Principles

Typical DC plasma torch is presented in Figure 2.1. Electric arc, created between copper anode and tungsten cathode, heats up the working gases, which creates plasma jet expanded through the torch nozzle. Material usually in form of the powder is transported by carrier gas and injected through powder port into the plasma. In the jet, powder particles are melted and accelerated towards the substrate. Coating is formed with the impact of fully or partially molten particles at substrate surface.

Plasma torch is intensively cooled by water, which preserve the electrodes from melting and consumption. Intense cooling of plasma nozzle also stabilizes the plasma jet. As a result, electric current flow, has a tendency to concentrate in the hot centre of plasma stream. This stabilization of plasma leads to further increase of its temperature and, consequently, electrical conductivity [17].

Usually used plasma gases are Ar, He, H_2, N_2. Type of gas (or gas mixture) determines plasma temperature and enthalpy. Enthalpy of plasma stream at the same temperature is higher for molecular gases (H_2, N_2) than for monatomic ones (Ar, He). Energy of molecular gases is stored not only with ionization but also with dissociation (Table 2.1). The plasma of molecular gas is able to supply greater amounts of energy. On the other hand, the monatomic gases reach a higher velocity, which is related with higher temperature of the gas. To ensure high velocity and high enthalpy of the plasma, Ar + H_2, Ar + N_2, N_2 +H_2 mixtures of the gases are used [18].

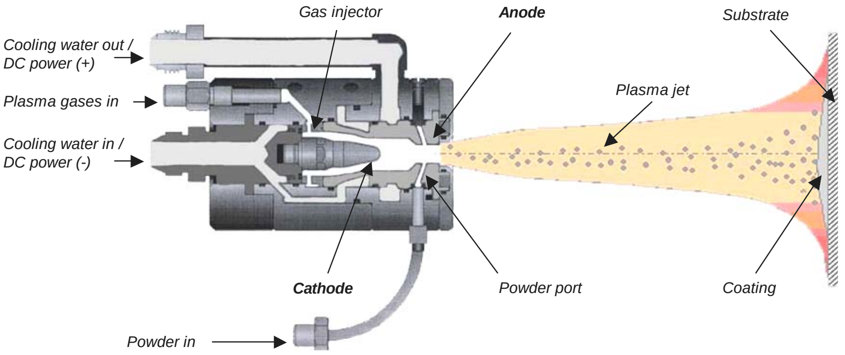

Figure 2.1 Sketch of typical DC plasma torch.

The temperature of plasma can reach up to 20 000 K, and as a effect, plasma stream leaves the nozzle with the velocity of 800 m/s or more. Plasma jet properties like distribution of temperature, velocity can be controlled in very wide range by change of torch construction, kind of the gases or electric parameters of plasma arc. Furthermore, position of powder injection point has a great influence on distribution, size and temperature of sprayed particles, and as a result on sprayed coatings properties [19].

Table 2.1 Main physical parameters of gases used for plasma spraying [17]

Physical parameter	Ar	He	H_2	H	N_2
Density, kg/m^3	1.78	0.178	0.098	-	1.25
Energy of ionization, eV	15.7	24.9	15.4	13.6	14.5
Energy of dissociation, J/mol	-	-	$4.3*10^5$	-	$9.4*10^5$
Heat capacity J/(mol · K)	21	21	35	-	-
Thermal conduction coeff. at 6000 K, W/(m K)	0.17	1.5	2.0	3.8	-

Liquid Feedstock

Introduction of liquid feedstock (suspensions or solutions) to thermal spray technology opened another path to deposit fine structured coatings. On the other hand, handling with liquids needs new transportation and injection techniques.

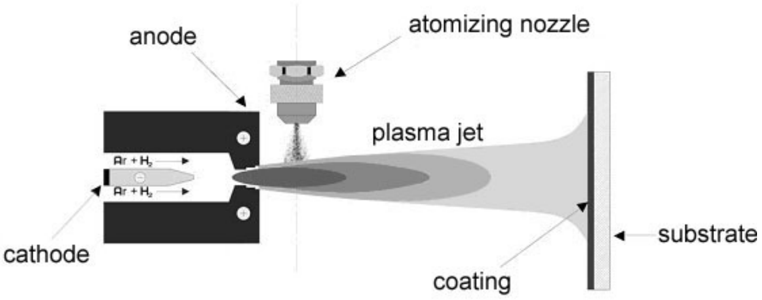

Figure 2.2 Sketch of suspension injection with use of atomizing nozzle.

Two methods of injection are commonly used:

- **pneumatic injection** in which the liquid is atomized into a spray by a pressure atomizer that generates narrow angled mist cone of droplets in the range of 2–100 µm with velocities from 5 to 30 m/s resulting in a wide range of droplets momenta. These droplets are injected transversely into the plasma jet where they are entrained and heated (Figure 2.2). Some of the low momentum droplets (small size, low velocity) could not penetrate into the high velocity plasma jet and they are carried towards the substrate around the periphery of the plasma jet [20][21].
- **mechanical injection** using:
  - an ink printer heads where the droplet size is determined by nozzle diameter and the velocity - by the pressure. Described system was used by Blazdell and Kuroda [22], where the ceramic ink is forced under pressure (up to 0.5MPa) through a 50 µm diameter nozzle (Figure 2.3). A pressure wave is superimposed by piezoelectric drive rod at frequency of 64 kHz. These pulses regulate the stream break-up into mono-sized 100 µm droplets. Oberste-Berghouse *et al.* used similar device based on magnetostriction drive operated at frequency of 30 kHz [23];
  - a pressurized tank in which a suspension is stored and an injector consisting of a stainless steel tube with a laser machined nozzle. A suspension is injected by controlling the pressure of the tank with compressed air, the pressure of injection is being monitored with a gauge. A natural stream fragmentation occur at about 15mm

downstream of the injector exit with creation of droplets of 300 µm diameter [24][25][13].

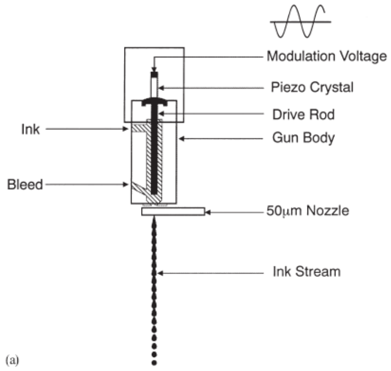

Figure 2.3 Ink printer injection based device [22].

Droplet interaction with plasma jet

Upon injection into the plasma jet, two phenomena occur: droplet fragmentation and evaporation. Calculations of droplet fragmentation by Fazilleau *et al.* and Fauchais *et al.* using simple force balance (i.e. assuming that the drag force equals the surface tension force) have shown that the fragmentation time of large droplets (50 to 300 µm in diameter) was much shorter (a few microseconds) than their vaporization time (2 to 3 orders of magnitude) [26][27]. Therefore, fragmentation can be calculated neglecting vaporization. For example, considering Ar-H_2 plasma jet, initial droplets of 225 µm in diameter are fragmented into droplets as small as 1 µm before they reach plasma jet axis, fragmentation starts in the plasma periphery.

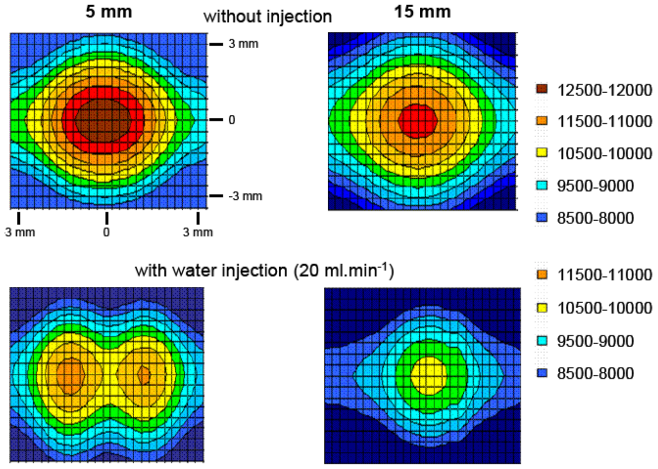

Figure 2.4 Influence of water injection on the plasma temperature in 5 and 15 mm distance downstream [26].

Fazilleau *et al.* investigated influence of injected water into the plasma by spectroscopic measurements of the jet temperature. With injection of 20 ml/min, the plasma jet was observed to be separated at 5 mm downstream of the nozzle exit (Figure 2.4). However, at 15 mm downstream of the nozzle exit, the jet is again symmetrical. It should also be noticed that the temperature dropped by only 2000 K with water injection. More radical cooling down of the plasma jet was observed with liquid flow rates above 50 ml/min. Moreover, application of ethanol instead of water for injection consumed less energy.

Suspension plasma spray

Many papers have been devoted to this topic in the last ten years. Initially research was focused on suspension injection into RF plasma. Successively, last five years brought many publications on DC plasma SPS. Usually formulated suspension consists of:

- nano/submicrometer powder; size distribution and morphology of the powders have great influence on coating microstructure. The selection of the powder has to be generally made between nanoparticles with a size distribution up to tens of nanometers, usually obtained by chemical routes, or submicrometer produced by attrition milling, with a size distribution in range of hundreds of nanometers. Fauchais *et al.* have observed difference of droplet history depending on the morphology of the powder. Figure 2.5 demonstrates the history of already fragmented droplet. One can observe, that the nanometer sized particles produced by chemical route seem to agglomerate easily within droplet [5]. After evaporation of the solvent, agglomerates explodes into molten or vaporized particles (Figure 2.5a). However, droplets containing attrition milled particles endure more predictable mechanism (Figure 2.5b);

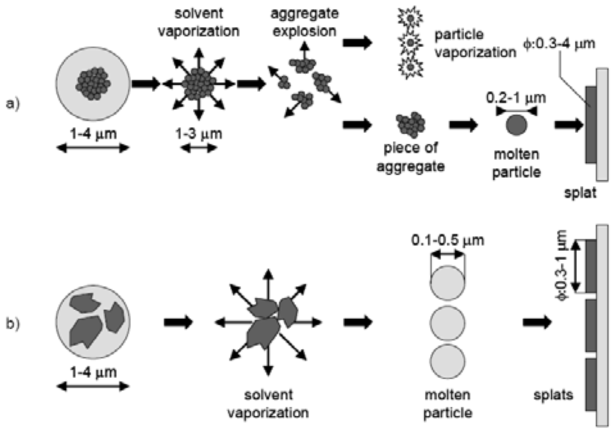

Figure 2.5 History of the suspension droplet in the plasma jet [5]

- solvent; water used most commonly or as an alternative organic solvent (e.g. ethanol or isopropanol). Application of organic solvent is expected to reduce cooling and separation of the plasma jet during injection, as evaporation enthalpy is lower than that of water (Table 2.2). Moreover, reaction enthalpy of solvent combustion will contribute to enhance temperature and velocity of the plasma jet;

- Dispersant; surface active agent which keeps suspension well dispersed, absorbed on the particle surface prevents the agglomeration of the particles by electrostatic and steric repulsion.

Table 2.2 Physical parameters of the solvents

Solvent	Evaporation temperature [°C]	Evaporation enthalpy [kJ/g]	Reaction enthalpy [kJ/g]
Water	100	2.26	-
Ethanol	78.3	0.84	29.7
Isopropanol	82	0.64	33.39

Solution precursor plasma spray

Many papers were published on this topic since 1997, mainly concerning deposition of YSZ for thermal barrier application [28][29][30][31][32][33] and also YIG coatings [34][35]. The solution precursor plasma spray (SPPS) process is similar to suspension plasma spray (SPS) except that the chemical precursor is used in place of solid particle suspension. In the case of yttria-stabilized zirconia formation, the solution is composed of zirconium acetate and yttrium nitrate as solute and water as solvent. The solutions can be injected to plasma with use of atomization nozzle positioned axially or radially to the plasma jet.

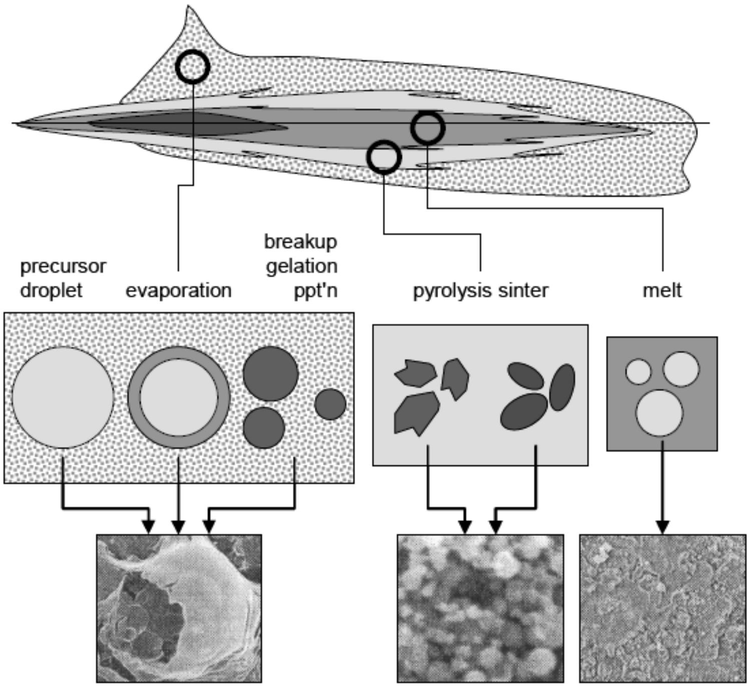

Figure 2.6 Mechanism of solution droplet-plasma interaction [30]

The atomized precursor droplets undergo rapid evaporation and break-up in the plasma (Figure 2.6). This is followed by precipitation or in some cases (lower temperatures) gelation of the precursor occurs. If the droplet approaches plasma periphery further pyrolysis and sintering take place. Finally, melting of the sintered particles occurs if the droplet enters the hot centre of the plasma [30]. The model of heat and momentum transfer from plasma to droplets presented by Oztur and Cetegen [20][21], considers both atomiser orientations (axial, transverse). The authors observed precipitation at much earlier stages of the droplet lifetime for axial injection, when compared to the transverse injection. It was also hypothesized that heat up of the droplets can lead to shattering of a formed crust and break-up of the internal liquid into smaller droplets. Small droplets (d < 5 µm) are expected to form fully precipitated solid spheres.

2.2. MICROSTRUCTURE OF THE COATINGS

2.2.1. Phase composition

The phase diagrams, that are so useful in many technologies of materials engineering, prove to be less useful in plasma spraying. Their application permits predicting the phase composition of the coating (knowing the phase composition of the powder) only by taking a lot of precautions. The reason for this are threefold: first, plasma spraying is accompanied by rapid solidification phenomena often resulting in new phases or even in an amorphous structure, secondly, it might be accompanied by a change in chemical composition (by e.g. selective evaporation of a component of multi-component powder), and thirdly the spraying atmosphere may lead to the coating oxidation or reduction.

The phase composition of sprayed coating depends on the following technological factors:

- chemical and phase composition of the starting powder as well as the morphology of its particles (produced by agglomeration, fusing and crushing or gas atomization);
- spraying technique, particularly the spraying atmosphere and all the processing parameters influencing the process of rapid solidification and rapid cooling. These two processes are an integral part of the thermal history of sprayed particles and the lamellae in the coating. The particle is melted and brought up to evaporation in a time of milliseconds before the impact upon the substrate (or previously deposited coating) and deforming in lamellae that cools down to the melting point and solidifies. The final stage of thermal history finishes when lamella inside the sprayed coating cools to room temperature (Figure 2.7);
- Post-spraying treatment accompanied by coating recrystallization.

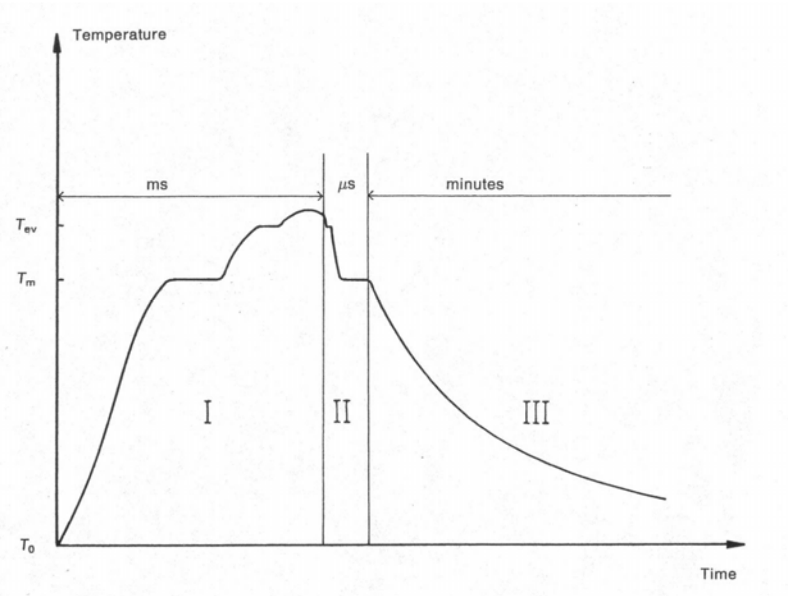

Figure 2.7 The thermal history of a particle in the flame (region I) deformed after impact into a lamella that cools down to the melting point and solidifies (region II) and this lamella within the deposited coating that cools down to the room temperature (region III) [1]

Composition and morphology of powder

Morphology and internal structure of powder is determined by its production method, for example spray-dried powders, characterized by significant internal porosity, require higher temperature of plasma flame and/or decrease the flow rate of the working gases, comparing to other powders [36]. Moreover, spray-dried powders promote formation of compounds, for example formation of spinel Al_2TiO_5 from Al_2O_3+40 wt.% TiO_2 powder, due to close contact of precursor particles (Normand *et al.* [37]), and consequently higher possibility of reaction between them.

Composition modification of sprayed material

The particles are melted in the plasma during spraying and their temperature may be higher than their boiling point. In materials composed of many phases, the phase having the lowest melting and evaporation points would evaporate faster than others. This results in the modification of chemical composition in sprayed coating. For example, a hydroxyapatite powder particle injected into the plasma suffers thermal decomposition during its flight. Decomposition sequence occurs in four steps [38][39]:

Step 1: $Ca_{10}(PO_4)_6(OH)_2 \rightarrow Ca_{10}(PO_4)_6(OH)_{2-2x}O_x\square_x + xH_2O$

(hydroxyapatite) (oxyhydroxyapatite)

Step 2: $Ca_{10}(PO_4)_6(OH)_{2-2x}O_x\square_x \rightarrow Ca_{10}(PO_4)_6O_x\square_x + (1-x)H_2O$
(oxyhydroxyapatite) (oxyapatite)

Step 3: $Ca_{10}(PO_4)_6O_x\square_x \rightarrow 2Ca_3(PO_4)_2 + Ca_4O(PO_4)_2$
(oxyapatite) (TCP) + (TTCP)

Step 4a: $Ca_3(PO_4)_2 \rightarrow 3\,CaO + P_2O_5$
Step 4b: $Ca_4O(PO_4)_2 \rightarrow 4CaO + P_2O_5$

Based on this decomposition sequence a model was developed [38] showing the in-flight evolution of individual calcium phosphate phases as shown in Figure 2.8.

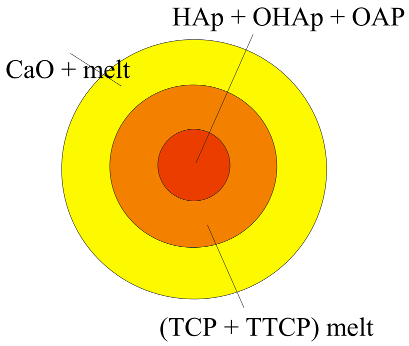

Figure 2.8 Model of phase composition of individual HAp particle decomposed in plasma jet .

Figure 2.8 shows that during the short residence time of the HAp particle in the plasma jet the innermost core is still at a temperature below 1828 K (incongruent melting point), consisting of HAp, OHAp and OAp as stable phases (steps 1 and 2). The second shell was heated to temperatures above 1843 K and consists of a melt with a Ca/P ratio of 1.67 (step 3). The outermost shell is composed of CaO and a melt whose Ca/P ratio shifts by continuous evaporation of P_2O_5 along the liquidus of the binary phase diagram CaO-P_2O_5 towards CaO-richer phases, *i.e.* TTCP (step 4). On impact at the target surface this molten phase solidifies to produce ACP with various Ca/P ratios.

Rapid solidification and rapid cooling

The rapid solidification and rapid cooling are the phenomena that occur after the impact of the particle with the substrate (or previously deposited coating). These phenomena may result in a formation of metastable phase. The best known example is the formation of the γ-Al_2O_3 phase (being metastable at room temperature) while spraying α-Al_2O_3. It's explained by lower energy for nucleation from liquid for γ than for α-phase [40].

When the HAp particle impinges at the metal surface the clear and entirely neat phase separation shown in Figure 2.8 will be lost. The result is an extremely inhomogeneous calcium phosphate layer in which HAp, OHAp, TCP (α-TCP; β-TCP, whitlockite), TTCP (hilgardite), CaO (oldhamite), and ACP of various composition are interspersed on a nano- to microcrystalline scale [41]. Figure 2.9 shows hypothetically the sequence of events, starting with stage 1 (free flight and evaporation phase, Figure 2.9a) and progressing through stage 2 (contact and compression phase, Figure 2.9b), stage 3 (compression and flow phase, Figure 2.9c), stage 4 (remelting phase, Figure 2.9d), stage 5 (deformation and splashing phase, Figure 2.9e) to stage 6 (relaxation and cooling phase, Figure 2.9f).

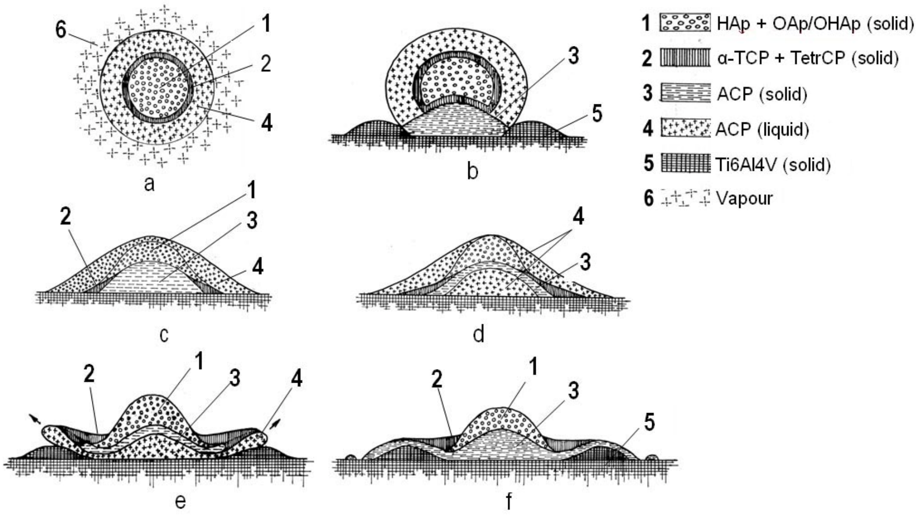

Figure 2.9 Sequence of events a to f occurring during deposition of a supersonically accelerated semi-molten hydroxyapatite particle impinging on a roughened Ti6Al4V substrate (for explanation see text) [41].

Post-spraying treatment

Post spraying treatment at appropriate temperatures might enable the metastable phases to transform back to equilibrium ones. For example, γ-Al_2O_3 in as-sprayed coating recrystallizes to equilibrium α-Al_2O_3 under heat treatment at a temperature about 1270 K. The same recrystallization occurs also at an application of laser treatment [42].

2.2.2. Coating inhomogenity

The deposited coatings by plasma spray process are strongly inhomogeneous due to several factors, such as:

- inhomogenity of sprayed powder; size, morphology, chemical and phase composition of single particles in the same powder lot differs. For example, TiO_2 containing particles being slightly reduced to a lower oxide would result in a coating having inclusion of Ti_xO_{2x-1} Magneli phases [43].
- variation of feedstock feed rate; feeding systems do not always give a constant feed rate.
- variation of plasma velocity and temperature caused by electric arc fluctuation [44].

Due to above mentioned factors the particles arrive at the substrate with different velocity and melt state (molten, partially molten, not melted), which results in several microstructural features. Many authors proposed qualitative classification of the coating defects. Pawlowski have identified 9 class of the defects (Figure 2.10):

- poor contact to the substrate,
- crack resulting from the relaxation of one-torch-pass stress,
- crack resulting from the relaxation of residual stresses in the vertical direction,

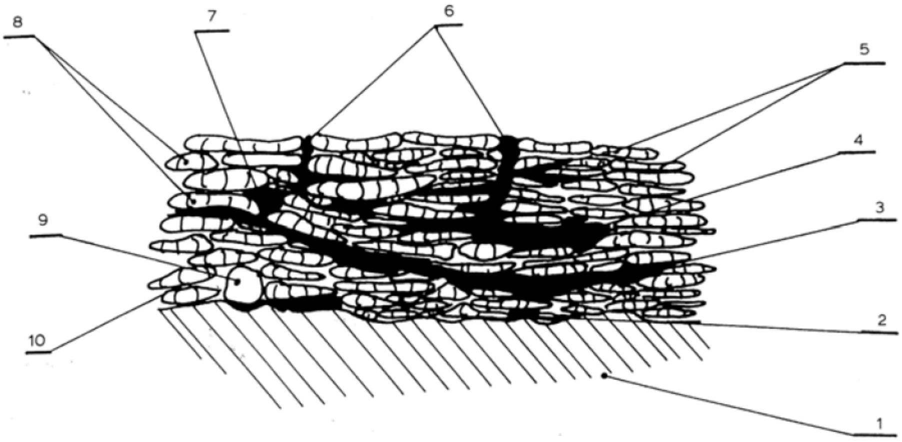

Figure 2.10 Sketch of the cross-section of thermally sprayed coating showing possible defects. 1, substrate; 2, poor contact to the substrate; 3, crack resulting from the relaxation of one-torch-pass stress; 4, crack resulting from the relaxation of residual stresses in the vertical direction; 5, columns of solidification in the lamellae; 6, cracks resulting from the relaxation of residual stress in the planar direction (open porosity); 7, void resulting poor deformation of partially melted particle (few micrometers void); 8, lamellae formed of well melted particles; 9, unmelted particle; 10, void resulting from poor interlamellar contact (submicrometers voids) [1].

- columns of solidification in the lamellae,
- crack resulting from the relaxation of residual stress in the planar direction (open porosity),
- voids resulting poor deformation of partially melted particle (few micrometers voids),
- lamellae formed of well melted particles,
- unmelted particle,
- void resulting from poor interlamellar contact (submicrometers voids).

Some of the defects result from improper spray parameters selection (e.g. high power with close spray distance leads to excessive overheating of the substrate).

Particle deformation

The particles are melted and accelerated by the plasma. During the impact with the substrate particle takes form of lamellae (so called "splat"), this transformation is associated with deformation and solidification.

Many authors investigated morphology transformation of lamellae in function of spray process parameters, velocity and temperature of the particles at the impact, nature and temperature of the substrate. Kudinov *et al.* have presented the classification of 30 different splats morphologies of the alumina particles in dependence of velocity and temperature during the impact (Figure 2.11) [45].

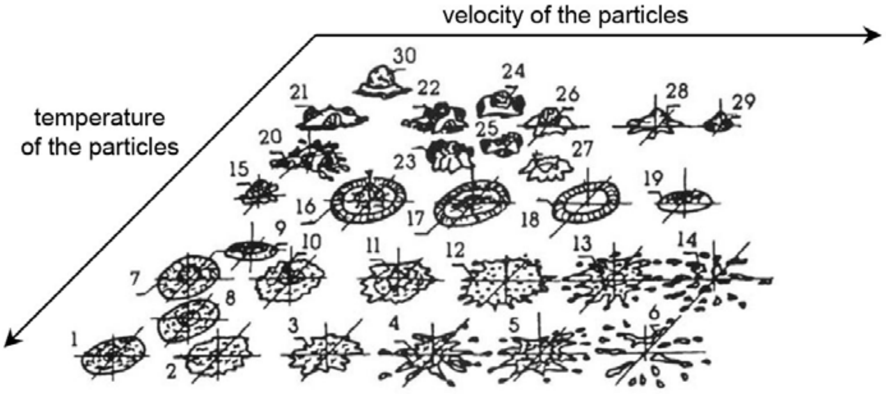

Figure 2.11 Morphology of plasma sprayed alumina particles in function of their velocity and temperature before the impact [45].

The temperature of the substrate during the particle impact plays important role also. The adhesion of the splats is improved if the substrate was preheated prior to deposition. The preheating causes slight superficial oxidation (for metallic substrates) and desorption of water molecules, which increases wettability of the substrate with liquid ceramics. The threshold temperature of the substrate above which the splats form regular round forms is defined as critical temperature of the substrate. Fukumoto *et al.* explained flattering of the particles at the substrate with temperature above and below critical temperature. The impact of the particle at cold substrate formed a exploded “flower like” splat resulting in formation of pores (Figure 2.12). This phenomenon is explained by low wettability of the substrate. In case of preheated substrate (above critical temperature), droplets form regular round splats [46][47].

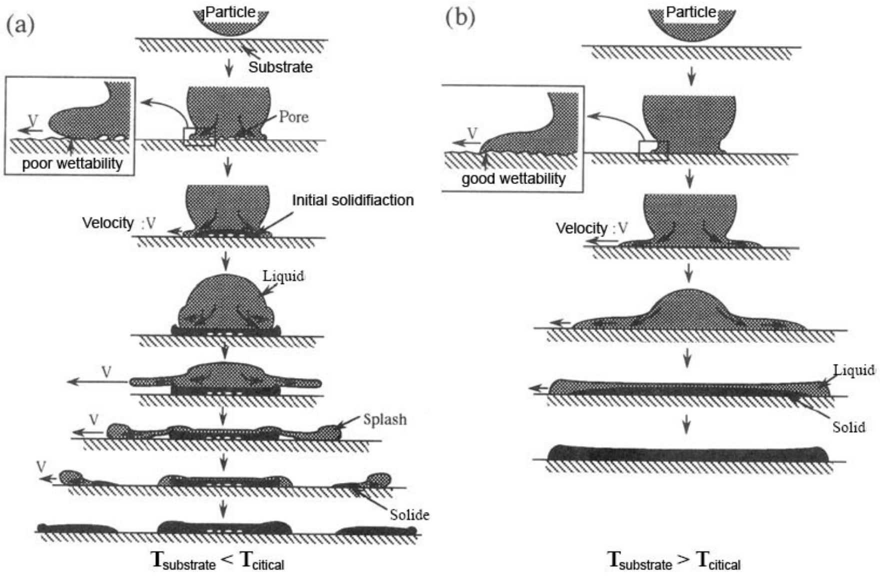

Figure 2.12 Schematic representation of flattering mechanism of the droplets in function of substrate temperature; a – $T_{substrate} < T_{critical}$, b - $T_{substrate} > T_{critical}$ [46]

CHAPTER 3

FIELD ELECTRON EMITTERS

Electron emitting cathodes implemented in electronic vacuum devices were the only active elements of electronics in the first half of XXth century. The main sources of electrons applied in electronic tube were thermionic cathodes, also in some rare specific applications – photocathodes. In the 1940s, Dyke has initiated investigations of field emission (FE) effect from tungsten electrolytic etched ultrasharp tips, because he believed that FE cathodes had unique properties which may increase the performance of variety of microwave devices [48]. His work established a useful foundation on which other groups have built their success. Among these was Spindt, who introduced in 1968 the ideas of Dyke into vacuum microelectronics by production of field emitters using the thin film technology [49]. Introduction of this technology allowed integration of cathode and extractor (Figure 3.1), and finally arrange the emitters into very large scale integrated arrays. This solution made it possible to obtain 1000 A/cm^2 field emission current density. Moreover, short distance between cathode and extractor reduced extraction voltage down to tens of volts (Figure 3.2).

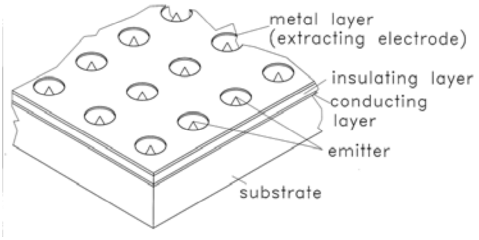

Figure 3.1 Spindt type emitters array [50].

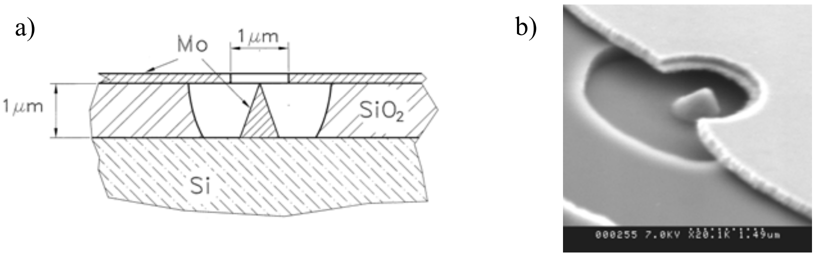

Figure 3.2 Single Spindt type field emitter; a – sketch of cross-section [50], b – SEM micrograph [51]

Over the last decades, the scientific community focussed on searching the new emitting materials, especially diamond, diamond like carbon (DLC), nanotubes or other materials with wide bandgap, i.e. BN and AlN.

Another branch of research goes into development of the composite emitters with use of alternative production techniques, such as plasma spraying. Znamirowski *et al.* investigated plasma sprayed and laser engraved Cr_2O_3 coatings covered with PVD thin film of Ti. As it was proved the emission occurred from Ti coated single micrometers sized Cr_2O_3 crystallites (Figure 3.3) generated at the solidification of laser molten Cr_2O_3 [52][53].

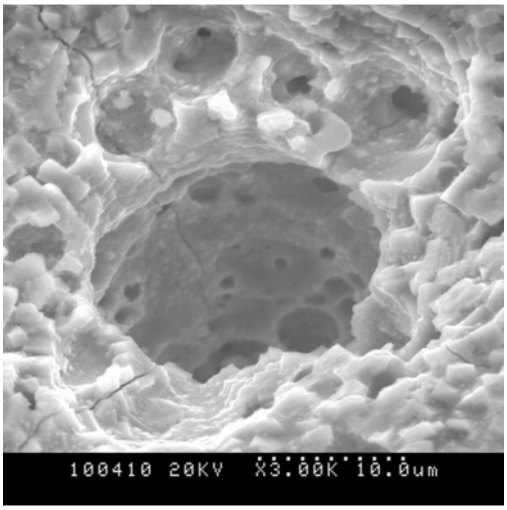

Figure 3.3 Laser engraved cell of plasma sprayed Cr_2O_3 coating [53].

Further study were focused on field emission obtained from plasma sprayed TiO_2 and Al_2O_3/TiO_2 ceramics **[54]**[55][56]. As the coatings are characterized by inhomogeneous structure, containing several crystal phases (electrically insulating and conducting), the authors believed that field emission can be enhanced. This phenomenon was explained by means of composite emitter model elaborated by Forbes for carbon films[57].

3.1. PHYSICAL BACKGROUND OF FIELD EMISSION

Electron emission from solid body to vacuum can occur if supply sufficient energy. Energy can by supported by heat (thermionic emission) or photon (photoemission). When the electric field is applied to the surface of the thermionic emitter, reducing the magniture of surface potential barrier, increasing the number of electrons able to escape from the surface, the phenomenon is called Schottky emission.

Electrons can also escape from the solid surface by tunnelling through potential barrier, only if the barrier is finite-dimensional, which occurs by applying external electric field. The probability of electron tunnelling is inversely proportional to a width of potential barrier [50]. The higher is electron energy (but still under potential barrier height), the narrower is potential barrier, which has to be passed through, and in result probability of electron tunnelling is higher. The field emission under elevated temperature (a electron energy is increased to the level for which the potential barrier is narrow enough to obtain desired emission current) is called thermal field emission (Figure 3.4).

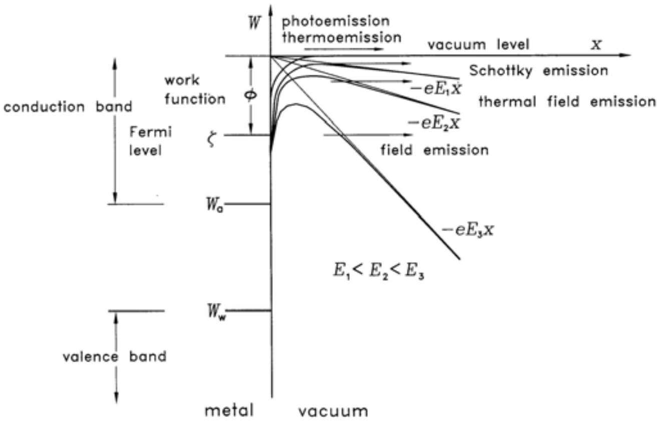

Figure 3.4 Mechanisms of electron emission from metals; W_a – lowest energy of conduction band, W_w – highest energy of valence band, ζ – Fermi level [50]

Fowler and Nordheim (FN) developed the model of cold field electron emission. Elaborated FN equation (3.1)

$$J = A\frac{E^2}{\Phi t^2(y)}\exp\left(-B\frac{\Phi^{\frac{3}{2}}}{E}v(y)\right), \tag{3.1}$$

predicts the electron emission density (J) from a cold metal as a function of applied electric field (E) and work function (Φ), where

$$\begin{aligned} A &= \frac{e^3}{8\pi h}, \\ B &= \frac{8\pi\sqrt{2m}}{3eh}, \end{aligned} \tag{3.2}$$

t(y) and v(y) are Nordheim elliptic functions. It can be assumed that $t^2(y) = 1,1$ and $v(y) = 0,95 - y$ [50], where

$$y = 3{,}7947 \cdot 10^{-5} \frac{E^{1/2}}{\Phi}. \tag{3.3}$$

Current density (J) can be expressed as overall emission current (I) divided by emitting surface area (α)

$$J = \frac{I}{\alpha}. \tag{3.4}$$

Electric field can by assumed as linear function of potential difference, dependent on shape of the electrodes. It can be stated that

$$E = \beta \cdot V, \tag{3.5}$$

where V is applied voltage and β shape coefficient of electrodes.
Substitution of Equation 3.4 and 3.5 to Equation 3.1 results in following expression

$$\ln\left(\frac{I}{V^2}\right) = -\frac{b_{FN}}{V} + \ln a_{FN}. \tag{3.6}$$

where

$$a_{FN} = \frac{\alpha A \beta^2}{1{,}1\Phi} \exp\left(\frac{1{,}45 \cdot 10^{-7} B}{\Phi^{1/2}}\right) \tag{3.7}$$

and

$$b_{FN} = \frac{0{,}95 B \Phi^{3/2}}{\beta}. \tag{3.8}$$

Obtained expression (3.6) allows to draw a graph log $I/V^2 = f(1/V)$, known as Fowler-Nordheim (F-N) plot. Knowing the β, one can easily derive many parameters (i.e. work function, emission spot surface area, etc.) from the F-N plot. Those parameters are very useful in comparison of different emitters.

Composite field emitter (Forbes Model)

Field-induced electron emission from different materials obtained with different methods sometimes appears at surprisingly low field values.

It's important to distinct between macroscopic field E_0 measured in a flat-capacitor situation and a local field E which is the actual field at an emitting spot. The local field E determines the slope of the tunnelled potential barrier for electron. The two fields are related by equation (3.5). Visible cold field emission usually occurs at local field values of about 2 V/nm or above. If, experimentally, cold field emission occurs significantly below these 'usual' local field value, then this is called 'low macroscopic field' LMF emission [58].

When a conducting surface has small sized sharp protrusion on it, this can considerably improve field enhancement factor. The phenomenon is termed 'external field enhancement' and is the physical explanation for low macroscopic field (LMF) emission. The additional explanation of low macroscopic field emission in thin films was presented by Forbes. The main arguments of his hypothesis were:

- in many (probably most) experimental situations, LMF emission from a thin dielectric film occurs because the film is an electrically nanostructured heterogeneous (ENH) material,
- electrical nanostructure, either completely or very largely inside the film, can create field enhancement at the vacuum interface, causing the local field there to be much greater than the measured macroscopic field. The local field can be high enough to allow rapid electron tunnelling into vacuum. This is the internal field enhancement (internal-β) hypothesis. In some cases, hybrid field enhancement (due to electrical nanostructure partly inside, partly on top of the film) may operate.
- An ENH thin film also provides conduction paths able to carry adequate current from the substrate to the emitting features. Details of charge transport mechanisms may vary as between films as for a given film when the circumstances of emission vary.

An ENH material has some or all of the following structural components:

- a dielectric matrix;
- small (often nanoscale) conducting or semiconducting inclusions within the dielectric;
- conducting channels between inclusions, and between inclusions and the substrate
- an emitting channel that terminates at the vacuum interface [58].

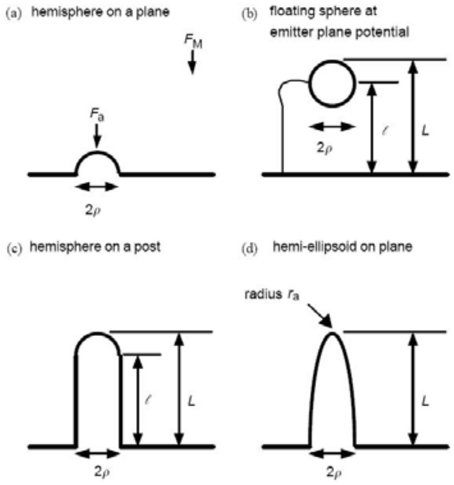

Figure 3.5 Geometrical/mathematical models for a field enhancing micro/nanoprotrusion: (a) hemisphere on a plane, (b) floating sphere at emitter plane potential, (c) hemisphere on a post, (d) hemi-ellipsoid on plane; L – distance of the apex of the sphere or protrusion from the emitter plane; l – the height of the centre of the sphere above the emitter plane [59]

There can exist various physical causes of field enhancement, but the most obvious seems to be a micro/nanoprotrusion at the emitter surface. The estimation of the field enhancement factor β was done in recent literature [59].

The three simplest models of "hemisphere on a plane", "floating sphere at emitter plane potential model" and the "hemisphere on a post" are presented in Figure 3.5a-c

The first model was analysed exactly to yield enhancement factor β = 3. The remained two are related with geometrical features of the protrusions determined by relation:

$$\beta = m + \frac{h}{\rho} \tag{3.9}$$

, where $\boldsymbol{\rho}$ is a sphere or hemisphere radius, $\boldsymbol{h}$ is a height of sphere of hemisphere above emitter plane, and $\boldsymbol{m}$ is a constant (depending how $\boldsymbol{h}$ is defined).

The "floating sphere at emitter plane potential model" which is not an obvious geometrical could be treated semi-analytically to yield similar formula to more realistic model of "hemisphere on a post". The model assumes that: (1) distant from the floating sphere there is an uniform field above the emitter plane; (2) the emitter plane is at uniform potential; (3) the sphere is at uniform potential, equal to that of the emitter plane. In practice in literature it is common to observe for "floating sphere at emitter plane potential model" the equation (3.10)

$$\beta = 2.5 + \frac{L}{\rho} \tag{3.10}$$

, where $\mathbf{L} = \mathbf{l} + \boldsymbol{\rho}$.

According to Rohrbach [60], the model of "hemisphere on a post" yield:

$$\beta = 3 + \frac{l}{\rho} \tag{3.11}$$

The model of 'hemi-ellipsoid on plane' feature all above mentioned, considered as an ellipse of semi-major axis length **L** and semi-minor axis length $\boldsymbol{\rho}$. The axis ratio v of the ellipse, a parameter ξ, and the apex radius of curvature $\mathbf{r_a}$ are given by

$$v = \frac{L}{\rho}, \tag{3.12}$$

$$\xi = \left(v^2 - 1\right)^{1/2}, \tag{3.13}$$

$$r_a = \frac{\rho^2}{L} = \frac{\rho}{v}. \tag{3.14}$$

In case when hemi-ellipsoid is located on a large flat plane (Figure 3.5d), the field enhancement factor $\boldsymbol{\beta}$ is given by

$$\beta = \frac{\xi^3}{[v \ln(v + \xi)] - \xi} \tag{3.15}$$

The general conclusion on presented models is that the value of the field enhancement factor β for a micro/nanoprotrusion depend significantly on the shape of the protrusion and its size.

Wide bandgap emitter materials

The wide bandgap materials, such as diamond, indicate interesting electron emission properties. Initially the emission mechanism was ascribed to negative electron affinity, so that the bottom of the conduction band in the bulk of the device lies at an energy higher than vacuum energy. Thus, any electron present in the conduction band within minority carrier diffusion length has a reasonable chance of escaping into the vacuum with no further application of energy.

In case of diamond like carbon layers, the real emission mechanism wasn't unequivocally clarified. Several mechanism are taken into consideration:

1. Negative electron affinity reduces work function.
2. Emission occurs from nano-sized tips.
3. Emission of hot electrons occurs under applied electric field (model bases on insulator nature of diamond; electrons tunnel to conduction band and successively escape to vacuum).
4. Electron emission is induced by electric breakdown between substrate and conducting inclusions on the surface.

Different structures and properties of the DLC coatings gives possibility to simultaneous presence of different mechanisms [50].

CHAPTER 4

EXPERIMENTAL METHODES

4.1. FEEDSTOCK DETAILS

4.1.1. Initial powders

Hydroxyapatite

Commercial Hydroxyapatite powder of Tomita was used during the study. The powder was manufactured by spray drying process followed by calcinations at 800°C for 4 hours. Initially power grains are spherical and of a size distribution suitable for conventional APS purpose.

Titania

Tioxide R-TC90 (Huntsman, England) powder is available as a pigment for paint production. According to technical bulletin, powder contains rutile phase, however is also covered by thin alumina envelope coating. Grain size is of 0.24 µm [61].

Commercially available for thermal spray purposes METCO 102 powder, angular and blocky, produced by fusing and crushing. Characterized by - 88 + 7.8 µm particle size distribution, according to powder technical bulletin [62].

4.1.2. Ball milling

In order to decrease grain size of coarse powders, i.e TiO_2 Metco 102, hydroxyapatite, mechanical ball milling was used. The process was carried out on moliNEx system (NETZSCH, Germany) (Figure 4.1). 1,85mm zirconia balls were used as grinding medium, ethanol acted as cooler. Milling went on for 8 hours with rotation speed of rotor set to 1000 RPM.

Figure 4.1 Ball-milling system

4.1.3. Suspensions formulation

Stability measurements

Important property of suspension (besides of size distribution of the solid particles) is its stability, understood as a ability of sustaining the solid particles dispersed in the solvent. Technically, to ensure well dispersed system dispersing agents should be used.

Determination of a sufficient concentration of the surfactant for TiO_2 suspension was based on stability measurements conducted with use of TurbiScan equipment.
The TurbiScan scans the test-tube containing prepared suspension with laser beam within few minute cycles, backscattered light from the sample is detected and the acquired date is used for particles/agglomerates size estimation. Figure 4.2 shows the example of plots family of backscattered light intensity in function of the test-tube height, the time of measurement is the parameter. At the test-tube height of 40 to 45 mm, the significant backscattered light intensity drop in first 30 min of experiment is observed, which is interpret as a clarification front of suspension.

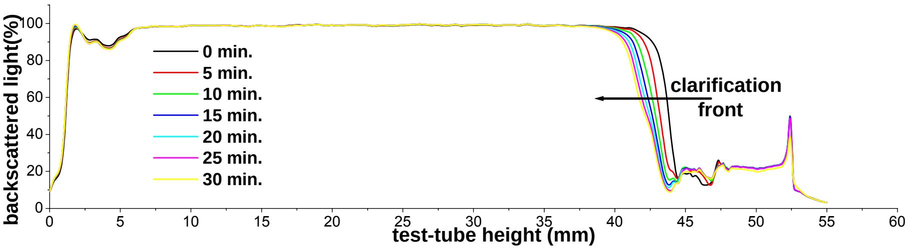

Figure 4.2 Intensity of backscattered signal in function of test-tube height

The stability measurements were done for two dispersants:

- Hydropalat N,
- Hydropalat 5050,

under different concentrations :

- 0,3 wt.% (calculated on a dry powder weight),
- 13 wt.% (calculated on a dry powder weight).

Figure 4.3 shows mean particle size in function of the time for different dispersant with different concentration. The most stable system appears to be the suspension containing 0,3 wt.% of Hydropalat N. The remaining cases were characterized by quick agglomeration of the particles within first 15 minutes after suspension preparation.

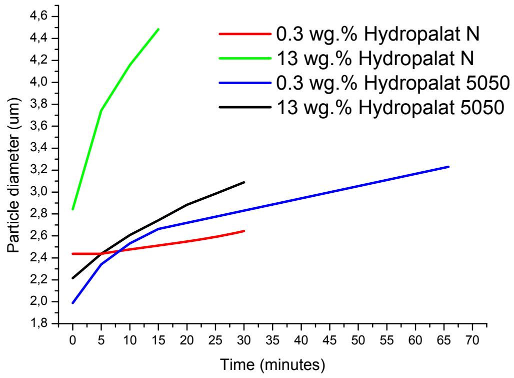

Figure 4.3 Results of suspension stability measurements

Finally three different powders were utilized for suspension preparation, detailed information on suspensions used for spraying of field emitting coatings contains Table 4.1, while Table 4.2 presents information of TiO_2/HAp gradient coating :

- Titanium oxide R-TC 90,
- Titanium oxide METCO 102,
- Ball-milled Hydroxyapatite.

All suspensions contained 0,3 wt.% (calculated on a dry powder weight) dispersing agents (sodium polyacrylate - Hydropalat N or tetra sodium diphosphate), which were initially dissolved in distillate water with the magnetic stirrer (Heidolph MR 1000, Germany).

Table 4.1 Suspension composition for spraying of field electron emitting coatings

Components	**Quantity**
Suspension A:	
Solid particles: TiO_2 Huntsman	4 wt.%
Dispersant: Hydropalat N	0,3 (dwb^{a}%)
Suspension B	
Solid particles: ballmilled TiO_2 M-102	4 wt.%
Dispersant: Hydropalat N	0,3 (dwb%)

Table 4.2 Suspension composition for for spraying TiO_2/HAp gradient coatings

Components	**Quantity**
TiO_2 suspension:	
Solid particles: TiO_2 Huntsman	10 wt.%
Dispersant: Hydropalat N	0,3 dwb[a]%
HAp suspension:	
Solid particles: ball-milled HAp	10 wt.%
Dispersant: tetra sodium diphosphate	0,3 dwb%

[a] dwb : Weight amount of dispersant on a dry weight basis of powder

4.2. PARAMETERS AND CONDITIONS OF PLASMA SPRAYING

4.2.1. Suspension feeding systems

For this thesis two different feeding systems were designed and manufactured by the author. Both systems base on pneumatic injection of the suspension with use of commercial BETE XAPR 100 internal mixing nozzle. Compressed air was used as an atomizing gas. The difference between the systems is the transportation method of the suspension (by pressurized vessel or peristaltic pump)

Pressurized vessel system (PVS)

The initially developed system consists of vessel in which the feedstock is stored (Figure 4.4). After applying the pressure with compressed air, the suspension is pushed out of the tank and fed into the atomizing nozzle. The atomizing gas pulverizes the suspension into the plasma jet.

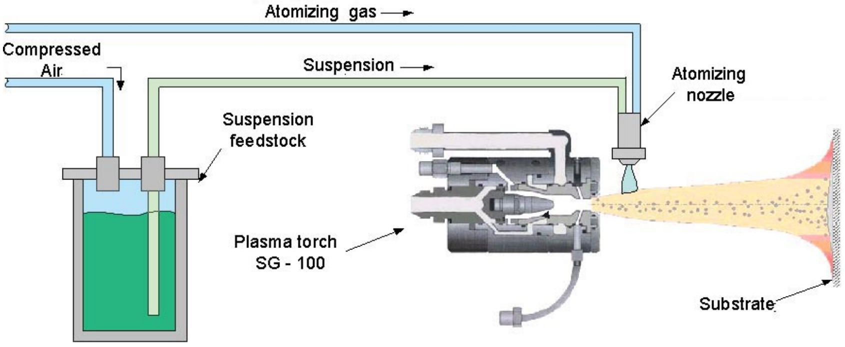

Figure 4.4 Pressurized vessel suspension injection system.

The PVS was used for TiO_2 spray experiments of SPS A and SPS B.
Prior to each operation calibration of suspension feed rate had to be performed. Figure 4.5 presents calibration setup of suspension feed rate. The atomizer is directed to the glass tank, which is placed on the balance. The setup allows the observation of feed rate, stability and symmetry of the atomized liquid cone.

Table 4.3 Calibration data of PVS.

No.	**Atomizing gas pressure [bar]**	**Pressing gas pressure [bar]**	**Feed rate [g/min]**	**Stability**
1	0.3	0.28	13	Not stable
2	0.3	0.3	20	Stable
3	0.35	0.4	34	Stable
4	0.4	0.4	17	Not stable

The calibration data was listed in Table 4.3. It seems that at feed rates 13 and 17 g/min, the atomized cone tend to fluctuate. The effect is undesirable for plasma spraying due to variation of the suspension flow rates causing inhomogenity of the coating. Hence, the flow rates above 20 g/min should be used.

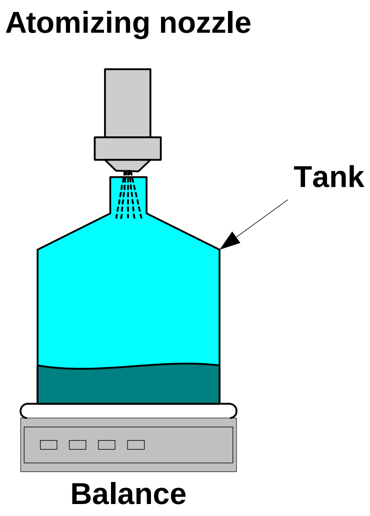

Figure 4.5 Suspension feed rate calibration setup.

Peristaltic pumps system (SPSfeed)

Figure 4.6 shows sketch of improved injection system based on peristaltic pumps heads (OMEGA) mounted on stepper motors (WObit), which were driven by ATmega16 microprocessor (ATMEL). The SPSfeed system offers exceptional simplicity, easiness of use, and variable flow capability. A motor turns the pump's rollers, which squeeze suspension through precision-bore tubing in a wave-like motion. The fluid does not come into contact with the pump; only the outside wall of the tubing does.

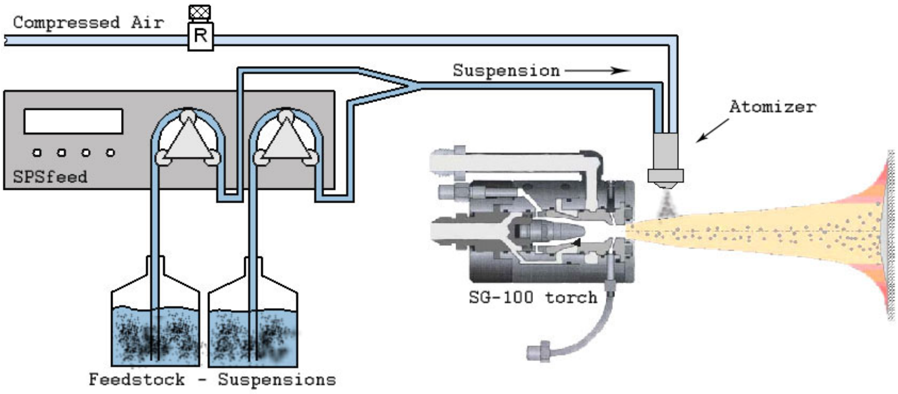

Figure 4.6 SPSfeed – suspension feeding system

The SPSfeed pump offers microprocessor control and a digital display. The user enters values and controls all operations through button keyboard. A dot LCD matrix provides for easy viewing. Calibrating the unit is easy with the user-friendly interface (Figure 4.7). Remote control via ABB Robot interface allows pump start and stop for safe operation during plasma spraying.

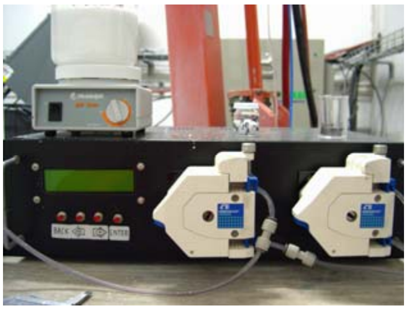

Figure 4.7. Overall view SPSfeed front plate

Features

Flow rates from 1 to 60 ml/minute (per pump head)

Simultaneous feeding from two suspension sources

Reduction of pulsation with application of three-roller geometry head pumps

Large clear LCD display with accurate digital monitoring for clear pump configuration

Microprocessor controlled stepping motor for excellent speed control

User interface

The user interface presented in Figure 4.8 is based on operation on four buttons:

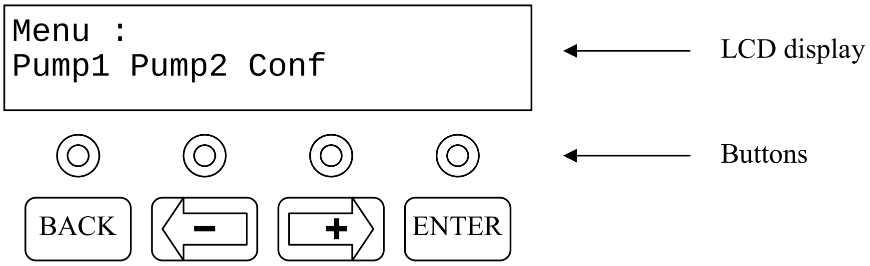

Figure 4.8 Overview of the user interface

BACK – go back from sub-menu (starts pump if pushed in main menu)

Left(minus) – jump left or decrease parameter value

Right(plus) – jump right or increase parameter value

ENTER – confirm change

4.2.2. Plasma spraying parameters

In order to continuous coatings the plasma spraying parameters had to by carefully selected, the main spray parameters were:

- P – electric arc power;
- V – linear velocity of the torch;
- n – number of passes of the torch;
- d – atomizer axis to anode front stand-off distance;
- D – atomizer front to torch axis stand-off distance.

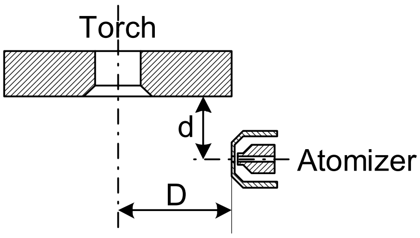

Figure 4.9 Atomizer to torch relative position

The feedback element for parameter selection was the observation of the sprayed sample surface.

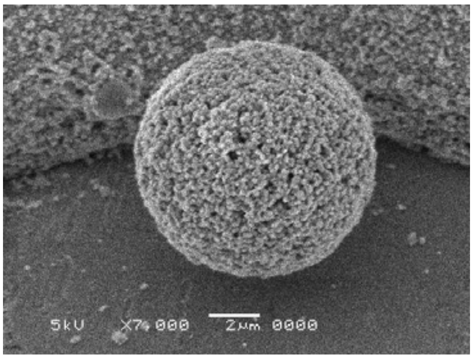

Figure 4.10 Surface topography (P = 30 kW, V = 500mm/s n = 30, D^d = 18^14 mm)

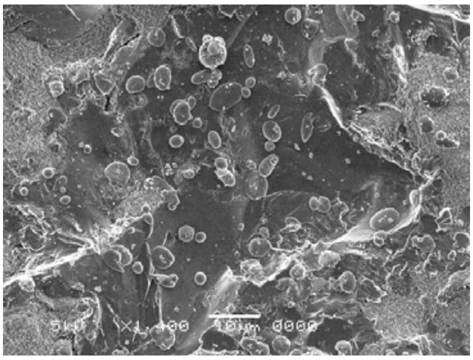

Figure 4.11 Surface topography (P = 35 kW, V = 500mm/s n = 30, D^d = 18^14 mm)

Suspension plasma spraying with P = 30 kW, V = 500 mm/s, n = 30 and D^d = 18^14 mm, resulted in formation of agglomerated sphere of the powder grains presented in Figure 4.10. Absence of the splats, suggests insufficient torch power. After application of P = 35 kW, rarely situated splats were observed (Figure 4.11). Decreasing of torch speed resulted in slight improvement of splats concentration (Figure 4.12)

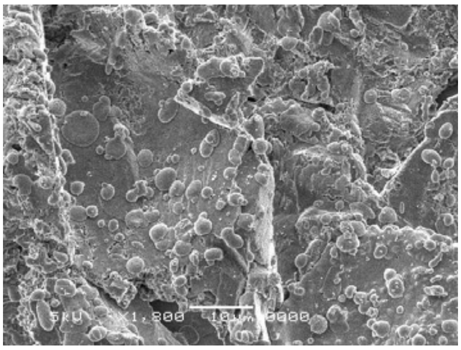

Figure 4.12 Surface topography (P = 35 kW, V = 125mm/s
n = 20, D^d = 18^14 mm)

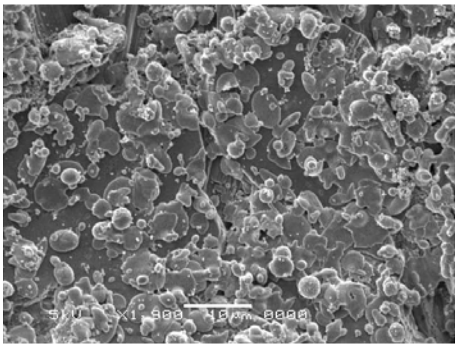

Figure 4.13 Surface topography (P = 40 kW, V = 125mm/s
n = 10, D^d = 18^11 mm)

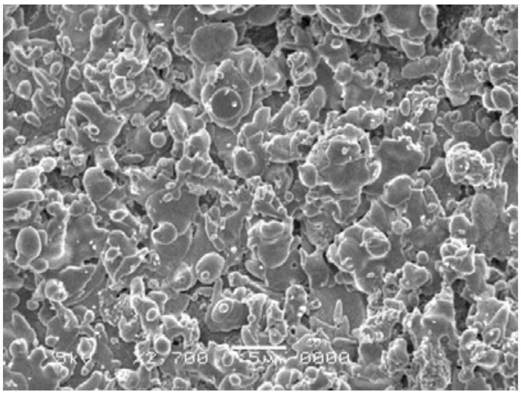

Figure 4.14 Surface topography (P = 40 kW, V = 125mm/s
n = 10, D^d = 15^11 mm)

Further increasing of the torch power to 40 kW and bringing closer together the torch with atomizer, led to significant increase of the splats number (Figure 4.13). Finally, setting up P = 40 kW, V = 125mm/s, n = 10, D^d = 15^11 mm. resulted with total coverage of the substrate with the splats (Figure 4.14).

All the spray experiments were done with use of commercial Praxair installation equipped with SG-100 plasma torch. The Figure 4.15 presents experimental setup with PVS injection system.

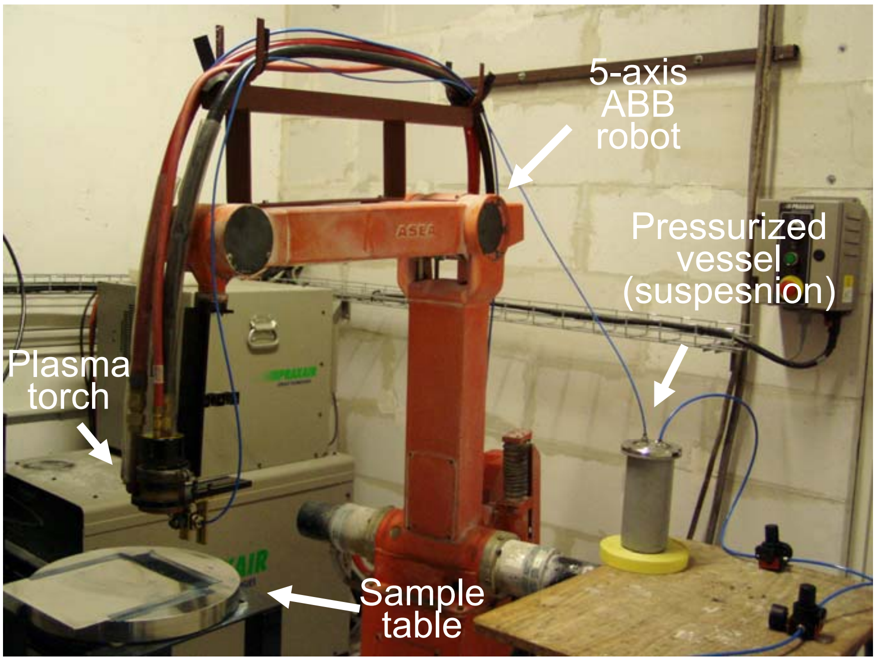

Figure 4.15 Plasma spraying installation

Spraying of field electron emitters TiO_2

Prior to plasma spraying, substrates the 15x15x3mm plates of stainless steel were alumina grit blasted under 5 bar pressure of compressed air, distance between blast gun and substrates was maintained between 80 – 100 mm.

Table 4.4 Plasma spraying parameters fo field electron emitting coatings

	Electric power [kW]	**Plasma gases flow rate [slpm]**	**Spraying distance [cm]**
APS Metco 102	24	Ar = 47, H_2 = 2,5	10
SPS Susp A	40	Ar-50,5; H_2 = 5	10
SPS Susp B	40	Ar-50,5; H_2 = 5	8

Few substrates were coated with the powder Metco 102 (APS) and the rest with suspension A (SPS A) and suspension B (SPS B). Some of Metco 102 coated samples were then sprayed with suspension A in order to receive 2-layered coating (GRAD). The main spray parameters are in the Table 4.4

Spraying of HAp biocompatible coatings

Prior to plasma spraying, substrates the 15x15x3mm plates of titanium were alumina grit blasted under 5 bar pressure of compressed air. Distance between blast gun and substrates was maintained between 80 – 100 mm. Clean and rough substrates were submitted to plasma spraying under different conditions presented in Table 4.5.

- Samples A1 and A2 were obtained by plasma spraying of hydroxyapatite suspension onto prepared Ti substrate.
- In case of samples B1 and B2, prior to HAp suspension spray, substrates were covered with coatings of conventionally sprayed coarse HAp powder.
- Samples C1 and C2 were produced by initially sprayed TiO_2 suspension followed by spraying of HAp suspension.
- Samples D1 and D2 were sprayed with simultaneous feeding of two suspensions (HAp and TiO_2). Feed rate of the suspensions were regulated in such a way to obtain quasi-gradient profile of HAp:TiO_2 ratio and to maintain constant overall flow rate at 25 g/min. Spraying started with pure TiO_2 suspension and after every 10 passages of the torch, content of HAp suspension was increased by 20 vol.%, reaching 100 vol.% at 50th passage. Profile is presented in Figure 4.16.

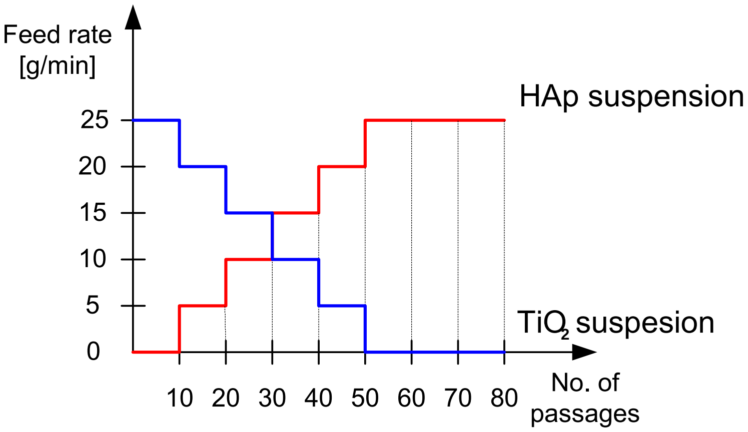

Figure 4.16 Profile of HAp (red line) and TiO_2 (blue line) suspensions feed rates during SPS process

Table 4.5 Spraying parameters

Sample No.	Substrate modifications	Electric arc power [kW]
A1	Ti – without modification	35
A2	Ti – without modification	40
B1	HAp(APS) on Ti	35
B2	HAp(APS) on Ti	40
C1	TiO_2(SPS) on Ti	35
C2	TiO_2(SPS) on Ti	40
D1	Ti – without modification	35
D2	Ti – without modification	40

Kinetics of the robot

Substrates were plasma sprayed using Praxair SG-100 torch mounted on 5-axis ABB IRB-6 industrial robot. Linear velocity of the robot can be changed from 0 mm/s to 1000mm/s.

The spraying experiments were done with velocity of 500 mm/s and torch stand-off distance to substrate at 100 mm. Programmed torch path is presented on Figure 4.17.

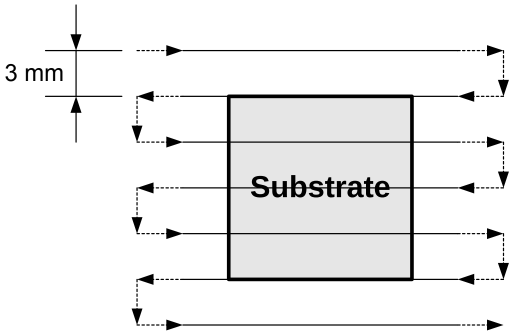

Figure 4.17 Sketch of robot movement

4.3. METHODES OF CHARACTERIZATION

4.3.1. Granulometry

Granulometry measurements of powders were conducted with use of Malvern Mastersizer X.

4.3.2. Scanning electron microscopy

Morphologies of powders and coatings were investigated using JSM 6060 and Hitachi S-570 microscope equipped with a detector of secondary electrons. Cameca CAMEBAX Electron Probe Micro-Analyser (EMPA) was used for qualitative chemical analysis of HAp-TiO_2 cross-sectioned gradient coatings.

4.3.3. X-ray diffraction

Phase analysis was conducted on Bruker type D8, Karlsruhe, with CuK_α radiation in range of 2θ angle from 20° to 80°. The patterns were identified with use of Diffrac^{plus} EVA software base on International Centre of Diffraction Data JCPDS-ICDD.

4.3.4. Micro-Raman spectroscopy

Micro-Raman spectroscopy was carried out using Dilor-Jobin Yvon-Spex, type LabRam spectrometer. HeNe laser (632.8nm, 8mW) was used as an excitation source. The spectral slit width was 150 µm, confocal hole was 500 µm. The diameter of analysis spot was approximately 1 µm. The samples were mounted in a micrometric manipulator of the Olympus BX40 confocal microscope. The spectra were acquired and processed using LABSPEC software.

4.3.5. X-ray photoelectron spectroscopy

VG ESCALAB 220 XL equipped with Mg K_α source (1253.6 eV), without monochromator, operated at 300 W. Constant energy pass was 40 eV. Spectra calibration was performed according to C 1s level at 285 eV.. A homogenous layer model was established for quantitative analysis.

4.4. FIELD EMISSION MEASUREMENTS

Field electron emission measurements were conducted on system presented in Figure 4.18. During the measurements the vacuum was maintained at about 10^{-7} hPa. The distance between cooper anode and emitting sample was set to 14µm. The DC polarization varied from 0.3 to 2.8 kV. Emission current was measured with MV40 DC-MILLI-PICO-METER electrometer protected against short-circuit by neon lamp. The voltage was monitored through 1:1000 probe by Metex multimeter.

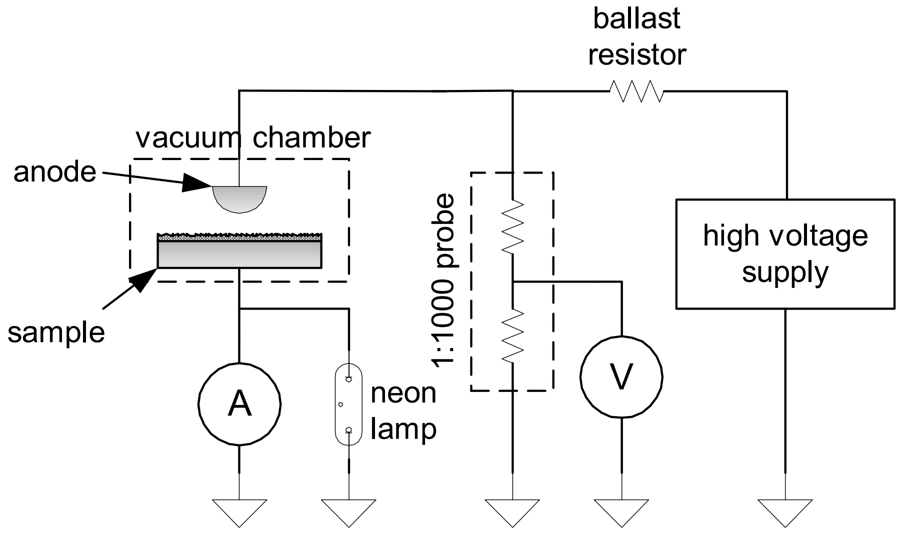

Figure 4.18 Scheme of field emission measurements system

CHAPTER 5

MICROSTRUCTURAL CHARACTERIZATION

5.1. FIELD EMITTING COATINGS (TITANIA)

5.1.1. Feedstock

5.1.1.1. Metco TiO_2 powder (APS and SUS B)

SEM

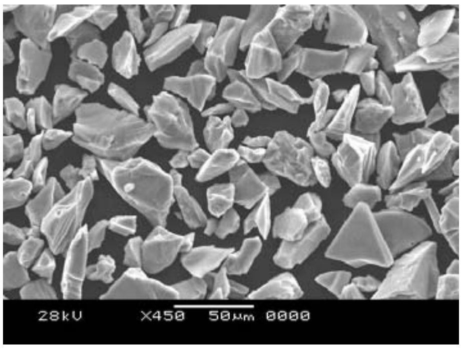

Figure 5.1 Morphology of METCO 102 TiO_2 powder (SEM secondary electrons).

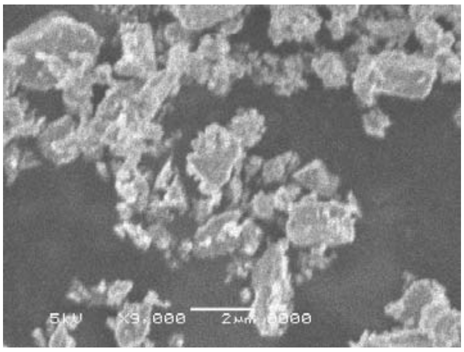

Figure 5.2 Morphology of 8 hours ball-milled TiO_2 powder (SEM secondary electrons).

Morphology of TiO_2 (Metco 102) ball milled for 8 hours is presented on Figure 5.2. The geometrical size of the powder grains are one order of magnitude smaller than in initial powder (Figure 5.1). Great majority of grains are submicrometer sized.

Granulometry

Granulometry measurements of initial Metco 102 and ball-milled after 3 and 8 hours showed the decrease of powder grain size with elongation of ball-milling time (Figure 5.3). Initial powder D[3,2] grains, defined by Masters [63], size was 23.34 µm. After 3 hours ball-milling D[3,2] decreased to 0.61 µm, finally 8 hours ball-milling changed powder grain size to D[3,2] = 0.45 µm. Shape of size distribution also changed, tail related with grains of size from 2 to 40 µm appeared after 8 hours milling. Possible explanation for that phenomenon could be evaporation of ethanol, cooling medium, during long time milling and resulting agglomeration of powder particles.

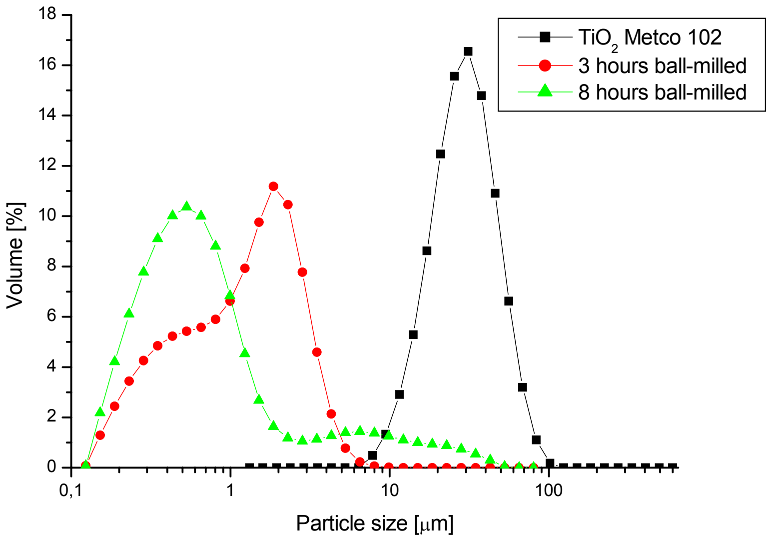

Figure 5.3 Result of granulometry analysis.

XRD

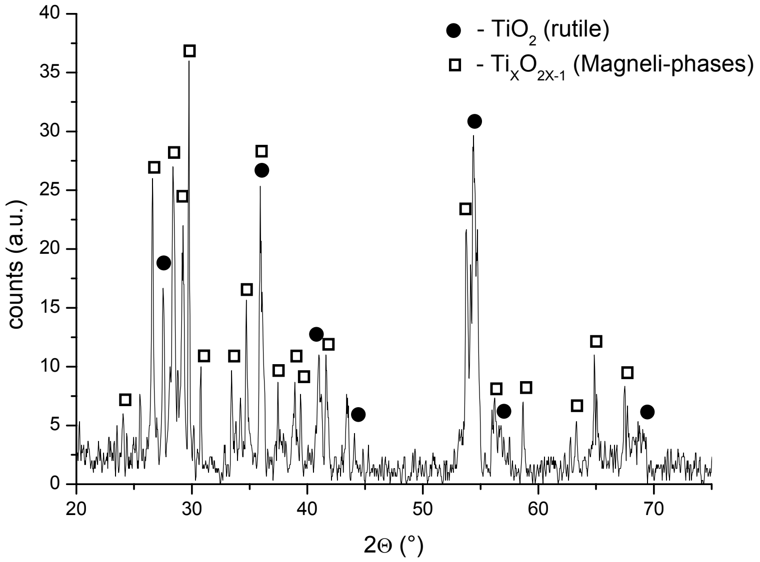

Figure 5.4 XRD diagram of TiO_2 Metco 102 powder.

The pattern of XRD analysis of initial TiO_2 Metco102 powder is shown in Figure 5.4. In studied powder, titania existed mainly in form of non-stoichiometric sub oxide Magneli phases Ti_xO_{2x-1} ($5 < x < 9$) [64] and rutile phase.

μ-Raman spectroscopy

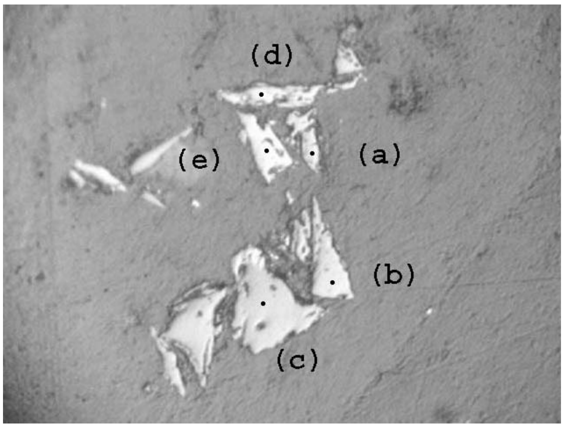

Figure 5.5 Positions of Raman spectroscopy spots of cross-sectioned TiO_2 Metco 102 powder (OM micrograph).

Figure 5.5 presents micrograph of cross-sectioned powder grains and marked Raman analysis spots. Corresponding spectra are shown in Figure 5.6. Spectra d,e are characterized by presence of bands at 144, 236, 440 and 604 cm^{-1} which confirms rutile like structure [65][66]**[43]**, however attenuation and shift of the bands, suggests existence of defected crystal structure, such as oxygen vacancies in Magneli phases [67]. Spectra a, b, c exhibit features of earlier mentioned rutile bands and in addition disorder induced bands at 320 – 360 cm^{-1} [65] probably related with Magneli phases.

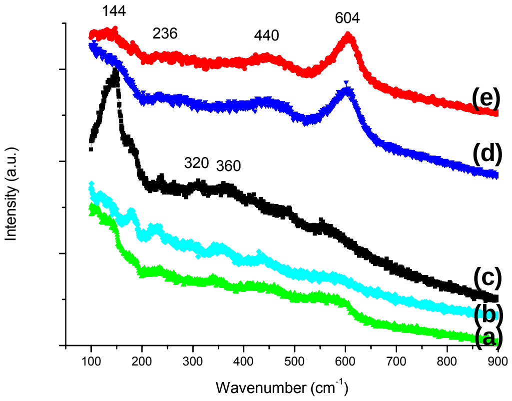

Figure 5.6 Raman spectra of TiO_2 Metco 102 powder.

XPS

Results of XPS quantitative analysis are presented in Table 5.1. The surface of the powder seems to be significantly contaminated by carbon (28.40%). The factor of atomic quantity of $O_{(O\text{-}Ti)}$, to Ti (42.85/21.68 = 1,97) being below the value of 2, indicates the slight substoichiometry of the titanium oxide.

Table 5.1 Results of quantitative analysis of TiO_2 Metco 102 powder

Element	**Orbit**	**$\%_{atom.}$**
$O_{(O\text{-}Ti)}$	1s	42.85
$O_{(OH)}$	1s	6.24
$O_{(O^2)}$	1s	0.83
Ti	2p	21.68
C	1s	28.40

The Ti 2p energy region presented in Figure 5.7 is characterized by doublet at 458.7 and 464.4 eV specific for tetravalent titanium cation Ti^{4+}, which indicates existence of TiO_2 [67][68][69]. Curve obtained from O 1s energy region (Figure 5.8) was resolved into three components, the main peak 530.1 eV corresponds to TiO_2, peak at 531.8 eV OH and peak 533,3 eV is attributed to contaminated O^{2-} organic molecules such as C=O, O-C=O [67][68][69].

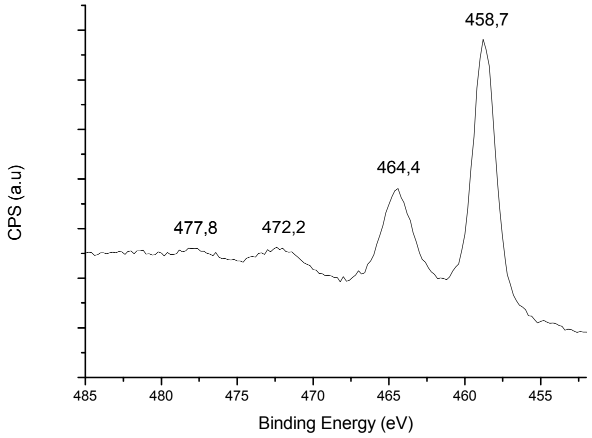

Figure 5.7 XPS spectrum of Ti 2p energy region of TiO_2 Metco 102 powder.

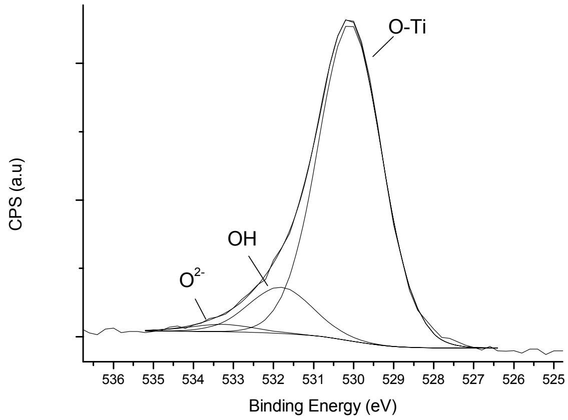

Figure 5.8 XPS spectrum of O 1s energy region of TiO_2 Metco 102 powder.

5.1.1.2 TiO_2 Huntsman powder

Granulometry

Particle size distribution of Huntsman powder is presented in Figure 5.9. Mean particle diameter D[3,2] equals 0,33 µm.

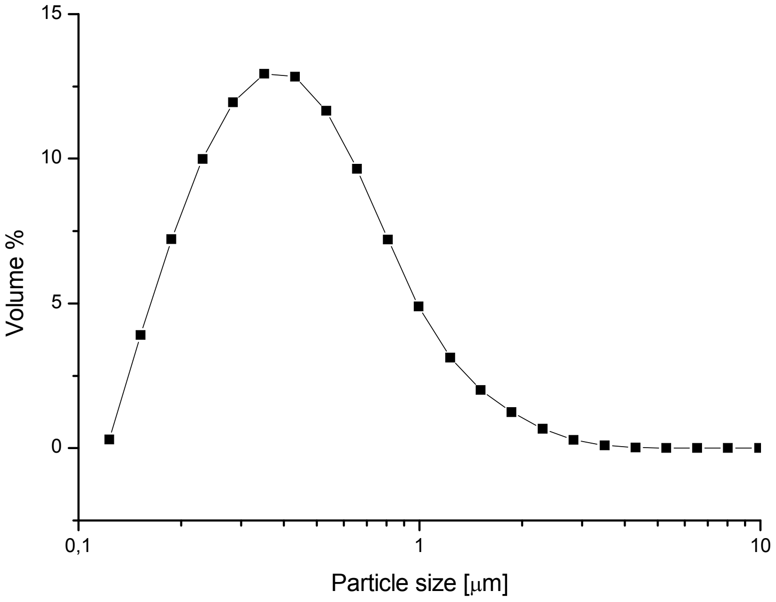

Figure 5.9 Granulometry analysis of TiO_2 Huntsman powder.

XRD

X-Ray diffraction pattern of TiO_2 Huntsman powder (Figure 5.10) corresponds exactly to rutile phase data base pattern.

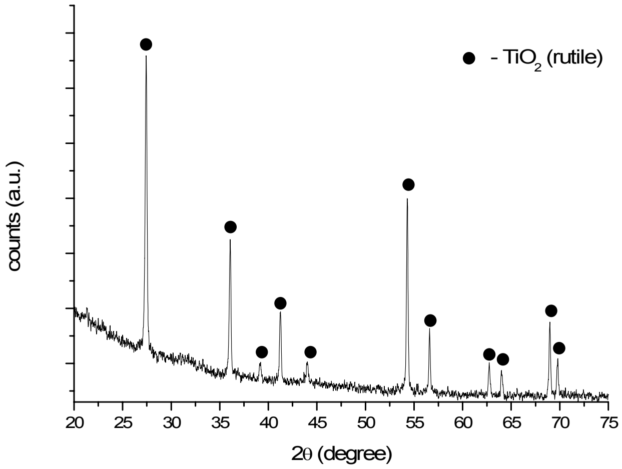

Figure 5.10 XRD diagram of TiO_2 Huntsman powder.

μ-Raman spectroscopy

Analysis of Huntsman powder resulted with only one kind of spectrum presented in Figure 5.11. Bands at 142, 238, 448, 611 cm^{-1} correspond to rutile phase.

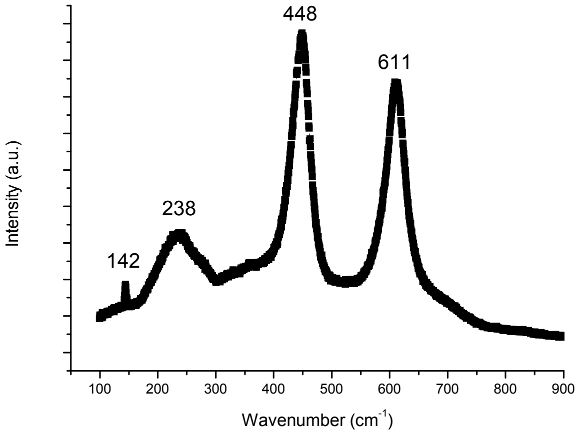

Figure 5.11 Raman spectra of TiO_2 Huntsman powder.

XPS

Table 5.2 Results of quantitative analysis of TiO_2 Huntsman powder

Element	**Orbit**	**$\%_{atom.}$**
$O_{(O\text{-}Ti)}$	1s	21,81
$O_{(O\text{-}Al,\ OH)}$	1s	28,54
$O_{(O^{2})}$	1s	3,74
Ti	2p	5,71
C	1s	23,38
Al	2p	16,82

Results of quantitative analysis are presented in table Table 5.2. Atomic percentage of titanium was estimated to only 5.71%, explanation for so low content could be the existence of carbon contamination 23.38 % and aluminium atoms 16.82 % in form of envelope coating of particles in accordance with powder technical bulletin.

Titanium energy region is presented in Figure 5.12, the typical peaks doublet is observed at 458.2 and 463.9 eV, which corresponds to tetravalent titanium cation in the bond with oxygen, Ti^{4+}-O. Spectrum of oxygen energy region presented in Figure 5.13 was resolved into following species: 529.8 eV is attributed to TiO_2, the most intense peak at 531.6 eV is ascribed to superposition of Al_2O_3, an envelope inorganic coating, and OH groups.

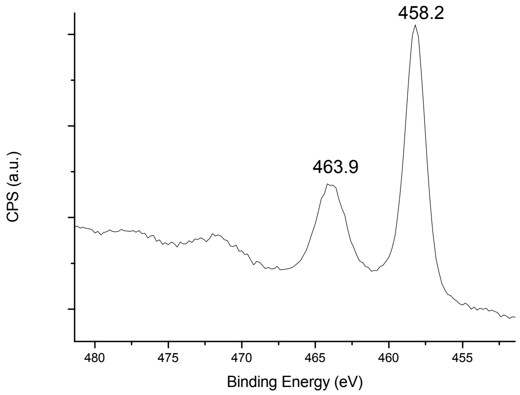

Figure 5.12 XPS spectrum of Ti 2p energy region of TiO_2 Huntsman powder.

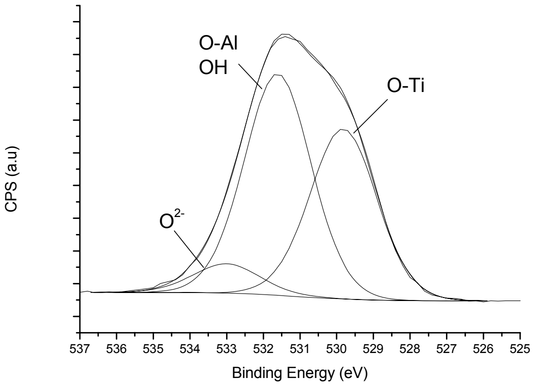

Figure 5.13 XPS spectrum of O 1s energy region of TiO_2 Huntsman powder.

5.1.2. Coatings

5.1.2.1. APS

SEM

Micrographs of APS coating are presented in Figure 5.14 - Figure 5.16. Figure 5.14 represents splat with diameter of about 80 µm, characterized by internal cracks. Cross-section of coating reveals porosities and vertical cracks (Figure 5.15). Coating thickness was estimated to 50-60 µm. Figure 5.16 presents surface artefacts originated from material vapour condensation.

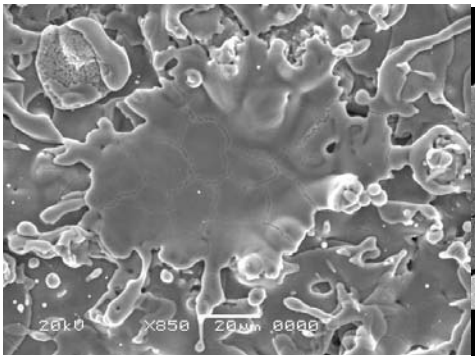

Figure 5.14 Micrograph of APS TiO_2 coating (SEM secondary electrons).

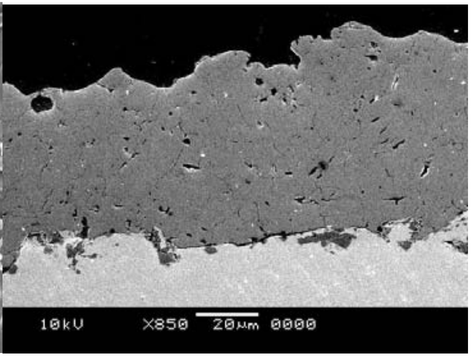

Figure 5.15 Micrograph of cross-sectioned APS TiO_2 coating (SEM secondary electrons).

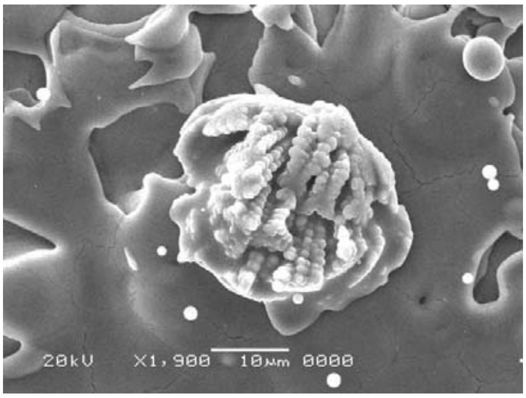

Figure 5.16 Material vapour condensation on TiO_2 coating (SEM secondary electrons).

XRD

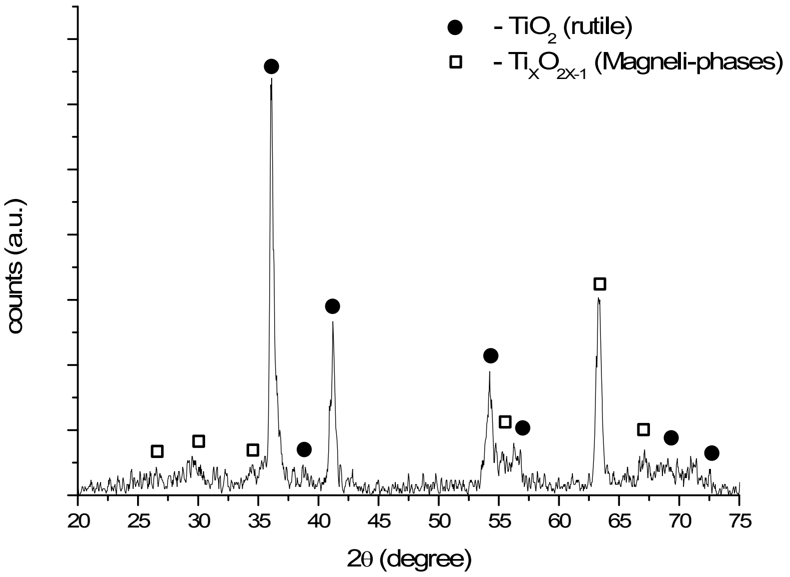

Figure 5.17 XRD diagram of APS coating.

XRD phase analysis showed existence of rutile as a major phase and a considerable contribution of Magneli phases (Figure 5.17). Obtained diagram suffers from absence of main rutile peak positioned at about 27.7 degree of 2θ, according to JCPDS-ICDD database. Phenomenon is related to texture of the coating.

μ-Raman spectroscopy

Different phases were investigated with use of Raman spectroscopy, Figure 5.18 shows cross-section of the coating and spots of analysis.

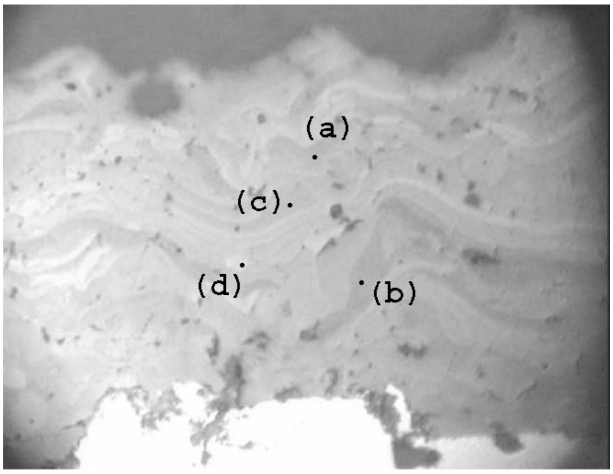

Figure 5.18 Positions of Raman spectroscopy spots of cross-sectioned APS coating (OM micrograph)

Spectrum corresponded to spot (d) give rise to intensity characteristic for rutile phase at 237, 440, 602 cm^{-1} (Figure 5.19). Broad bands and frequency shift of spectra a, b, c gives hints to presence of oxygen vacancy (Ti$_x$O$_{2x-1}$), low crystallinity and remaining stresses.

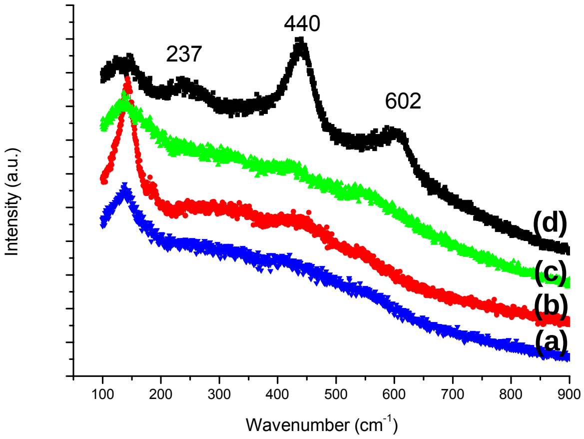

Figure 5.19 Raman spectra of APS coating

XPS

Table 5.3 Results of quantitative analysis of APS coating

Element	Orbit	$\%_{atom.}$
$O_{(O-Ti)}$	1s	51,06
$O_{(OH)}$	1s	5,72
Na	1s	7,69
Ti	2p	28,79
C	1s	6,74

Quantitative analysis (Table 5.3) showed considerable 7.69 % sodium contamination of unknown origin.

Spectra of Ti 2p energy region consisted dominantly of a doublet peaks at 458.4 and 464.2eV (Figure 5.20). These two major peaks were attributed to the tetravalent titanium cation, i.e. , Ti^{4+} $2p_{3/2}$ and Ti^{4+} $2p_{1/2}$.Oxygen energy region spectrum was resolved into two species, the major peak at 529.8 eV corresponded to O-Ti bond, peak at 531.6 eV attributed to OH (Figure 5.21).

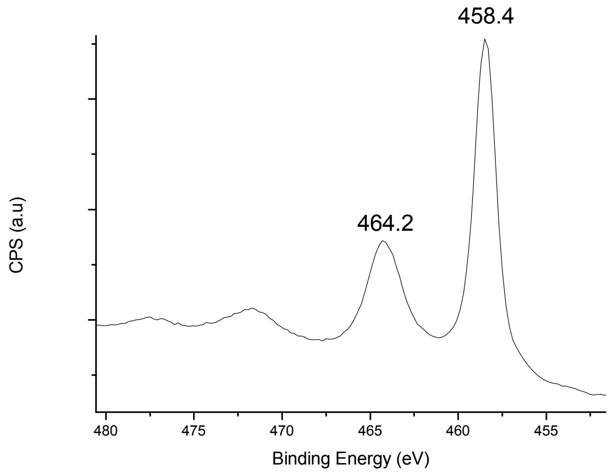

Figure 5.20 XPS spectrum of Ti 2p energy region of APS coating.

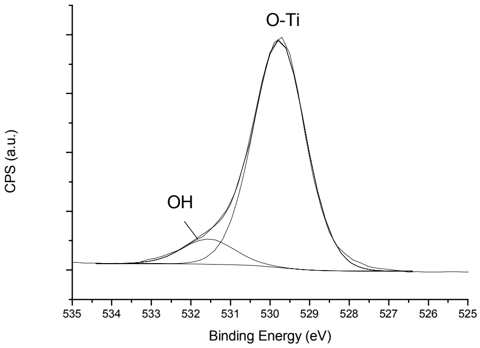

Figure 5.21 XPS spectrum of O 1s energy region of APS coating.

5.1.2.2. SPS B

SEM

Figure 5.22 shows cross-section of the coating, thickness was observed to be inhomogeneous and changed from 2 to 7 µm. Some of the substrate surface was found to be not covered by the sprayed material forming discontinuities in the coating. The reason of these discontinuities could be relatively high roughness of the substrate in comparison with coating thickness.

Figure 5.23 presents micrograph of the coating's surface, the evaluated sizes of splats are in range of 1 to 10 µm.

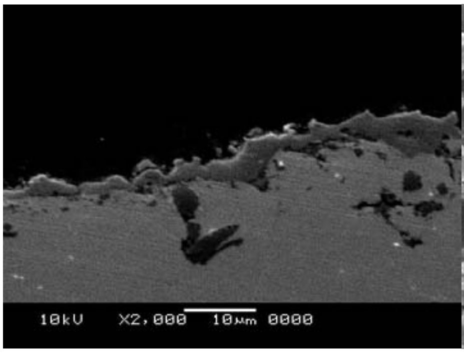

Figure 5.22 Micrograph of cross-sectioned SPS B TiO2 coating (SEM secondary electrons).

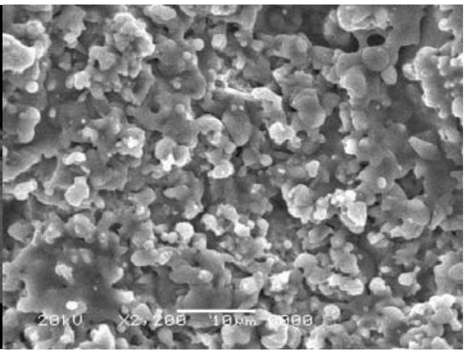

Figure 5.23 Micrograph of SPS B coating (SEM secondary electrons).

XRD

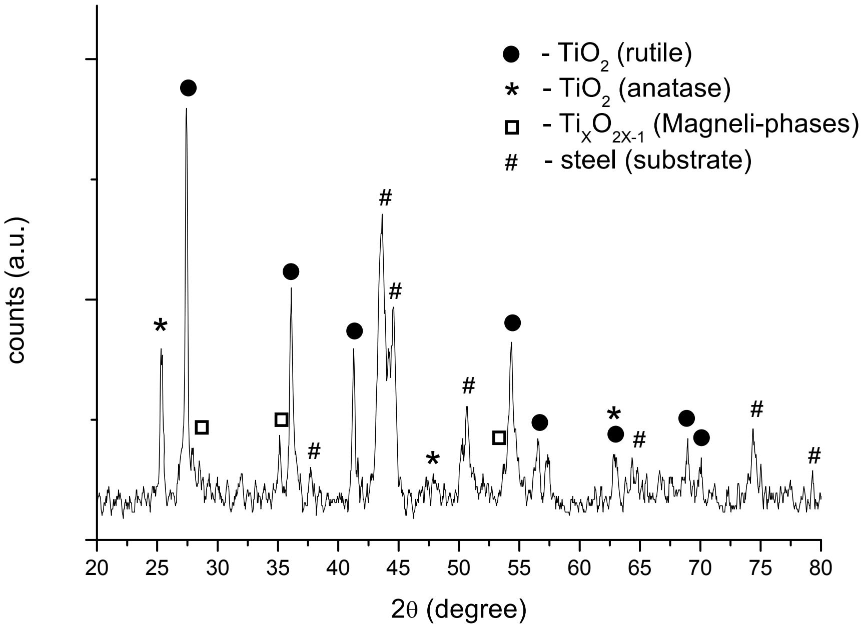

Figure 5.24 XRD diagram of SPS B coating

XRD phase analysis indicated co-existence of mainly rutile and some of anatase and Magneli phases. Considerable part of the peaks in the pattern is related to stainless steel - substrate material (Figure 5.24). Peaks related to coating material were observed to be switched for 0.370° 2Θ angle in comparison with reference patterns of JCPDS-ICDD database, effect wasn't observed in case of peaks of substrate material.

μ-Raman spectroscopy

Figure 5.25 shows cross-section of the coating with marked positions of Raman spectroscopy spots.

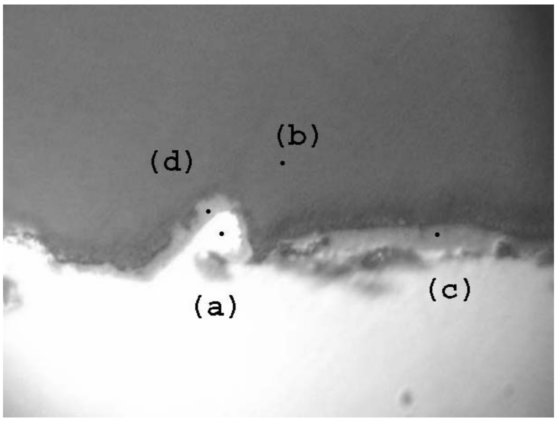

Figure 5.25 Positions of Raman spectroscopy analysis spots of cross-sectioned SPS B coating.

Featureless spectrum (a) is ascribed to substrate material - stainless steel, spectrum (b) indicates typical bands for epoxy resin (Figure 5.26). Analysis of spot (c) resulted in broad bands specific for rutile phase. Spectrum obtained from spot (d) seems to be the superposition of bands characteristic for rutile 147, 445, 609 and for anatase 147, 399, 516, 640 [65][66][43]

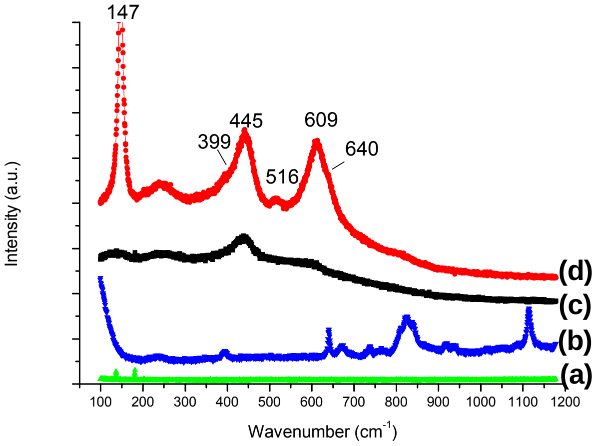

Figure 5.26 Raman spectra of SPS B coating.

XPS

Table 5.4 Results of quantitative analysis of SPS B coating.

Element	**Orbit**	**$\%_{atom.}$**
$O_{(O-Ti)}$	1s	42,11
$O_{(OH)}$	1s	7,87
$O_{(O^{2})}$	1s	2,87
Na	1s	5,00
Ti	2p	21,19
Ca	2p	1,07
C	1s	19,88

Quantitative analysis (Table 5.4) showed considerable 5.00 % sodium and 1.07 % calcium contamination of unknown origin.

Titanium energy region scan (Figure 5.27) revealed doublet at 458.5 and 464.2 eV, undoubtedly ascribed to Ti $2p_{3/2}$ and Ti $2p_{1/2}$, respectively, of tetravalent cation bonded with oxygen Ti^{4+}-O (TiO_2). Figure 5.28 presents resolved O 1s spectrum into contribution of TiO_2 at 529.8 eV, OH groups at 531.4 eV and 532.7 eV related to O^{2-} organic molecules such as C=O, O-C=O.

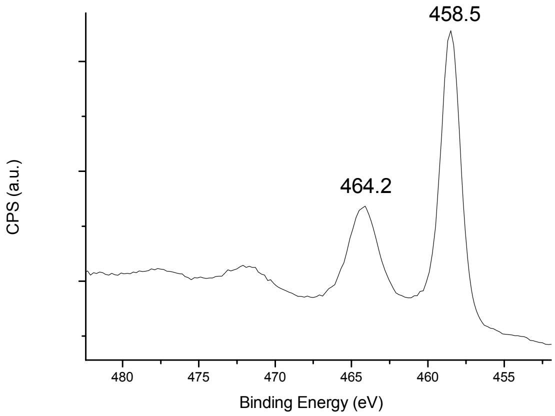

Figure 5.27 XPS spectrum of Ti 2p energy region of SPS B coating.

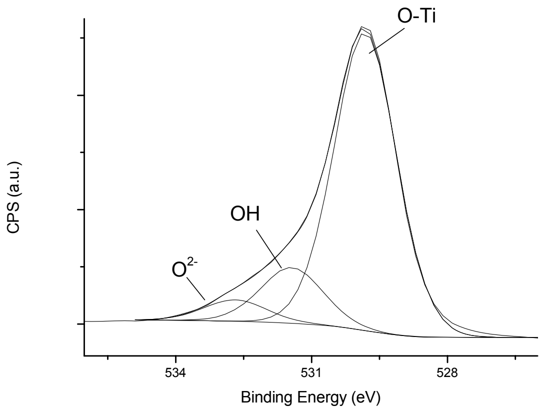

Figure 5.28 XPS spectrum of O 1s energy region of SPS B coating.

5.1.2.3. SPS A

SEM

Coating discontinuities are also observed in this case (Figure 5.29). The thickness was found to be from 1 to 5 µm. However in case of coatings sprayed with 6 times more passages (Figure 5.30), thickness was evaluated to be homogenously 10 µm.

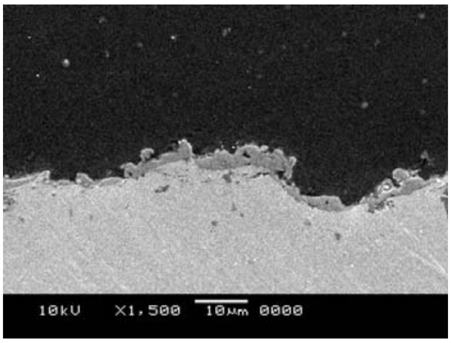

Figure 5.29 Micrograph of cross-sectioned SPS A TiO2 coating (SEM secondary electrons).

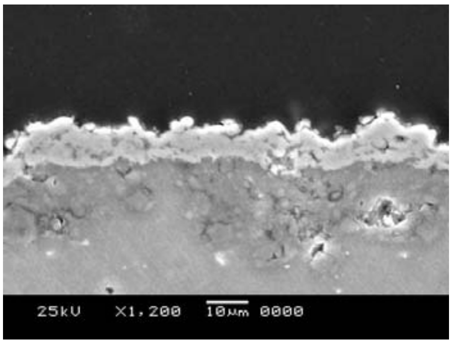

Figure 5.30 Micrograph of cross-sectioned SPS A TiO2 coating (SEM secondary electrons).

Observation of surface showed splats of sizes in range from 1 to 5 µm (Figure 5.31)

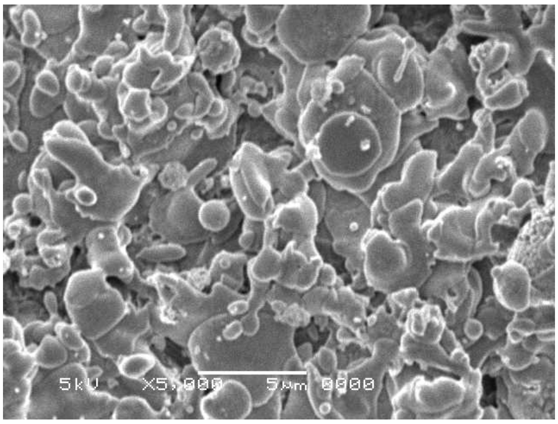

Figure 5.31 Micrograph of SPS A coating (SEM secondary electrons)

XRD

XRD analysis shows co-existence of several phases in the coating (Figure 5.32). The most intense peak is related with rutile phase, less intense peaks are imputed to anatase phase and Magneli phases. Considerable fraction of the peaks in the pattern is related to stainless steel - substrate material. Peaks related to coating material were observed to be switched for 0.370° 2Θ angle in comparison with reference patterns of JCPDS-ICDD database, effect wasn't observed in case of substrate material peaks.

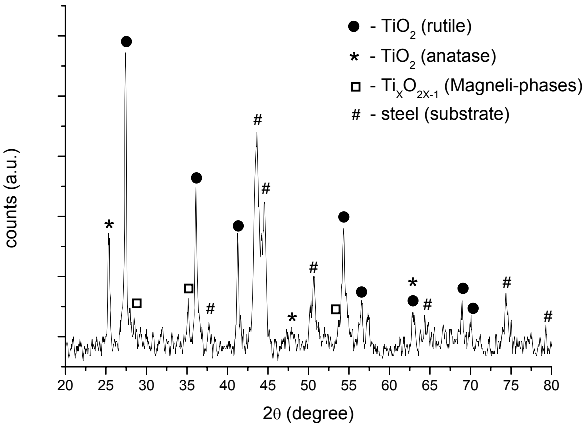

Figure 5.32 XRD diagram of SPS A coating

μ-Raman spectroscopy

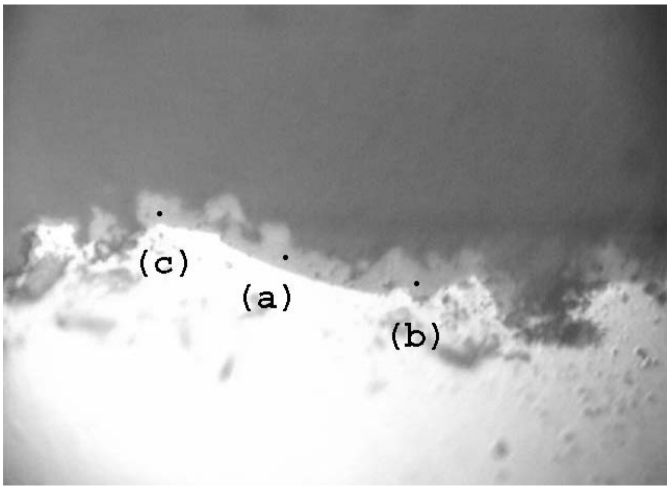

Figure 5.33 Positions of Raman spectroscopy analysis spots of cross-sectioned SPS A coating.

All spots of micro-Raman investigation (Figure 5.33) are found to be the superposition of rutile 445, 609 cm^{-1} and anatase 153, 399, 516, 640 cm^{-1} (Figure 5.34)

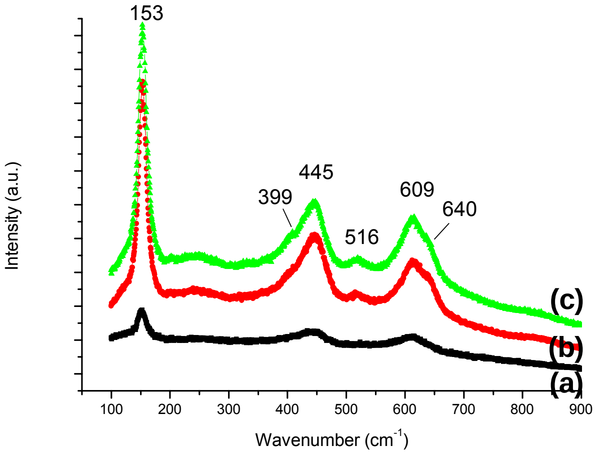

Figure 5.34 Raman spectra of SPS A coating

XPS

Table 5.5 Results of quantitative analysis of SPS A coating

Element	**Orbit**	**$\%_{atom}$**
$O_{(O\text{-}Ti)}$	1s	34.44
$O_{(O\text{-}Al,\ OH)}$	1s	13.64
$O_{(O^{2})}$	1s	4.92
Ti	2p	15.3
C	1s	12.2
Al	2p	10.2
Na	1s	7.1
Si	2p	2.3

Quantitative analysis is presented in Table 5.5. Titanium atomic content was estimated to 15.3%, aluminium atomic percentage was 10.2%. Plasma spraying introduced substantial impurities of Na and Si atoms, 7.1% and 2.3% respectively.

Titanium energy region spectrum (Figure 5.35) is characterized by doublet at 458.5 and 464.2 eV specific for tetravalent titanium cation Ti^{4+}-O.

Figure 5.36 presents resolved O 1s spectrum, major peak at 530.0 eV corresponds to TiO_2, peak at 531.5 eV was attributed to Al_2O_3 and OH groups, and finally peak at 533.0 eV represents O^{2-} organic molecules.

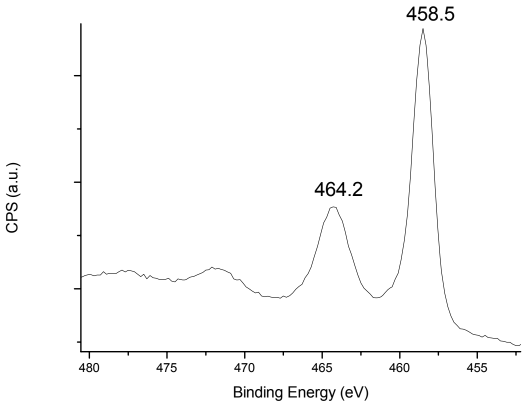

Figure 5.35 XPS spectrum of Ti 2p energy region of SPS A coating.

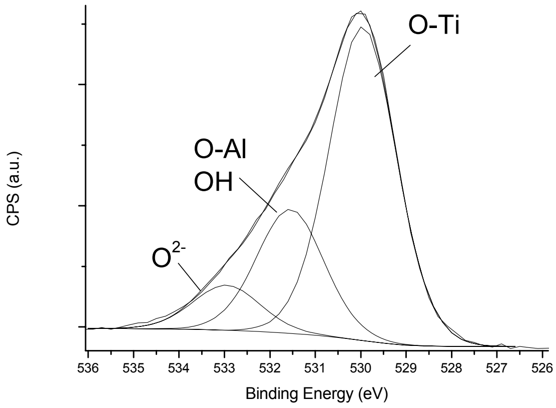

Figure 5.36 XPS spectrum of O 1s energy region of SPS A coating.

5.1.2.4. GRAD – 2 layered (APS – bottom, SPS A – top)

SEM

Micrograph of cross-sectioned coating is presented in Figure 5.37. Bottom layer plasma sprayed with Metco 102 powder is characterized by considerable porosities, interlamellar cracks and thickness of about 30 to 50 µm. Top layer sprayed with SPS A is inhomogeneous in thickness, which changes in range from 1 - 8 µm, discontinuities are also observed. Interface between both layers is sharply outlined, which could suggest low adhesion strength.

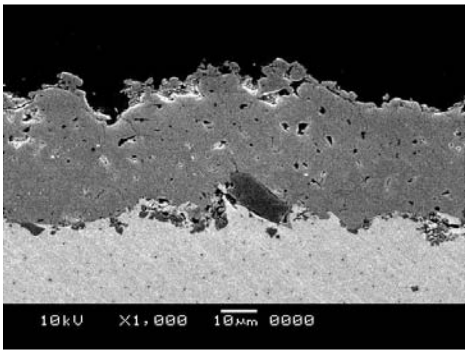

Figure 5.37 Micrograph of cross-sectioned GRAD TiO_2 coating (SEM secondary electrons).

XRD

Phase analysis using XRD indicated existence of phases present in APS and SPS A coating rutile, anatase, Magneli phases (Figure 5.38). Some of the peaks are split, that phenomena could be explained by superposition of switched peaks originated from stressed top SPS A coating and peaks from bottom APS coating

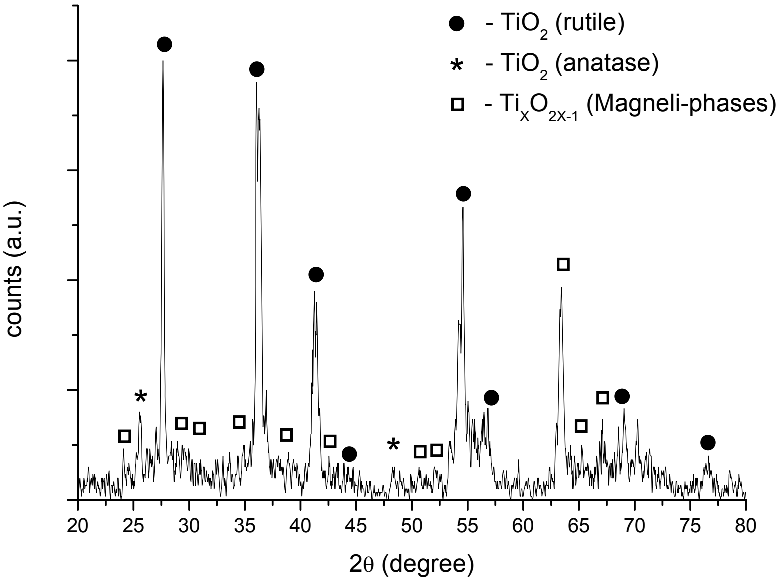

Figure 5.38 XRD diagram of GRAD coating

μ-Raman spectroscopy

Figure 5.39 presents optical micrograph of GRAD coating with marked spots of Raman investigation. Spots (e), (f) correspond to top layer sprayed with use of suspension, resulted spectrum (f) is characterized by contribution of the bands of rutile 445, 609 and anatase 153, 399, 516, 640, spectrum (e) give rise to rutile only bands (Figure 5.40). Spectra (a), (b), (c), (d) resulted from APS – bottom layer posses rutile-like structure, however broad band and slight frequency shift suggests low crystallinity, residual stresses or defects such as oxygen vacancies Ti_xO_{2x-1}.

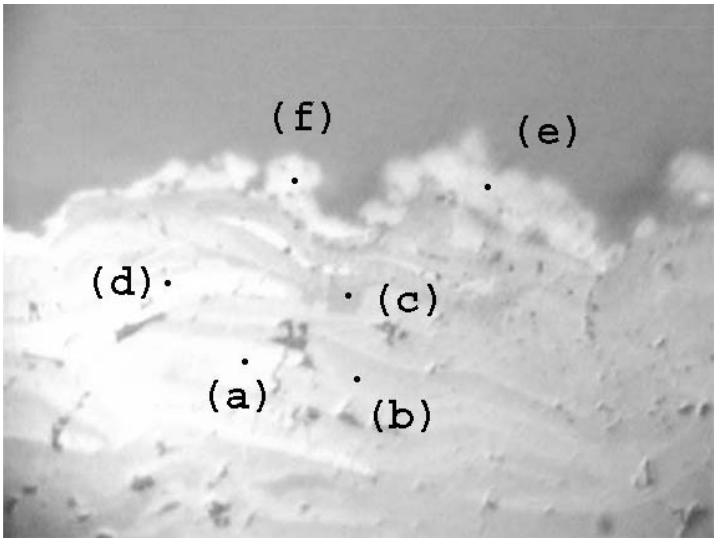

Figure 5.39 Positions of Raman spectroscopy analysis spots of cross-sectioned GRAD coating

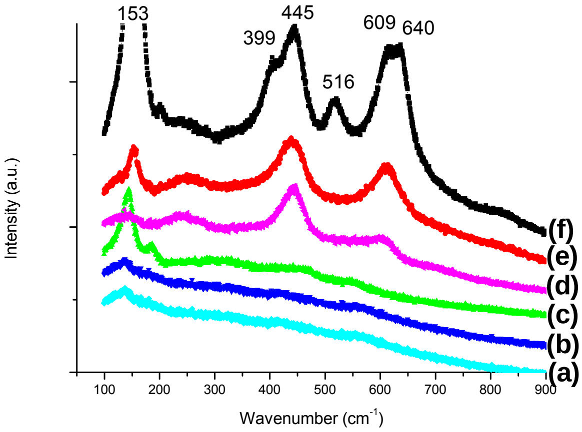

Figure 5.40 Raman spectra of GRAD coating

5.2. BIOCOMPATIBLE COATINGS (HYDROXYAPATITE / TITANIA)

5.2.1. Feedstock

5.2.1.1. HAp Tomita powder

Granulometry

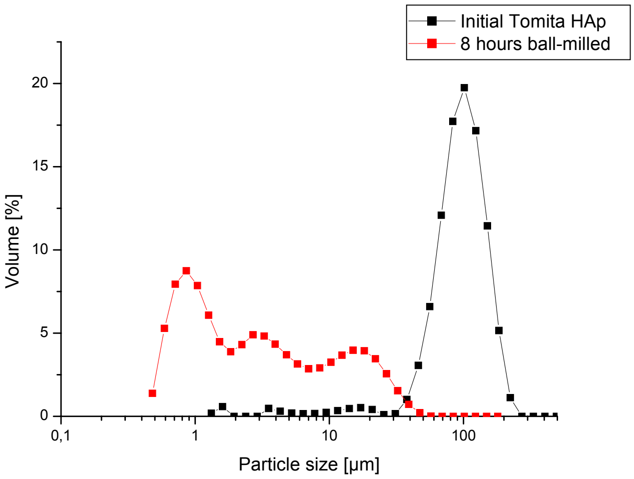

Figure 5.41 Granulometry analysis of HAp initial and ball-milled powders

Granulometry measurements of initial and 8 hours ball-milled HAp powders are presented in Figure 5.41. Initial HAp powder contains mainly grains of volume-surface mean diameter (defined, e.g., by Masters [63]) D[3,2] = 44.09 µm and D(v, 0.5) = 87.73 µm. After 8 hours ball-milling grain size distribution compose of three fractions: submicrometer, single micrometers and tens of micrometers. Resulting mean sizes are D[3,2] = 1.47 µm and D(v, 0.5) = 2.23 µm.

XRD

Both X-Ray patterns of HAp initial and ball-milled powders are presented in Figure 5.42. Initial HAp as well as ball-milled powder patterns contain reflexes corresponding to hydroxyapatite phase.

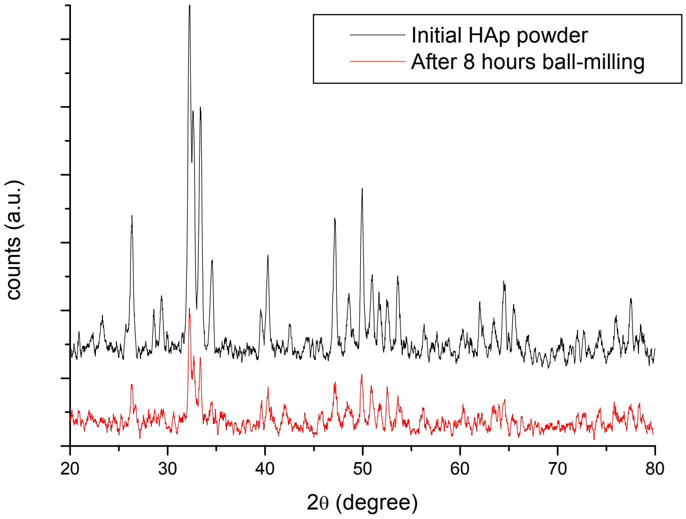

Figure 5.42 X-ray diffraction pattern of HAp initial and ball-milled powders

µ-Raman spectroscopy

Crystal phase determination with use of µ-Raman spectroscopy is presented in Figure 5.43. Spectra of initial and ball milled powder are exactly the same. Both are characterized by bands in range of 400-490, 570-625, 1020-1095cm^{-1} and very intense peak at 962 cm^{-1}. Mentioned bands correspond to hydroxyapatite crystal phase [70][71][72].

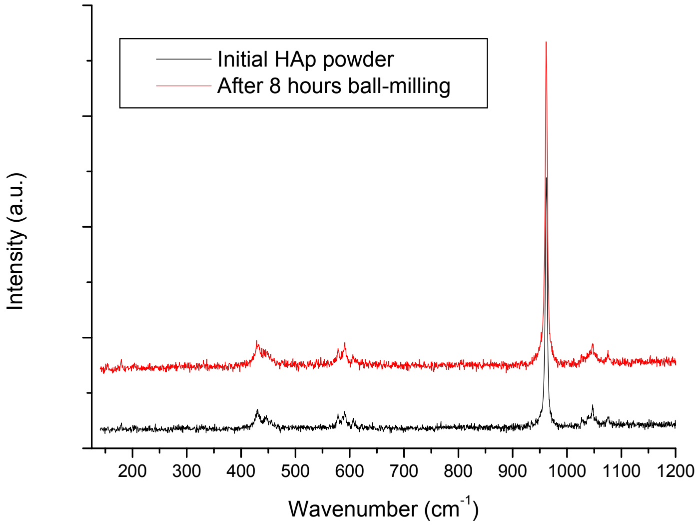

Figure 5.43 µ-Raman spectra of HAp initial and ball-milled powders

XPS

XPS spectra of HAp initial and ball-milled powders are presented in Figure 3.44 - Figure 5.47.

Spectra of O 1s and P 2p present single peaks at 531.0 and 133.1 eV, respectively. Ca energy region contains doublet of Ca $2p_{3/2}$ and Ca $2p_{1/2}$ at 347.1 and 350.6 eV. In case of C 1s energy region, spectrum of initial powder is composed of two peaks at 285 and 289.2 eV corresponding to contamination carbon and CO_3 carbonate group [73][74]. C 1s region of ball-milled powder contain peak at 285-284,6 eV with higher intensity. Origin of this intensity increase could be contamination by ethanol during ball-milling process.

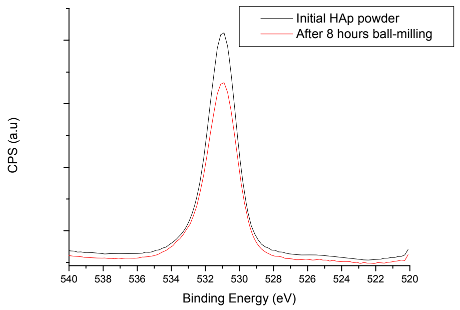

Figure 5.44 XPS spectrum of O 1s energy region of HAp initial and ball-milled powders.

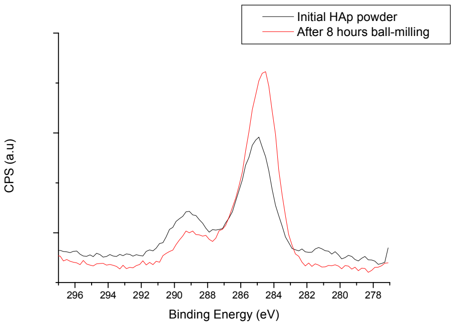

Figure 5.45 XPS spectrum of C 1s energy region of HAp initial and ball-milled powders.

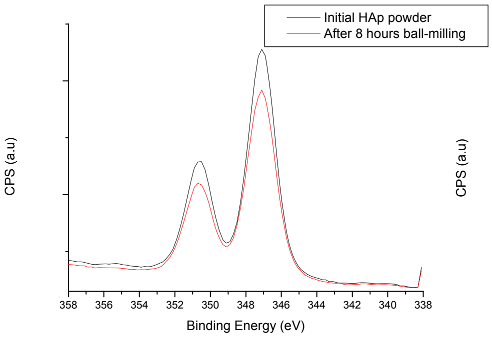

Figure 5.46 XPS spectrum of Ca 2p energy region of HAp initial and ball-milled powders.

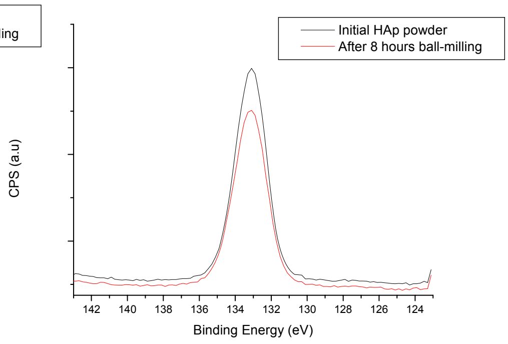

Figure 5.47 XPS spectrum of P 2p energy region of HAp initial and ball-milled powders.

Quantitative analysis confirms higher contamination of ball-milled powder with carbon species (Table 5.6). Within initial powder carbon atomic percentage was 7.5. After ball-milling, carbon atomic content increased to 11.8 %.

Table 5.6 XPS quantitative analysis results.

Sample	**Peak**	**$\%_{atom}$**	**Ca/P ratio**
Initial HAp powder			
	O 1s	54.6	1.38
	Ca 2p	22.0	
	P 2p	15.9	
	C 1s	7.5	
8h ball-milled HAp			
	O 1s	52.1	
	Ca 2p	20.9	1.37
	P 2p	15.2	
	C 1s	11.8	

5.2.2. Coatings

5.2.2.1. Samples A1 and A2 – single layered suspension plasma sprayed HAp

SEM

Cross section micrographs of sample A1 (arc power – 35kW) is presented in Figure 5.48 and Figure 5.50. Whereas, Figure 5.49 and Figure 5.51 present cross-section of sample A2 being sprayed with 40 kW of arc power. Coatings seem to be 10 to 20 µm thick and considerably porous. Important difference between sample A1 and A2 is the quality of the coating-substrate interface. Sample A1 appears to be weakly attached to substrate, manifested by voids in the interface (Figure 5.50 – look arrow). In case of sample A2, presence of interface voids is lower (Figure 5.51).

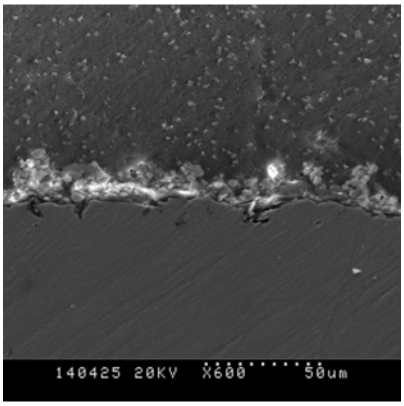

Figure 5.48 Micrograph of cross-sectioned sample A1 (magn. X 600)

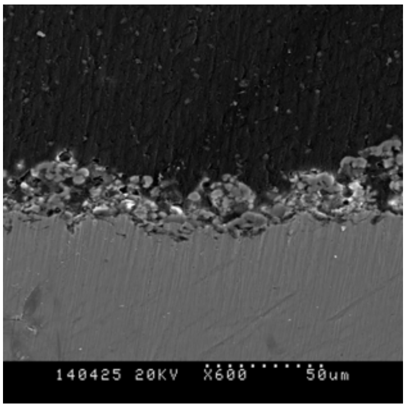

Figure 5.49 Micrograph of cross-sectioned sample A2 (magn. X 600)

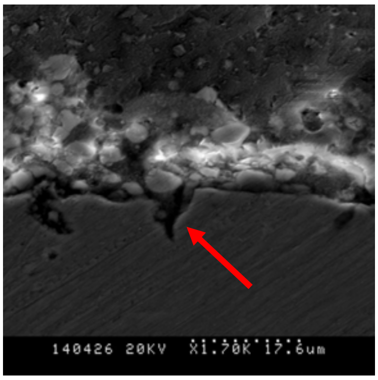

Figure 5.50 Micrograph of cross-sectioned sample A1 (magn. X 1,7k)

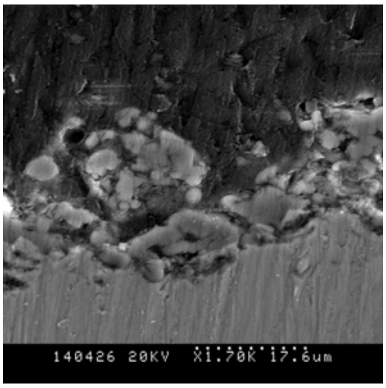

Figure 5.51 Micrograph of cross-sectioned sample A2 (magn. X 1,7k)

XRD

Sample A1 and A2 are composed of several phases (Figure 5.52). The main one is HAp phase, however some reflexes correspond to decomposition phases such as, α-TCP, β-TCP, TTCP. Additionally, patterns contain titanium reflexes originated from substrate. Relative intensity of titanium peaks differs between sample A1 and A2, being less significant for sample A2. This phenomenon proves the greater thickness and/or density of sample A2.

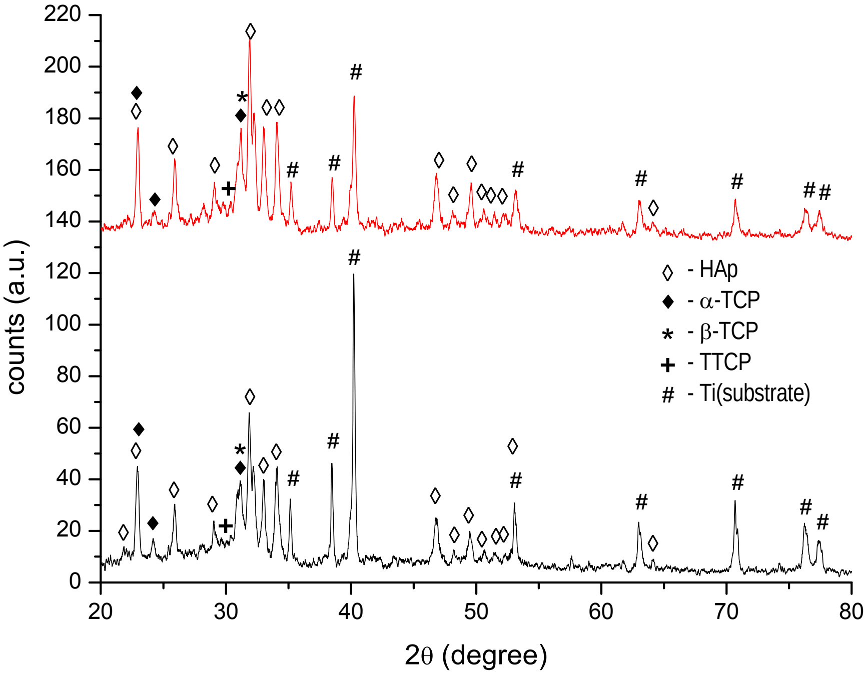

Figure 5.52 X-ray diffraction pattern of sample A1 (bottom) and sample A2 (top)

μ-Raman spectroscopy

Figure 5.53 shows Raman spectra obtained from sample A1 and A2. Observed bands at 400-490, 570-625, and 1020-1095cm^{-1} can be ascribed to HAp phase. However, presence of superposed peaks around 960 cm^{-1} originate from decomposition phases (α-TCP, β-TCP, TTCP) [70][71][72].

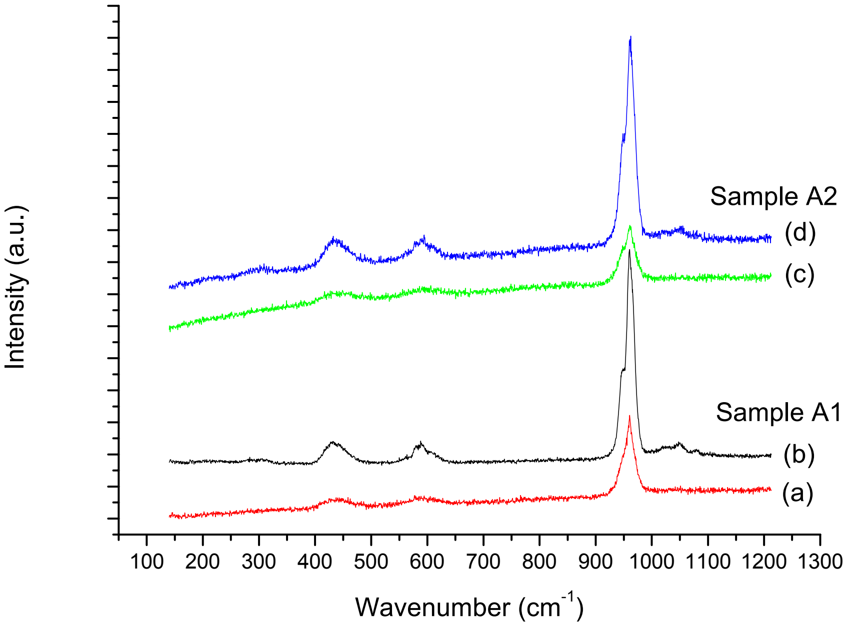

Figure 5.53 μ-Raman spectra for two randomly chosen spots for each sample (a, b – A1; c, d – A2)

5.2.2.2. Samples B1 and B2 – double layered SPS HAp on APS HAp coating

SEM

Figure 5.54– Figure 5.59 show cross-sections of samples B1 and B2. Double layer structure of the coatings is observed. The bottom, ~100µm thick layer obtained by coarse HAp powder spraying is characterized by dense, cracked structure (Figure 5.56 and Figure 5.57). The top layer sprayed with suspension is 10-20 µm thick and very porous. Earlier observed difference of interface between 35 and 40 kW sprayed coating is also observed in this case. Sample B2 sprayed with power 40 kW seems to be more adherent to bottom layer.

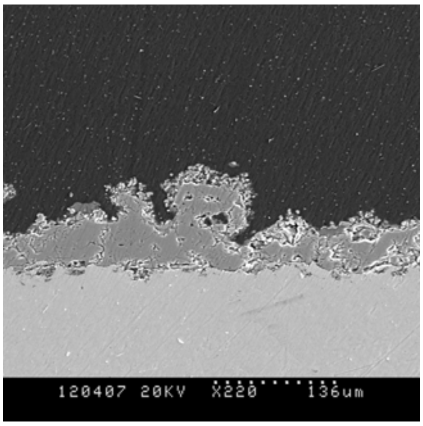

Figure 5.54 Micrograph of cross-sectioned sample B1 (magn. X 220)

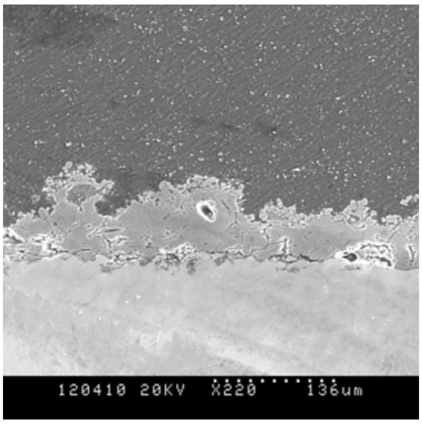

Figure 5.55 Micrograph of cross-sectioned sample B2 (magn. X 220)

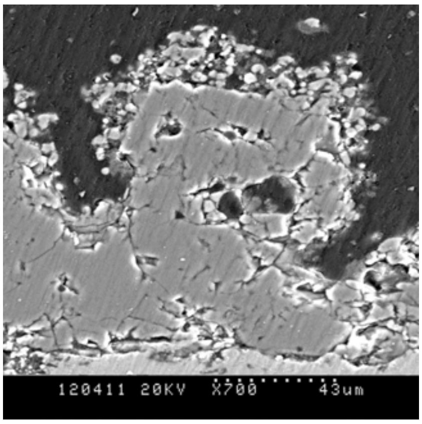

Figure 5.56 Micrograph of cross-sectioned sample B1 (magn. X 700)

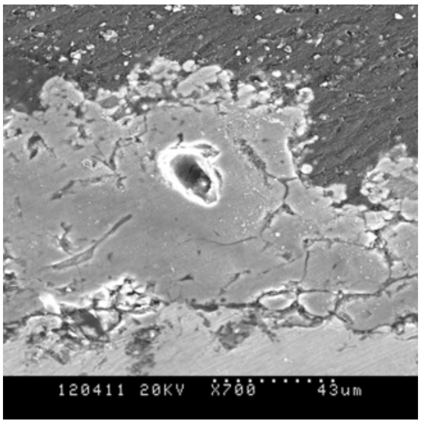

Figure 5.57 Micrograph of cross-sectioned sample B2 (magn. X 700)

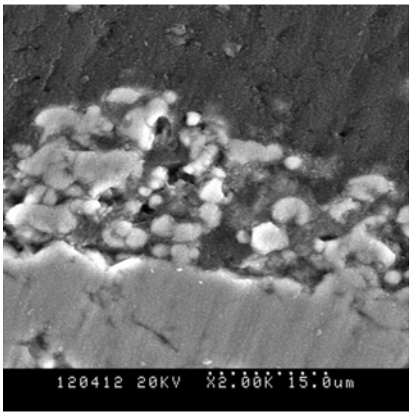

Figure 5.58 Micrograph of cross-sectioned sample B1 (magn. X 2k)

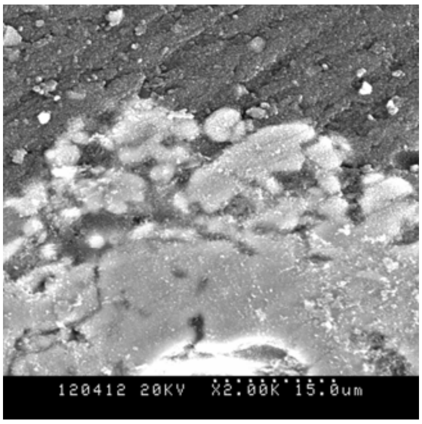

Figure 5.59 Micrograph of cross-sectioned sample B2 (magn. X 2k)

XRD

HAp crystal phase is the main one observed in X-ray diagrams shown in Figure 5.60. Few peaks point out presence of decomposition phases (α-TCP, β-TCP, TTCP). Intensities of the decomposition phases peaks at 24.3°, 31.0°, 35.6° and 37.5° of 2theta angles are higher for sample B2, which is explained by greater decomposition of the HAp occurring with high arc power of (40kW).

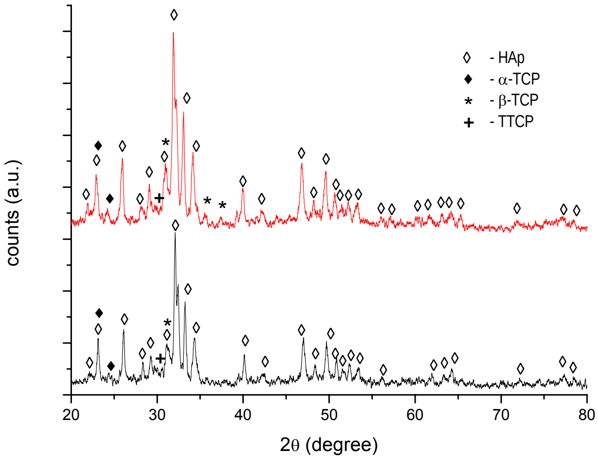

Figure 5.60 X-ray diffraction pattern of sample B1 (bottom) and sample B2 (top)

μ-Raman spectroscopy

Raman spectra presented in Figure 5.61, are similar to earlier obtained for sample B1 and B2. Observed bands at 400-490, 570-625, and 1020-1095cm^{-1} are ascribed to HAp phase. Superposed peaks around 960 cm^{-1} originate from decomposition phases.

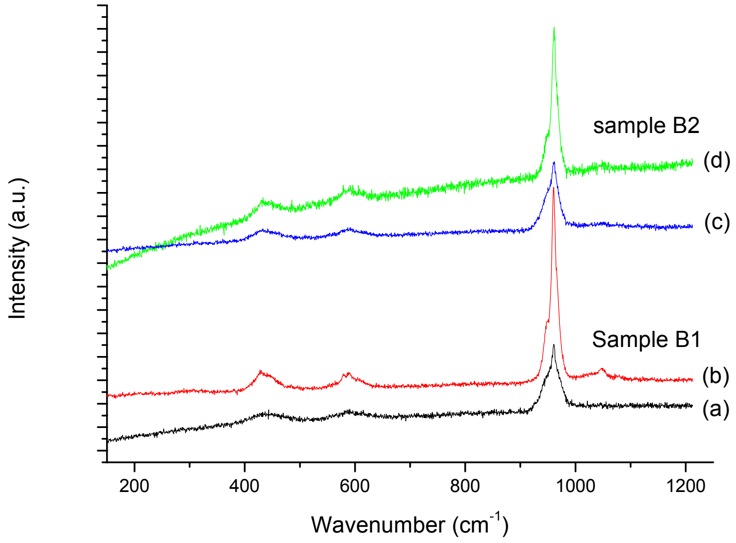

Figure 5.61 μ-Raman spectra for two randomly chosen spots for each sample (a, b – B1; c, d – B2)

5.2.2.3. Samples C1 and C2 – double layered SPS HAp on SPS TiO_2

SEM

Cross-section micrographs of sample C1 i C2 are presented in Figure 5.62 - Figure 5.65. Though the coatings are double layered (bottom – SPS TiO_2, top – SPS HAp), the interface between layers is indistinguishable. Coating thickness is of about 10 – 20 µm.

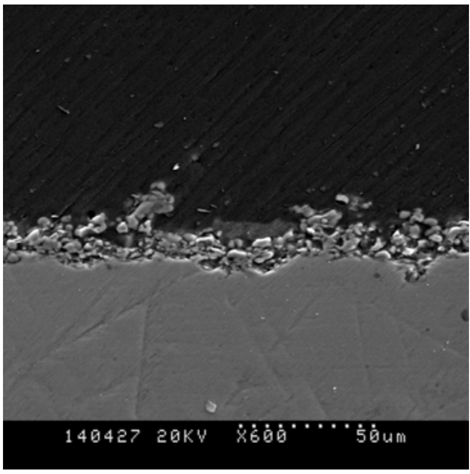

Figure 5.62 Micrograph of cross-sectioned sample C1 (magn. X 600)

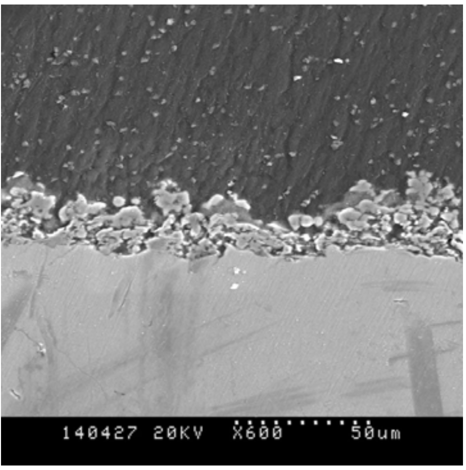

Figure 5.63 Micrograph of cross-sectioned sample C2 (magn. X 600)

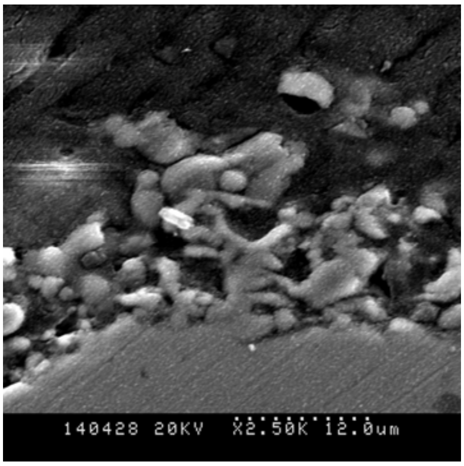

Figure 5.64 Micrograph of cross-sectioned sample C1 (magn. X 2.5k)

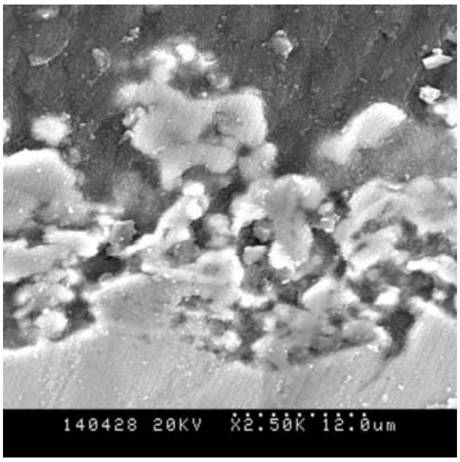

Figure 5.65 Micrograph of cross-sectioned sample C2 (magn. X 2.5k)

Obtained WDS micrographs with Ti, P, Ca material contrast allowed to confirm double layered structure of the sample C1. One can see on Figure 5.66 , presence of Ti in substrate and bottom layer. The top layer is visible under P and Ca contrast.

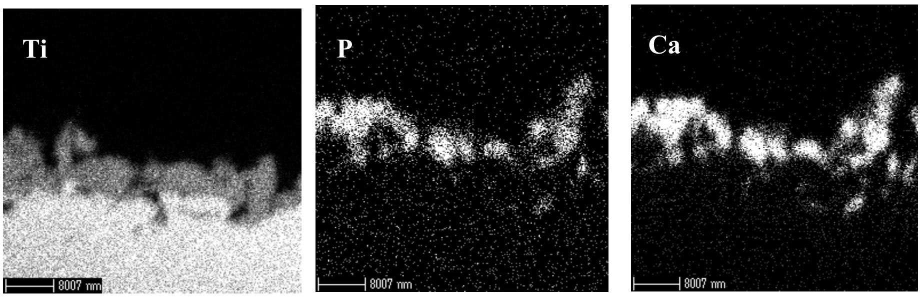

Figure 5.66 WDS micrograph of cross-sectioned sample C1 with Ti, P, Ca material contrast

XRD

X-ray diagrams of sample C1 and C2 are shown in Figure 5.67. Due to low density or/and low thickness of the layers, X-ray penetration depth is sufficient to observe phase composition of bottom layer or even substrate.

Rutile crystal phase originated from bottom TiO_2 is the main one observed in X-ray diagrams. Moreover, formation of metastable anatase phase was indicated by presence of corresponding peaks.

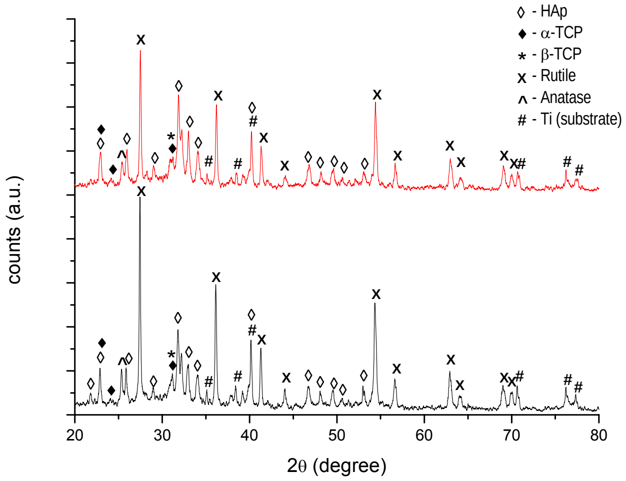

Figure 5.67 X-ray diffraction pattern of sample C1 (bottom) and sample C2 (top)

μ-Raman spectroscopy

Raman spectra of sample C1 and C2 are presented in Figure 5.68 and Figure 5.69, respectively. Spectra (Figure 5.68b) and (Figure 5.69a) were obtained from the spots localized in the bottom of porosities observed perpendicularly to surface. Mentioned spectra are the superposition of bands corresponding to anatase (152, 399, 517, 640 cm^{-1}) and rutile (152, 235, 445, 607 cm^{-1}) phase bands earlier also observed by Tomaszek *et al.* (2005) in suspension plasma sprayed TiO_2 coatings. In case of sample spectrum (Figure 5.69)a , bands of rutile and anatase are superposed with bands of HAp - 400-490, 570-625, 960 and 1020-1095cm^{-1}. Broadening of the 960 cm^{-1} peak towards 930 cm^{-1} correspond α-TCP, β-TCP, TTCP decomposition phases. Remaining spectra, obtained from surface of the coating, indicate high content of HAp and decomposition phases, however weak peak at 152 cm^{-1} corresponding to rutile/anatase.

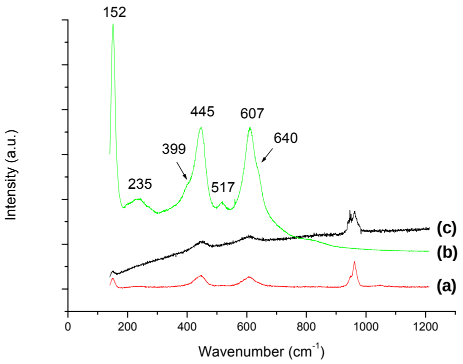

Figure 5.68 μ-Raman spectra of sample C1

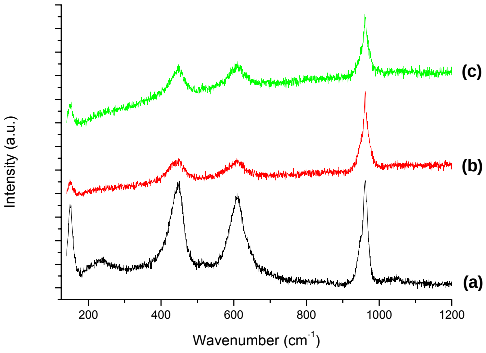

Figure 5.69 μ-Raman spectra of sample C2

5.2.2.4. Samples D1 and D2 – gradient TiO_2 - HAp coating

SEM

Sample D1 and D2 cross-section micrographs are shown by Figure 5.70 - Figure 5.73. The coatings are about 30-40µm thick and porous.

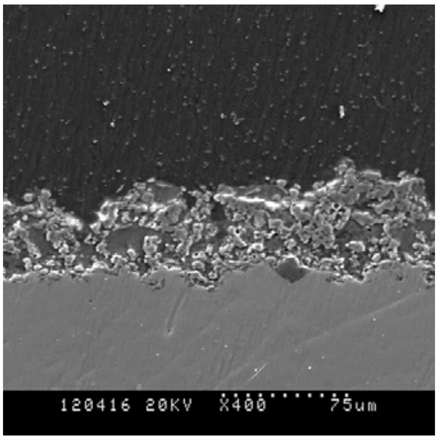

Figure 5.70 Micrograph of cross-sectioned sample D1 (magn. X 400)

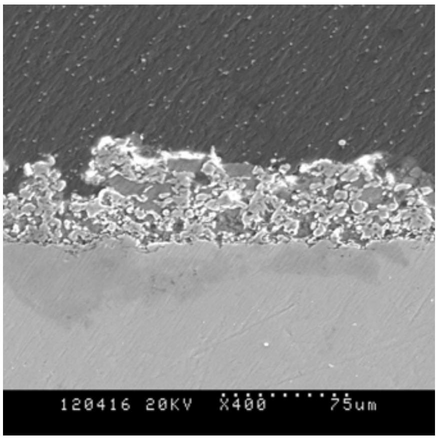

Figure 5.71 Micrograph of cross-sectioned sample D2 (magn. X 400)

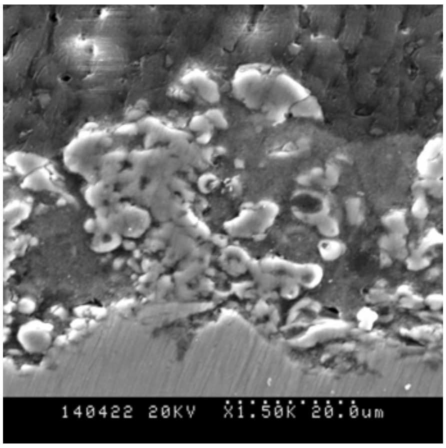

Figure 5.72 Micrograph of cross-sectioned sample D1 (magn. X 1.5k)

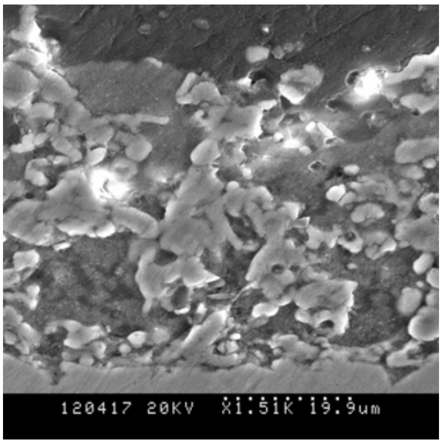

Figure 5.73 Micrograph of cross-sectioned sample D2 (magn. X 1.5k)

Results of analysis with use of WDS – Ti, Ca, P material contrast allowed to observe gradient structure of the coating D1. Figure 5.74 presents Ti, P and Ca material contrast. Content of Ca and P atoms is low at substrate-coating interface and increases towards the surface. The reverse effect is observed under Ti material contrast – high content of Ti atoms at the substrate-coating interface and decrease towards the surface.

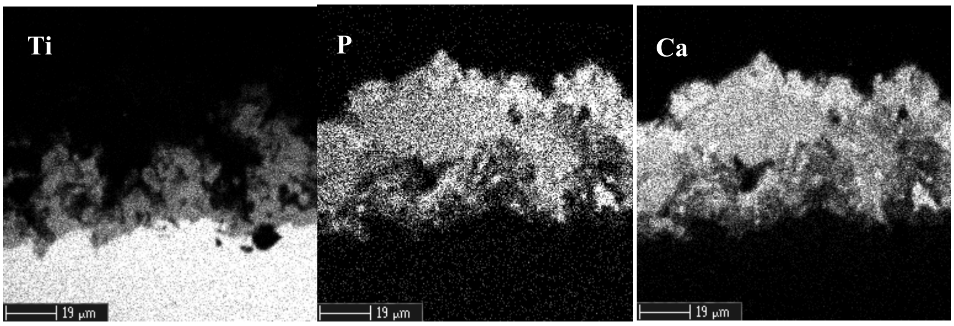

Figure 5.74 WDS micrograph of cross-sectioned sample D1 with Ti, P, Ca material contrast

XRD

X-Ray diffraction patterns of sample D1 and D2 present variety of phases (Figure 5.75). The most intense peaks correspond to HAp phase. The minor are α-TCP, β-TCP, TTCP, CaO decomposition phases and rutile phase. Important difference between sample D1 and D2 diagrams is the intensity of CaO phase and rutile phase being higher for sample D2 – sprayed with arc power of 40kW.

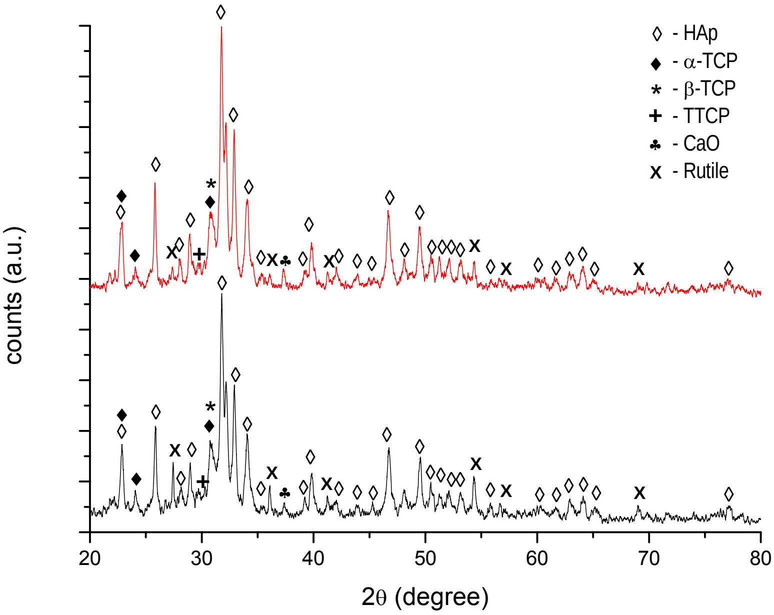

Figure 5.75 X-ray diffraction pattern of sample D1 (bottom) and sample D2 (top)

μ-Raman spectroscopy

Raman spectra of sample D1 and D2 were presented in Figure 5.76. Observed bands at 400-490, 570-625, 1020-1095cm^{-1} and intense peak 930 cm^{-1} are ascribed to HAp phase. Moreover, arise to the band at 930-960 cm^{-1} corresponds to are α-TCP, β-TCP, TTCP decomposition phases.

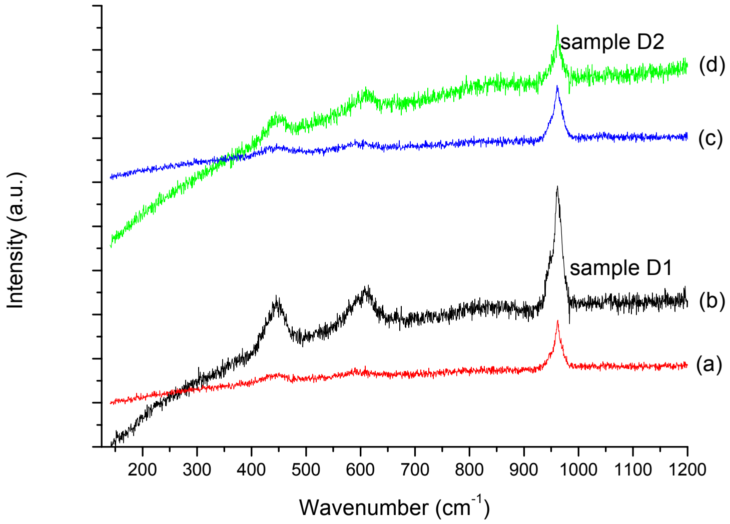

Figure 5.76 μ-Raman spectra for two randomly chosen spots for each sample (a, b – D1; c, d – D2)

XPS

XPS spectra of HAp initial and ball-milled powders are presented in Figure 5.77 – Figure 5.80.

Spectra of O 1s and P 2p present single peaks at 531.1 and 133.3 eV, respectively. Ca energy region contain doublet of Ca $2p_{3/2}$ and Ca $2p_{1/2}$ at 347.3 and 350.8 eV. In case of C 1s energy region, spectra of initial powder is composed of two peaks at 285 and 289.2 eV corresponding to contamination carbon and CO_3 carbonate group.

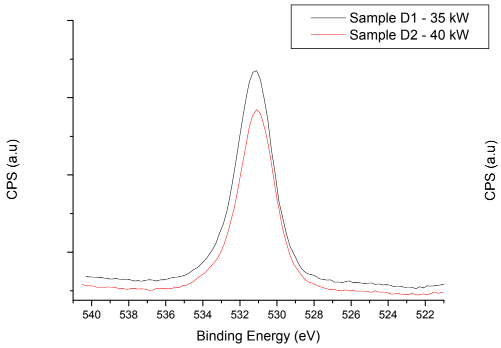

Figure 5.77 XPS spectra of O 1s energy region of samples D1 (top) and D2 (bottom)

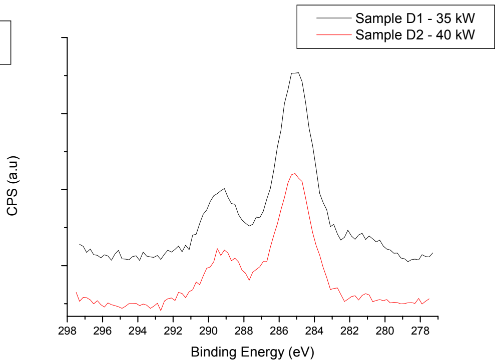

Figure 5.78 XPS spectra of C 1s energy region of samples D1 (top) and D2 (bottom)

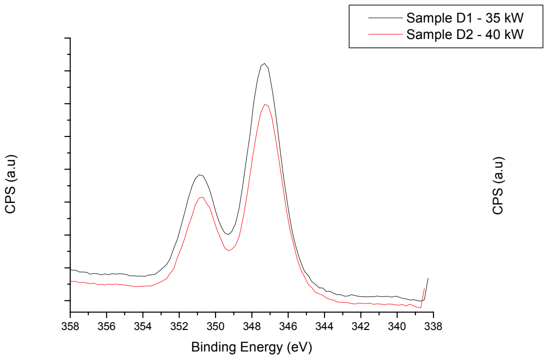

Figure 5.79 XPS spectrum of Ca 2p energy region of samples D1 (top) and D2 (bottom)

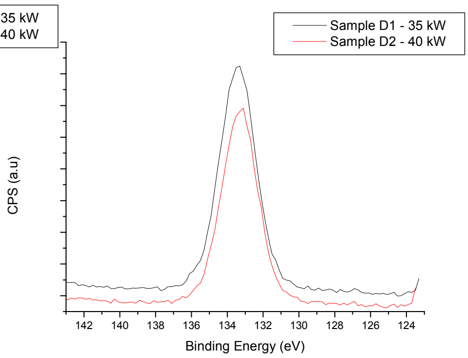

Figure 5.80 XPS spectrum of P 2p energy region of samples D1 (top) and D2 (bottom)

Quantitative analysis results are presented in Table 5.7. Analysis revealed considerable fraction of Na atoms, 2.1 % and 2.2 % for D1 and D2, respectively (possibly originated from surfactants used for preparation of suspension).

Table 5.7 XPS quantitative analysis results.

Sample	**Peak**	**%$_{atom}$**	**Ca/P ratio**
D1			
	O 1s	50.9	
	Ca 2p	19.7	1.33
	P 2p	14.8	
	C 1s	12.5	
	Na 2p	2.1	
D2			
	O 1s	52.9	
	Ca 2p	20.5	1.35
	P 2p	15.2	
	C 1s	9.2	
	Na 2p	2.2	

CHAPTER 6

FIELD EMISSION MEASUREMENTS

6.1. APS

Results of field emission of APS coatings are shown on Figure 6.1 - Figure 6.4. Figure 6.1 presents family of I = f(E) plots, after 3hours 10min and additional 1h conditioning procedures. One can observe that after first 3h10min. step the emission currents considerably increases reaching 45 µA, which is 100% greater value than before conditioning. Additional conditioning for 1h improved field emission current up to 85 µA for 150 V/µm of electric field.

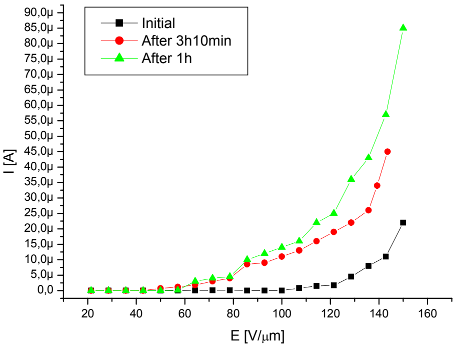

Figure 6.1 Electron emission plots I=f(E) of APS coatings

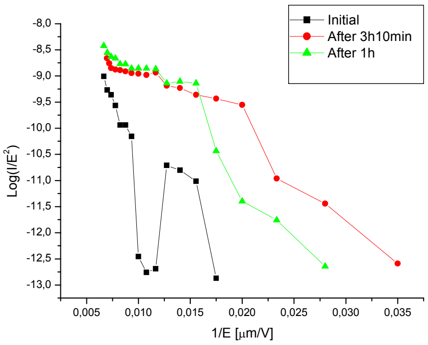

Figure 6.2 Fowler-Nordheim plots I=f(E) of APS coatings

Fowler-Nordheim plots presented in Figure 6.2, can by roughly fitted with straight lines, which suggests field induced mechanism of electron emission. Plot related with unconditioned sample (initial) appears to be considerably disturbed proving an unstable character of the emission. Onset value alteration of electron emission after conditioning is observed, being initially at level of about 57 V/µm it was decreased to 29 V/µm after first conditioning (3h10min), and surprisingly increased to 37 V/µm after second conditioning (1h).

Registered emission currents during first and second step of conditioning are presented in Figure 6.3 and Figure 6.4, respectively. First step is characterized by significant fluctuation of current within first 15 minutes, later the current is slowly rising to about 50 µA where occur sudden drop. The frequency of current drops seems to decrease, and finally resulting in stabilization of current at level of about 37µA. The second conditioning endured for 1 hour, in spite of being quite stable the current witnessed number of intense ripples.

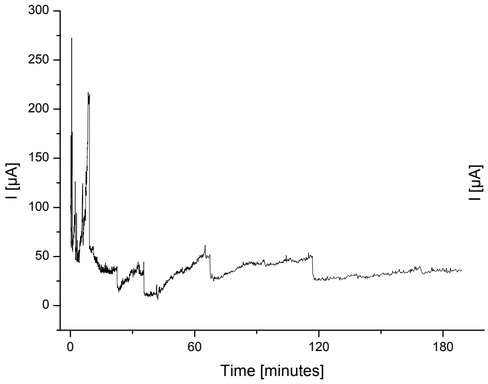

Figure 6.3 First step of conditioning of APS emitter

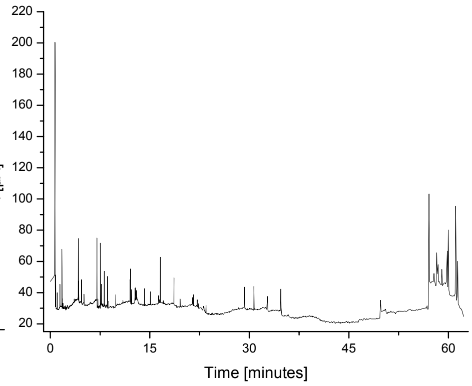

Figure 6.4 Second step of conditioning of APS emitter

6.2. SPS B

The field emission I = f(E) plots of SPS B coatings are shown in Figure 6.5. First (Figure 6.7) and second (Figure 6.8) conditioning led to improvement of emission current to 150 µA and 225 µA, respectively, moreover emission onset decreased from 62 V/µm to 50 and 35 V/µm, respectively (Figure 6.6). At 4th minute of third conditioning step, short-circuit occurred, after the incident emitter was able to still operate, though. Onset threshold was increased to 43 V/µm, however, maximum obtained current increased to about 400 µA.

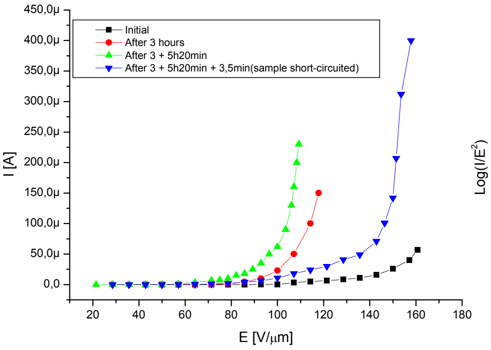

Figure 6.5 Electron emission plots I=f(E) of SPS B coatings

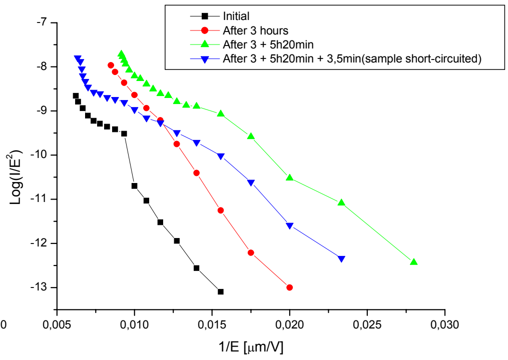

Figure 6.6 Fowler-Nordheim plots I=f(E) of SPS B coatings

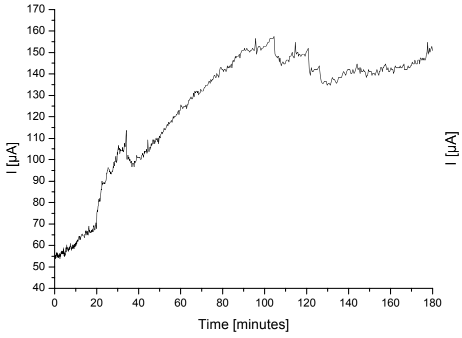

Figure 6.7 First step of conditioning of SPS B emitter

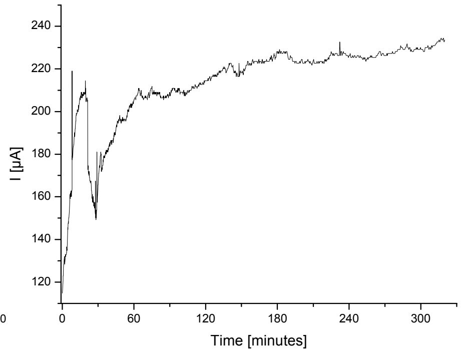

Figure 6.8 Second step of conditioning of SPS B emitter

6.3. SPS A

Field electron emissive characteristics (emission current versus electric field, I=f(E)) of the composite TiO_2 cathodes made with SPS A are presented in the Figure 6.9. The family of curves illustrates the electron emission behaviour of the emitters after the conditioning procedures (Figure 6.11 - Figure 6.13). First step of conditioning is presented in Figure 6.11, the cathode was driven to emit at current level of about 15 µA, in about 90 minutes the current increased to 50 µA. After sudden drop is observed down to 7 µA and again emitter activates to reach 30 µA. Third step of conditioning presented in Figure 6.13 shows rapid increase of current in first 10 minutes of operation. After 4 hours emission current stabilize to 230 µA. It's believed that during the conditioning process, the surface contaminations are reduced, especially those charged electrically. Moreover, formation of additional current paths in the coating could occur leading to improvement of emitter performance. Family of Fowler-Nordheim plots presents almost straight lines (Figure 6.10), which suggests only field emission mechanism to occur.

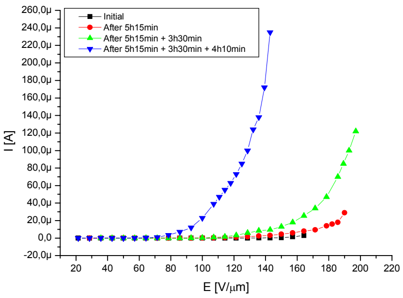

Figure 6.9 Electron emission plots I=f(E) of SPS A coatings

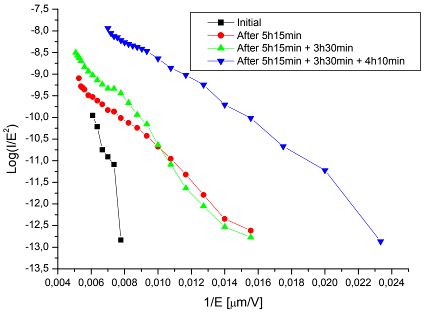

Figure 6.10 Fowler-Nordheim plots I=f(E) of SPS A coatings

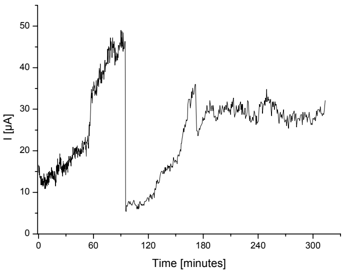

Figure 6.11 First step of conditioning of SPS A emitter

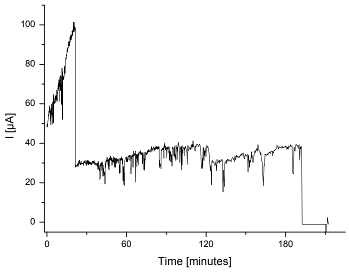

Figure 6.12 Second step of conditioning of SPS A emitter

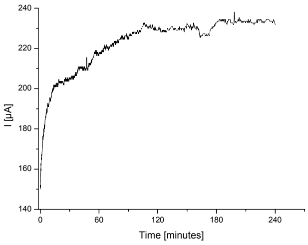

Figure 6.13 Third step of conditioning of SPS A emitter

6.4. GRAD

The GRAD coating after 4 successive conditioning steps (Figure 6.16 - Figure 6.19) emitted with maximum 100 µA current, which is 10 times higher in comparison with initial value (Figure 6.14). The initial FN plot (Figure 6.15 – black line) seems to compose of two slopes: at low emission current ($\log I/E^2 < -9{,}75$) and high emission currents ($\log I/E^2 > -9{,}75$), the latter could originate from weak performance of conducting channel in the thick GRAD coating, resulting in deficient of electrons at emitting surface, or/and high contamination of the surface. After conditioning the FN plots indicate single slope shape, which leads to conclusion, that conduction channel was developed during the conditioning or/and surface contaminants were desorbed.

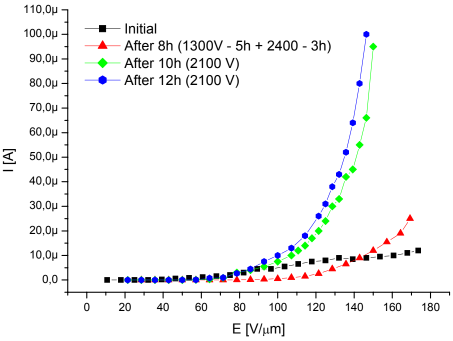

Figure 6.14 Electron emission plots I=f(E) of GRAD coating

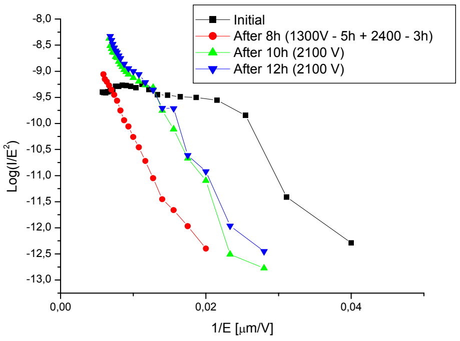

Figure 6.15 Fowler-Nordheim plots I=f(E) of GRAD coating

Registered emission current in function of time I = f(t) during the conditioning steps, differ from earlier presented. The Figure 6.16, Figure 6.18 and Figure 6.19 shows that emission current increases at the beginning of the conditioning, reaching the maximum it starts to decrease and finally stabilize at certain current level.

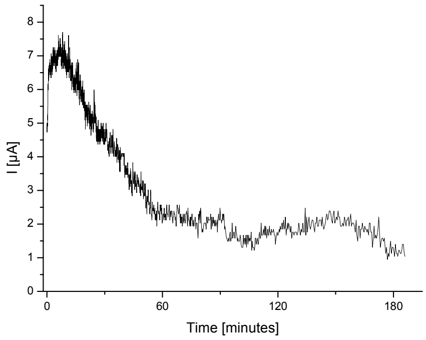

Figure 6.16 First step of conditioning of GRAD emitter

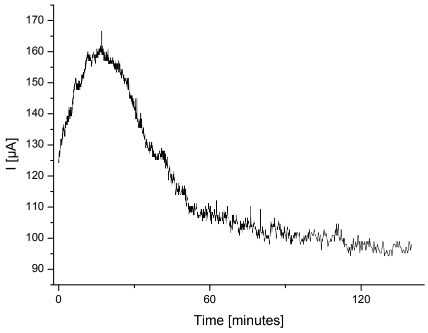

Figure 6.17 Second step of conditioning of GRAD emitter

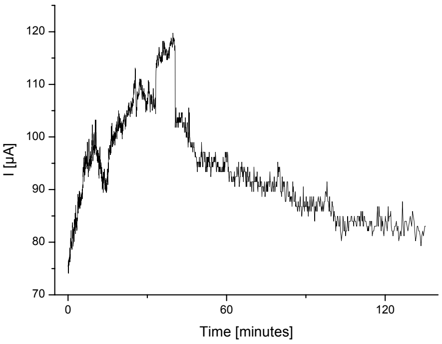

Figure 6.18 Third step of conditioning of GRAD emitter

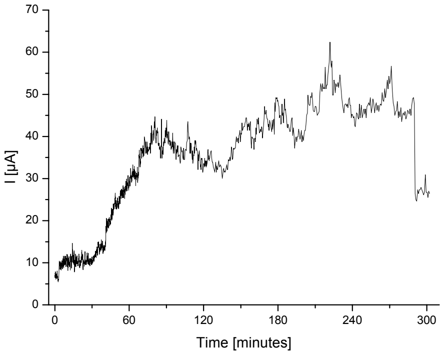

Figure 6.19 Fourth step of conditioning of GRAD emitter

CHAPTER 7

DISCUSSION

7.1. FIELD EMITTING COATINGS (TITANIA)

Suspension A

Suspension A was prepared from powder TiO_2, Huntsman commercially available pigment, of measured grain diameter D[3,2] = 0.33 µm. The powder contained only TiO_2 rutile phase. Suspension plasma spraying led to formation of round shape "pancake", fine-structured splats of a diameter up to 5 µm.

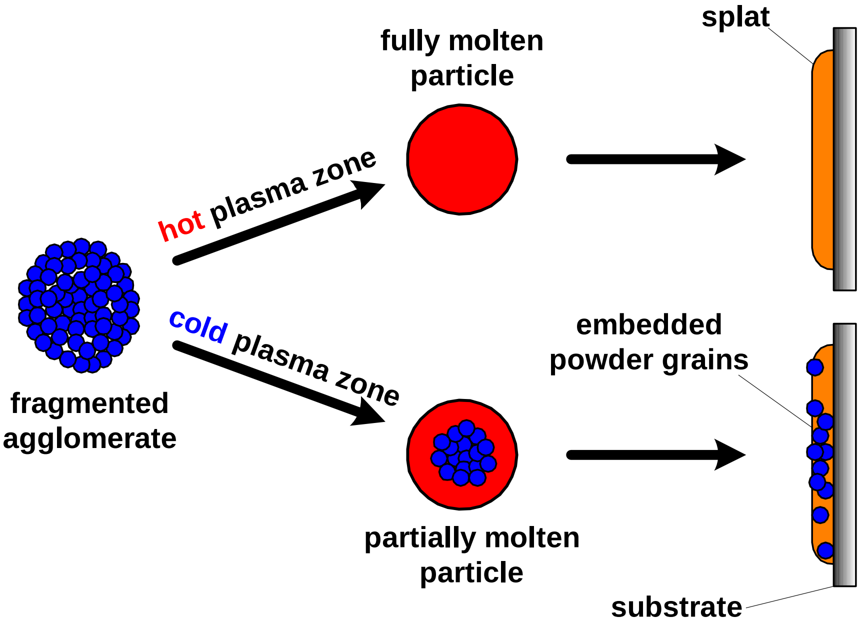

Figure 7.1 Mechanism of uniform splat originated from fully molten particle and substructured splat originated form partially molten particle

Some of solidified splats present substructure composed of initial Huntsman powder grains, which suggests incomplete melting of sprayed material in the plasma jet. The formation of such a splat could occur if suspension droplet pass through relatively colder plasma zone, where only external part of the agglomerate gets molten. Presence of partially or fully molten splats is expected since the atomizer injects the droplets with wide variety of trajectories into peripheral as well as core plasma zones. The droplets of the suspension which are injected into cold peripheral plasma zones have rather low probability to form a splat due to insufficient temperature to evaporate the solvent and to melt the solid agglomerate. In the case when the solvent is evaporated but a remained agglomerate is still unmolten the kinetic energy of the particle in the plasma spray process is too low to deform and interlock the solid agglomerate on the substrate. Therefore, those particles do not participate in a formation of the coating. In other words, only the partially and/or fully molten particles are able to bond to the substrate. Basing on the above considerations author of the thesis has proposed to update Fauchais model with additional formation mechanism of the substructured splat presented in Figure 7.1.

Transformed initial powder into coating is composed of mainly rutile and substantial fraction of anatase and non-stoichiometric Magneli phases Ti_xO_{2x-1} ($5 < x < 9$). The formation of the new phases predominate due to nucleation from the melt rather than transformation in the solid phase, since the initial powder contains thermodynamical stable rutile. Creation of defected phases with oxygen vacancy is probably promoted by rapid solidification of liquid material after contact with substrate and by reducing atmosphere of H_2 containing plasma gases.

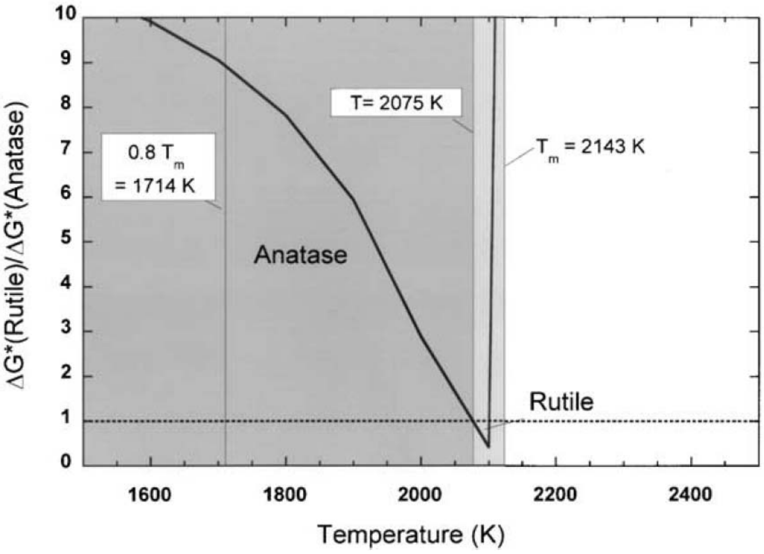

Figure 7.2 Ratio of critical energies for nucleation of anatase and rutile as a function of temperature [76].

In order to explain formation of metastable anatase, theory of homogenous nucleation was applied since the probability of foreign atoms being introduced into the small volume of the liquid droplets is very low. According to classic homogenous nucleation theory the nucleation rate of over-cooled liquid is related with critical nucleation energy. The precise evaluation of critical nucleation energies ratio for rutile and anatase in function of solidification temperature provided by Li and Ishigaki is presented in Figure 7.2. The characteristic shows that anatase should crystallize in the melt temperature under 2075 K and rutile in the temperature range from 2075 to 2147 K. In other words, anatase should form under rapid solidification and rutile under close to thermodynamical equilibrium cooling conditions. In case of big droplet deposition, phase nucleation is accompanied by liberation of considerable quantity of solidification heat, which reduces cooling rate and as a result promotes formation of rutile phase. The heat liberation in nucleating small droplet is rather insignificant, so anatase is promoted to form [75][76].

Finally, it could be stated that presence of the rutile in the coatings originate from:

- solid not transformed core of partially molten agglomerates;
- homogenous nucleation of the liquid under close to equilibrium cooling condition in the big droplets – liberation of solidification heat;
- heterogeneous nucleation of the liquid into rutile due to foreign atom contamination.

Coexistence of the three above-mentioned phenomena favour majority of the rutile in the coatings.

The coating suffered from internal stresses appeared by shift of diffraction pattern. Surface of the sample contained, besides of titanium atoms, aluminium atoms originated from inorganic envelope coating of initial powder, and impurities of sodium and silicon atoms of unknown origin. The possible origin for existence of sodium in suspension plasma sprayed coatings seems to be the sodium polyacrylate used for suspension stabilisation. On the other hand, the coatings sprayed with use of coarse powder APS, where the sodium polyacrylate was absent, also contain sodium contaminants. That suggests other unknown origin of contamination.

Suspension B

Size of 8 hours ball-milled M102 powder, used for formulation of suspension B, was D[3,2] = 0.45 µm. The powder contained mostly non-stoichiometric Magneli phases Ti_xO_{2x-1} ($5 < x < 9$) and considerable fraction of rutile TiO_2. After suspension plasma spraying, the resulting coating composed of rutile as a major phase, Magneli and anatase as the minor phases. The phase composition of the coating seems to be very similar to Suspension A coatings, which confirms hypothesis that main phase transformations occur during the liquid nucleation. In that case, the phase composition of the initial powder is less important if assumed that initial powder is completely molten, i.e. when a high electric power is applied during the spraying process.

The coating structure was found to contain stresses appeared by shift of diffraction pattern.

APS

Initial powder M102 without ball-milling had grain diameter D[3,2] = 23.34 µm. After conventional plasma spraying process, resulted coating contained predominant fraction of rutile and some of non-stoichiometric Magneli phases. It should be noted that absence of the anatase, in comparison with suspension plasma sprayed coatings, confirms strong relation of phase formation with initial material droplet size.

Coating seems to be highly textured, which manifests with absence/attenuation of main rutile peak at 2θ = 27.7°

GRAD

Two-layer coating, deposited suspension A on conventionally sprayed M102 TiO_2, exhibits microstructural features characteristic for earlier mentioned deposits. Top SPS A layer (TiO_2) and bottom layer (TiO_2) have the same thermal expansion coefficient, however the top coating suffers from stresses. Therefore, phenomenon suggests different stresses nature, probably quenching like.

Field electron emission of all measured samples was observed to be significantly influenced by the time of conditioning. Comparing emission properties of APS, SPS and GRAD coatings one can observe that SPS coating emits with highest intensity. Initially the emission current for this sample were at levels of about 25 µA and after the conditioning the current increased to 235 µA. Moreover the emission onset field was also improved from initial 130 V/µm to 42 V/µm. The shape of FN plots confirms field induced character of emission. Nonlinearity of the plot in the initial emission stage of APS coating are due to instability of emission most probably caused by contamination of the surface. Nonlinearity at high current intensities is ascribed to shielding effect of emitted electrons cloud. Initial FN plot of gradient emitter is thought to be disturbed by inefficient electron transport from the bulk to the surface or/and its contamination.

The phenomenon of field emission parameter improvement is most probably related with decontamination of the emitting surface during operation, and development of conducting channels in the coating.

7.2. BIOCOMPATIBLE COATINGS (HYDROXYAPATITE / TITANIA)

Feedstock

HAp suspension was prepared with use of 8 hours ball-milled Tomita powder. Initial grain size D[3,2] was 44.09 µm and during ball-milling was decreased to 1.47 µm. Powder contained exclusively HAp crystal phase and remained unchanged after ball-milling. However, carbon contamination couldn't be avoided due to application of ethanol as cooling medium for attrition.

Sample A1 and A2
35 and 40 kW plasma spraying of HAp suspension onto clean and rough Ti substrates produced 10 to 20 µm thick and considerably porous coatings. Sample A1 being sprayed with 35 kW looks to be poorly attached to substrate, manifested by voids within substrate-coating interface. Poor adhesion is probably caused by insufficient arc power, unable to evaporate and melt powder particles. On the contrary is in the case of the sample A2. Application of 40kW of torch power induces faster evaporation of solvent from suspension and melting of powder particles. As a result, more particles are molten, got splattered and interlocked within roughness of the surface, effectively more splats build up the coating. This hypothesis is confirmed by the fact that sample A2 is observable thicker than A1.

The phase composition of the coatings is dominated by HAp crystal phase. Both samples also contain α-TCP, β-TCP, TTCP decomposition phases. Moreover, X-ray diagrams were featured by peaks related to susbstrate material – titanium. Those reflexes are less significant for A2 sample, which proves the greater thickness and/or density of sample A2.

Sample B1 and B2
Samples B1 and B2 are characterized by double layer structure. The APS bottom layer is 100 µm thick, dense, crack structured coating – characteristic for APS sprayed HAp [77]. The top layer – HAp suspension plasma sprayed – is similar to samples A1 and A2. As it was observed earlier, coating obtained with power of 40 kW (B2) indicates better adhesion to bottom layer. Additionally, higher content of α-TCP, β-TCP, TTCP decomposition phases were observed. Greater decomposition is promoted by higher torch power during the spraying.

Samples C1 and C2
Samples C1 and C2 were manufactured in two step SPS spraying in order to obtain double layered structure – SPS HAp on SPS TiO_2. However, interface between top and bottom layer is indistinguishable with standard topographic contrast observation. Application of material contrast observation allowed to distinguish blurred interface.

Bottom TiO_2 layer contain rutile and anatase phase. Formation of metastable anatase phase was observed by author in previous study **[78]**. The top layer is constituted of HAp and α-TCP, β-TCP, TTCP decomposition phases.

Samples D1 and D2
Samples D1 and D2 were produced with gradient profile suspension feeding. The coatings are 30-40 µm thick and porous. Material contrast reveals its gradient structure: content of Ca and P atoms is low at substrate-coating interface and increases towards the surface. The reverse effect is observed under Ti material contrast – high content of Ti atoms at the substrate-coating interface and decrease of the Ti content towards the surface. The observed distribution of the elements could have been disturbed by a sample metallographic preparation and/or eventually due to atom diffusion in the high temperatures of the deposition process. Therefore, obtained information should be considered as a coarse verification of coating gradient structure.

Coatings contain HAp crystal phase and its decomposition products such as α-TCP, β-TCP, TTCP, CaO, and finally rutile phase. D2 sample seems to be more decompose due to higher arc power than sample D1.

CHAPTER 8

CONCLUSIONS

8.1. TECHNOLOGY OF SUSPENSION PRECURSOR PLASMA SPRAYING

The technology of plasma spraying was adapted to spray nano-structured/submicrometer feedstock. The effort was undertaken to formulate the suspension containing finely milled grains of titania or hydroxyapatite using appropriate proportion of surfactant and of solid phase fraction. The feedstock was delivered to plasma jet using two setups realized in this work:

- pressurized vessel feeder;
- electronically regulated device with two peristaltic pumps (SPSfeed).

The feedstock injection into the plasma jet was realized through an commercial atomizer. The injection was characterized by wide range of the suspension droplets trajectories and momenta, which led to formation of different types of splats (partially or fully molten) or unmolten agglomerates. The variety of material droplet history in the plasma is thought to be a cause of multiphase composite structure of the coatings.

The spray parameters were optimized to obtain relatively thin (5-20 µm) continuous coatings. In particular, it was found out that electric power input to plasma should be readily greater at suspension plasma spraying than in powder plasma spraying. This can be explained by evaporation of distilled water which needs additional thermal energy.

The future works should be concentrated into:

- application of different atomizers: radial narrow angled injection or especially promising axial injection, both approaches would considerably improve efficiency of the process;
- application of statistical method of spray parameters optimization ;
- testing of organic liquid based suspension which consummates less thermal energy to evaporate;
- development of precursor solutions that do not include a solid phase (in this case a high temperature driven reaction would lead to formation of solid phase).

8.2. FIELD EMITTING COATINGS (TITANIA)

Comparison of materials used for formulation of Suspension A (Huntsman powder) and Suspension B (ball-milled for 8 hours Metco 102 powder) shows significant differences, especially phase composition. Surprisingly, after suspension plasma spraying, coatings deposited using both suspensions, present very similar properties: morphology, size of the splats as well as crystal phase composition. The feature distinguishing both coatings could be found only on level of surface chemistry, observed with use of XPS. Coating obtained from Suspension A contains considerable quantity of Al atoms, originated from Al_2O_3 envelope coating of initial powder, unlike coatings sprayed with Suspension B, where Al atoms were absent.

Comparison of microstructural properties of TiO_2 coatings deposited with conventional APS and SPS techniques brings out unique features of SPS sprayed coatings:

- reduced geometrical size of splats ;
- lower minimum thickness of the continous coating;
- well developed surface ;
- formation of metastable anatase phase;
- absence of texture.

Due to above mentioned unique features of the SPS sprayed coatings, the technology seems to be very promising for many applications, for example field electron emitters.

As it was observed, the suspension plasma sprayed coatings present superior field electron emission properties than conventionally sprayed ones. The emitter performance was observed to be strongly influenced by conditioning time leading to improvement of current intensity up to 400µA and onset of the emission down to 42 V/µm. The obtained parameters are thought to be sufficient for implementation of the SPS coatings as the cold cathodes in the electronic devices. However, before final application of the SPS coatings, the additional investigations should be carried out focusing on:

- realization of big surface area SPS field emitter and testing its emission stability in different locations on the surface,
- realization of a electronic device with large surface area suspension plasma sprayed TiO_2 acting as a cold cathode,
- testing of a above-mentioned device behaviour in different conditions (ageing, humidity, temperature) in order to find out whether its stability is satisfactory.

8.3. BIOCOMPATIBLE COATINGS (HYDROXYAPATITE / TITANIA)

Suspension plasma spraying process is the successful method for deposition of duplex coatings as well as gradient coatings of TiO_2/HAp composites. The application of TiO_2 bond coat, considerably improves interface quality. The observed improvement was more significant for coatings sprayed with torch power of 40 kW. Unfortunately, the higher power, the more intense decomposition of a hydroxyapatite to less biocompatible phases, i.e. α-TCP, β-TCP, TTCP or not tolerated CaO.

The accurate evaluation of the materials distribution in the gradient coatings was limited due to distortion of the distribution by metallographic preparation of the samples or eventually thermal diffusion of the atoms.

Further works should be focussed on the following points:

- investigation of the adhesion and cohesion of duplex and gradient coatings;
- optimisation of spray parameters in order to obtain desired microstructural (phase composition and porosity) and mechanical properties (adhesion)
- investigation of electrical properties and its impact on biocompatibility of HAp coatings;
- testing of corrosion properties of suspension sprayed coating in body simulating fluids;
- development of new types of suspension basing onto metalorganic liquids which would decompose in plasma by giving desired hydroxyapatite phase.

REFERENCES

[1] Pawlowski L. *The Science and Engineering of Thermal Spray Coatings*, Wiley, Chichester, (1995).

[2] Schoop M. U., Guenther W.H., Das Schoopsche Metallspritzverfahren, Franckh Verlag, Stuttgart, Germany, (1917).

[3] Giannini G., Ducatti A., Plasma stream apparatus and methods, US Patent, no. 2 922 869.

[4] Gage R.M., Nestor D.M., Yenni Y.M., Collimated electric are powder deposition process, US Patent, no. 3 016 447.

[5] Fauchais P., Montavon G., Vardelle M., Cedelle J., Recent developement in direct current plasma spraying. In : 2nd International Meeting on Thermal Spraying, Lille, France

[6] Tomaszek R., Znamirowski Z., Brylak M., Pawłowski L., Sokołowski A., Comparative study of the TiO2 deposits obtained by plasma spraying of powder and suspension, materiały konferencyjne Tagungsband 6. Industriefachtagung "Oberflachen- und Warmebehandlungstechnik" und zum 8. Werkstofftechnischen Kolloquium ISBN 3-00-016841-9

[7] Tomaszek R., Znamirowski Z., Pawlowski L. and Wojnakowski A., Temperature behaviour of titania field emitters realized by suspension plasma spraying, Surface & Coatings Technology 201 (2006) 2099-2102

[8] Tomaszek R., Znamirowski Z., Pawlowski L., Zdanowski J., Effect of conditioning on field electron emission of suspension plasma sprayed TiO2 coatings, Ion 2006: VI-th International Conference, 26 – 29.06.2006, Kazimierz Dolny, Poland

[9] Ban Z.-G., Shaw L. L., Characterization of Thermal Sprayed Nanostructured WC-Co Coatings Derived From Nanocrystralline WC-18wt%Co Powders, Journal of Thermal Spray Technology 12 (1) (2003) 112 – 119

[10] Dahotre N.B., Nayak S., Nanocoatings for engine application, Surf. Coat. Technol. 194 [1] (2005) 58-59.

[11] Yang, G.-J., Li, C.-J., Han, F., Mao, S.-F., Preparation of TiO2 Photocatalyst by Thermal Spraying with Liquid Feedstock, Thermal Spray 2003: Advancing the Science & Applying the Technology, Moreau, C.,Marple, B., (ed.), ASM International, ISBN: 0-87170-785-3, pp. 675 – 680.

[12] Monterrubio-Badillo C., Ageorges H., Chartier T., Coudert J. F., Fauchais P., Plasma Spraying of a Perovskite Suspension for SOFC Cathodes, Thermal Spray 2003: Advancing the Science & Applying the Technology, Moreau, C., Marple, B. (ed.), ASM International, ISBN: 0-87170-785-3, pp. 687 – 692.

[13] Delbos C., Fazilleau J., Coudert J.F., Fauchais P., Bianchi L., Wittmann-Teneze K., Plasma spray elaboration of finely structured YSZ thin coating by liquid suspension injection, Proceedings of the International Thermal Spray Conference, ITSC2003, Orlando (USA), 5-8 May 2003, Thermal Spray 2003 : Advancing the Science and Applying the Technology, Marple B.R., Moreau C. Eds., ASM International, Materials Park, OH (USA), 2003, 661-669

[14] Shaw L. L., Goberman D., Ren R., Gell M., Jiang S., Wang Y., Xiao T. D. and Strutt P. R., The dependency of microstructure and properties of nanostructured coatings on plasma spray conditions, Surface and Coatings Technology 130 (1) (2000) 1-8.

[15] Lima R. S., Kucuk A.and Berndt C. C., Evaluation of microhardness and elastic modulus of thermally sprayed nanostructured zirconia coatings, Surface and Coatings Technology 135 (2-3) (2001) 166-172.

[16] He J. and Schoenung J. M., A review on nanostructured WC–Co coatings, Surface and Coatings Technology 157 (1) (2002) 72-79.

[17] Klimpel A. *Napawanie i natryskiwanie cieplne*, WNT, Warszawa, (2000).

[18] Pawlowski L. *Podstawy procesu natryskiwania plazmowego i przykłady jego zastosowań w technologii elektronowej*, Wydawnictwo Politechniki Wrocławskiej, Wrocław, (1977).

[19] Pawlowski L. *Dépots physiques*, Press polytechniques et universitaires romandes, Lausanne, (2003).

[20] Ozturk A., Cetegen B. M., Modeling of axially and transversely injected precursor droplets into a plasma environment, International Journal of Heat and Mass Transfer 48 (2005) 4367–4383.

[21] Ozturk A., Cetegen B. M., Modeling of plasma assisted formation of precipitates in zirconium containing liquid precursor droplets, Materials Science and Engineering A 384 (2004) 331–351

[22] Blazdell P., Kuroda S., Plasma spraying of submicron ceramic suspensions using a continuous ink jet printer, Surface and Coatings Technology 123 (2000) 239–246.

[23] Oberste-Berghouse J., Bouaricha S., Legoux J.-G., Moreau C., Production of SDC plasma sprayed nanocoatings using an internal injection of a suspension containing nanoparticles, Proceedings of International Thermal Spray Conference 2005, CD-Rom, ISBN 3-87155-793-5, Ed. E.F. Lugscheider, Pub. DVS Verlag GmbH, Düsseldorf, Germany, (2005).

[24] Wittmann K., Blein F., Fazilleau J., Coudert J.F., Fauchais P., A new process to deposit thin coatings by injecting nanoparticles suspensions in a DC plasma jet enhanced chemical vapour deposition, International Thermal Spray Conference, Essen (Germany), 4-6 March 2002, Tagungsband Conference

Proceedings, Lugscheider E. Ed., ASM Pub., DVS, Deutscher Verband für Schweißen, Germany, 2002, 519-522

[25] Fazilleau J., Delbos C., Violier M., Coudert J.F., Fauchais P., Bianchi L., Wittmann-Teneze K., Influence of substrate temperature on formation of micrometric splats obtained by plasma spraying liquid suspension, Proceedings of the International Thermal Spray Conference, ITSC2003, Orlando (USA), 5-8 May 2003, Thermal Spray 2003 : Advancing the Science and Applying the Technology, B.R. Marple, C. Moreau Eds., ASM International, Materials Park, OH (USA), 2003, 889-893

[26] Fazilleau J., Delbos, Rat V., Coudert J.F., Fauchais P., B. Pateyron, Understanding zirconia suspesnion plasma spraying through simple models, Part 1: suspension injection and behavior, Plasma Chem. Plasma Proc., accepted for publication.

[27] Fauchais P., Rat V., Delbos C., Coudert J.F., Chartier T., Bianchi L., Understanding of suspension DC plasma spraying of finely structured coatings for SOFC, IEEE Trans. On Plasma Science, 33 [2] (2005) 920.

[28] Gell M., Xie L., Jordan E. H., Padture N. P., Mechanisms of spallation of solution precursor plasma spray thermal barrier coatings, Surface & Coatings Technology 188–189 (2004) 101– 106

[29] Jadhav A., Padture N. P., Wu F., Jordan E. H., Gell M. Thick ceramic thermal barrier coatings with high durability deposited using solution-precursor plasma spray, Materials Science and Engineering A 405 (2005) 313–320

[30] Jordan E.H., Xie L., Ma X., Gell M., Padture N., Cetegen B., Roth J., Xiao T. D. and Bryant P.E.C., Superior Thermal Barrier Coatings Using Solution Precursor Plasma Spray, J. Thermal Spray 13 (2004) 57-65.

[31] Xie L., Ma X., Jordan E. H., Padture N. P., Xiao D.T., Gell M., Deposition mechanisms of thermal barrier coatings in the solution precursor plasma spray process, Surface and Coatings Technology 177 –178 (2004) 103–107

[32] Xie L., Ma X., Jordan E. H., Padture N. P., Xiao D.T., Gell M., Identification of coating deposition mechanisms in the solution-precursor plasma-spray process using model spray experiments, Materials Science and Engineering A362 (2003) 204–212

[33] Xie L., Ma X., Ozturk A., Jordan E. H., Padture N. P., Cetegen B. M., Xiao D. T., Gell M., Processing parameter effects on solution precursor plasma spray processspray patterns, Surface and Coatings Technology 183 (2004) 51–61

[34] Guo X.Z., Ravi B.G., Devi P.S., Hanson J.C., Margolies J., Gambino R.J., Parise J.B., Sampath S., Synthesis of yttrium iron garnet (YIG) by citrate–nitrate gel combustion and precursor plasma spray processes, Journal of Magnetism and Magnetic Materials 295 (2005) 145–154

[35] Guo X.Z, Ravi B.G., Yan Q.Y., Gambino R.J., Sampath S., Margolies J., Parise J.B., Phase and microstructure evolution in precursor plasma-sprayed YIG coatings, Ceramics International 32 (2006) 61–66

[36] Hurevich V., Smurov I., Pawłowski L., Theoretical study of the powder behavior of porous particles in a flame during plasma spraying, Surface and Coatings Technology 151-152 (2002) 370-376.

[37] Normand B., Fervel V., Codder C., Nikitine V., Tribological properties of plasma sprayed alumina-titania coatings: role and control of the microstructure, Surface and Coatings Technology 123 (2000), 278-287.

[38] Graßmann O., Heimann R.B., Compositional and microstructural changes of engineered plasma-sprayed hydroxyapatite coatings on Ti6Al4V substrates during incubation in protein-free simulated body fluid, J. Biomed.Mater.Res. 53(6) (2000) 685-693.

[39] Carayon M.T., Lacout J.L., Study of the Ca/P atomic ratio of the amorphous phase in plasma-sprayed hydroxyapatite coatings ,J.Solid State Chem. 172 (2003) 339-350.

[40] McPherson R., Formation of metastable phases in flame and plasma prepared alumina, Journal of Material Science, 8, (1973), 852-858.

[41] Götze J., Heimann R.B., Hildebrandt H., Gburek U., Microstructural investigations into calcium phosphate biomaterials by spatially resolved cathodoluminescence, 2nd Interdisc. Essen-Symposium 'Biomaterials: Fundamentals and Clinical Applications'. Mat.-wiss. u. Werkstofftechn. 32(2001) 130-136

[42] Krishnan R., Dash S., Babu Rao C., Subba Rao R.V., Tyagi A.K., Raj B., Laser induced structural and microstructural transformations of plasma sprayed Al_2O_3 coatings, Scripta Materialia 45 (2001) 693-700.

[43] **Tomaszek R.**, Pawlowski L., Zdanowski J., Grimblot J., Laureyns J., Microstructural transformations of TiO_2, Al_2O_3+13TiO_2 and Al_2O_3+40TiO_2 at plasma spraying and laser engraving Surface & Coatings Technology 185 (2004) 137– 149

[44] Heberlein J., Sensing and control of plasma torch instabilities in Sensors and Control 2004, Pub. ASM International, Materials Park, OH, USA, 2004, eproceedings.

[45] Kudinov V. V., Pekshev P. Y. and Safiullin V. A., Forming of the Structure of Plasma Sprayed Materials, High Temp. Dust. Laden Jets, (éd.) Solonenko et Fedorchenko, (1989) 381-418.

[46] Fukumoto M. and Huang Y., Flattening Mechanism in Thermal Sprayed Nickel Particle Impinging on Flat Substrate Surface, J. Thermal Spray Technol., 8(3), p. 427-432, 1999.

[47] Tanaka Y., Fukumoto M., Investigation of dominating factors on flattening behaviour of plasma sprayed ceramic particles, Surface and Coatings Technology 120–121 (1999) 124–130

[48] Charbonnier F., Developing and using the field emitter as a high intensity electron source, Applied Surface Science 94/95 (1996) 26 – 43.

[49] Spindt C. A., A thin film field emission cathode, J. Appl. Phys. 39, (1968), 3504 – 3505

[50] Czarczyński W., Mikroelektronika próżniowa, Oficyna Wydawnicza Politechniki Wrocławskiej, Wrocław (2000).

[51] Znamirowski Z., Czarczynski W., Pawlowski L., Electronic Emission from Surface of Plasma Sprayed and Laser Engraved TiO2 and Al2O3/TiO2 Alloys, FraPol04, Bourges (France), 17 June 2003.

[52] Znamirowski Z., Czarczynski W., Le Maguer A., Pawlowski L., Plasma sprayed and laser engraved field electron emitters, Surface and Coatings Technology 165 (2003) 211–215.

[53] Znamirowski Z., Czarczynski W., Pawlowski L., Le Maguer A., Field electron emission from laser the engraved surface, Vacuum 70 (2003) 397–402

[54] **Tomaszek R.**, Znamirowski Z., Pawlowski L., Grimblot J., Zdanowski J., Czarczynski W., Plasma sprayed ceramics for low macroscopic field emitters, High Temperature Material Processes, 9(2005) 103-108

[55] Znamirowski Z., Czarczynski W., Campana F., Janssen J.-P., Rivenet M., Pawlowski L., in: Moreau C., Marple B. (Eds.), Thermal Spray 2003: Advancing the Science and Applying the Technology, ASM Int, Materials Park, Ohio, USA, 2003, pp. 1069– 1073.

[56] Znamirowski Z., Pawlowski L., Cichy T., Czarczynski W., Low macroscopic field electron emission from surface of plasma sprayed and laser engraved TiO2, Al2O3+13TiO2 and Al2O3+40TiO2 coatings, Surface & Coatings Technology 187 (2004) 37– 46

[57] Forbes R. G., Low-macroscopic-field electron emission from carbon films and other electrically nanostructured heterogeneous materials: hypotheses about emission mechanism, Solid-State Electronics 45 (2001) 779-808.

[58] Forbes R. G., Field-induced electron emission from electrically nanostructured heterogeneous (ENH) materials, Ultramicroscopy 89 (2001) 7–15.

[59] Forbes R. G., Edgcombe C. J., Valdrè U., Some comments on models for field enhancement, Ultramicroscopy 95 (2003) 57–65.

[60] Rohrbach F., CERN Report 71-5/TC-L, 1971.

[61] www.huntsman.com, Tioxide R-TC90 Product Brochure.

[62] www.sulzermetco.com, Metco 102 Titanium Oxide Product Info.

[63] Masters K., *Spray Drying Handbook*, 4th ed., George Godwin, London, England, (1985), p. 67.

[64] Lima R.S., Marple B.R., From APS to HVOF spraying of conventional and nanostructured titania feedstock powders: a study on the enhancement of the mechanical properties, Surface & Coatings Technology 200 (2006) 3428-3437

[65] Toussaint D. R., Laude L. D., Geskin V. M., Lazzaroni R., Gouttebaron R., Micro-Raman spectroscopy study of surface transformations induced by excimer laser irradiation of TiO_2, Thin Solid Films 440 (2003) 268–277

[66] Oh S.-M., Ishigaki T., Preparation of pure rutile and anatase TiO2 nanopowders using RF thermal plasma Thin Solid Films 457 (2004) 186–191.

[67] Bertóti I., Mohai M., Sullivan J.L., Saied S.O., Surface characterisation of plasma-nitrided titanium: an XPS study, Applied Surface Science 84 (1995) 357-371

[68] Pouilleau J., Devilliers D., Garrido F., Durand-Vidal S., Mahé E., Structure and composition of passive titanium oxide films, Materials Science and Engineering B 47 (1997) 235-243

[69] Sul Y.-T., Johansson C.B., Petronis S., Krozer A., Jeong Y., Wennerberg A., Albrektsson T., Characteristics of the surface oxides on turned and electrochemically oxidized pure titanium implants up to dielectric breakdown: : the oxide thickness, micropore configurations, surface roughness, crystal structure and chemical composition, Biomaterials 23 (2002) 491-501

[70] Cusco R., Guitian F., de Aza S., Artus L., Differentiation between Hydroxyapatite and β-Tricalcium Phosphate by Means of μ-Raman Spectroscopy, Journal of the European Ceramic Society 18 (1998) 1301-1305.

[71] Darimont G.L., Gilbert B., Cloots R., Non-destructive evaluation of crystallinity and chemical composition by Raman spectroscopy in hydroxyapatite-coated implants, Materials Letters 58 (2003) 71– 73

[72] Li H., Ng B.S., Khor K.A., Cheang P., Clyne T.W., Raman spectroscopy determination of phases within thermal sprayed hydroxyapatite splats and subsequent in vitro dissolution examination, Acta Materialia 52 (2004) 445–453.

[73] Gu Y.W., Tay B.Y., Lim C.S., Yong M.S., Biomimetic deposition of apatite coating on surface-modified NiTi alloy, Biomaterials, 26 (2005), 6916–6923.

[74] Kaciulis S., Mattogno G., Pandolfi L., Cavalli M., Gnappi G., Montenero A., XPS study of apatite-based coatings prepared by sol–gel technique, Applied Surface Science 151 (1999) 1–5.

[75] Li Y., Ishigaki T., Synthesis of crystalline micron spheres of titanium dioxide by thermal plasma oxidation of titanium carbide, Chemistry of Materials, 13[5] (2001) 1577-1584.

[76] Li Y., Ishigaki T., Thermodynamic analysis of nucleation of anatase and rutile from TiO_2 melt, Journal of Crystal Growth 242 (2002) 511-516.

[77] Heimann R.B., Vu T. A., Wayman M. L., Bioceramic coatings: state-of-the-art and recent development trends, Eur. J. Mineral 9 (1997) 597-615.

[78] Tomaszek R., Pawlowski L., Gengembre L., Laureyns J., Znamirowski Z., Zdanowski J., Microstructural characterization of plasma sprayed TiO2 functional coating with gradient of crystal grain size, Surface & Coatings Technology 201 (2006) 45-56.

APPENDIX

SPSFEED – SUSPENSION FEEDING SYSTEM

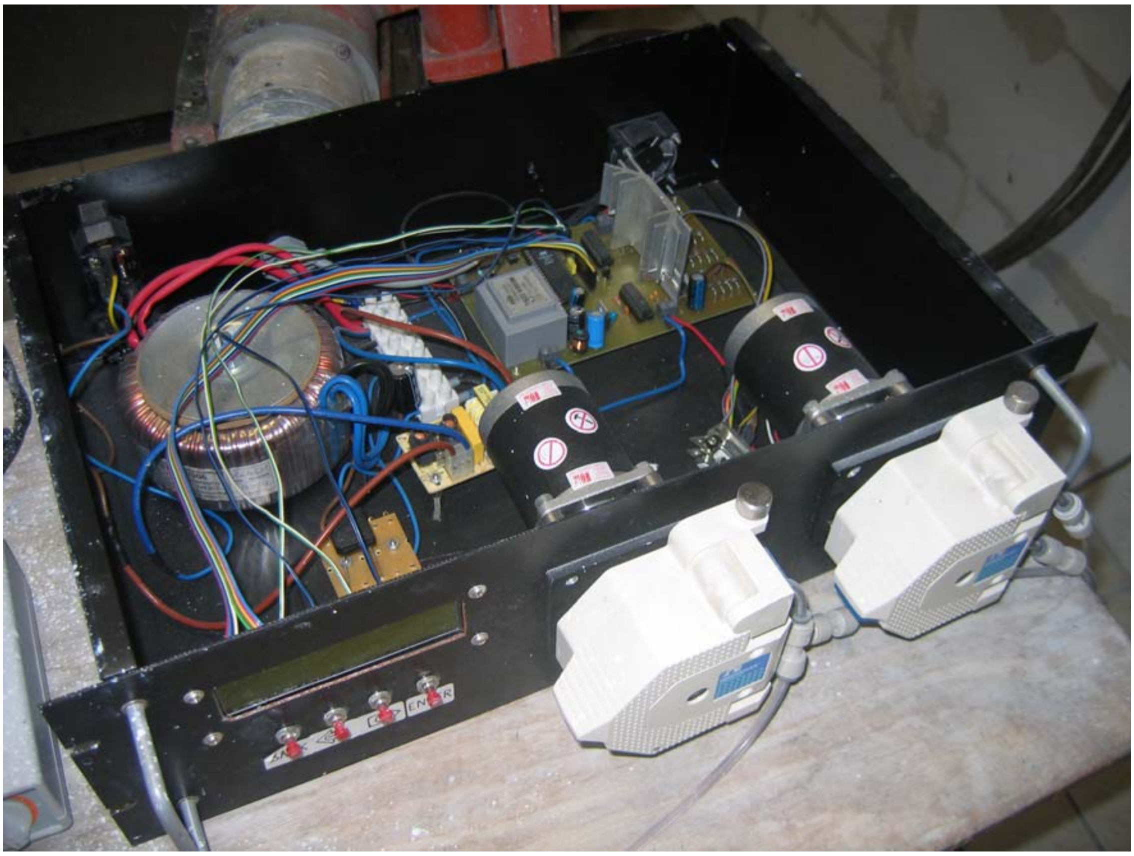

Figure A.1 SPSfeed suspension feeding system

Designed and produced SPSfeed system, presented in figure A.1, is capable to fulfil requirements for suspension plasma spraying with simultaneous feeding of two feedstocks.
Precise regulation and repeatability is provided by microcontroller driven peristaltic pumps.
ATMEL ATmega16 microcontroller, the heart of the system (Figure A.2) performs following operations:

- can programmed from PC directly to its Flash memory with use of ISP interface, making it easy to update software without disassembling the device;
- can be triggered to initiate a suspension feeding by external signal (ABB robot) or manually;
- supports user interface consisting of LCD display and buttons;
- controls rotation speed of the WObit 57BYG707 stepper motors, which turn the peristaltic pumps;

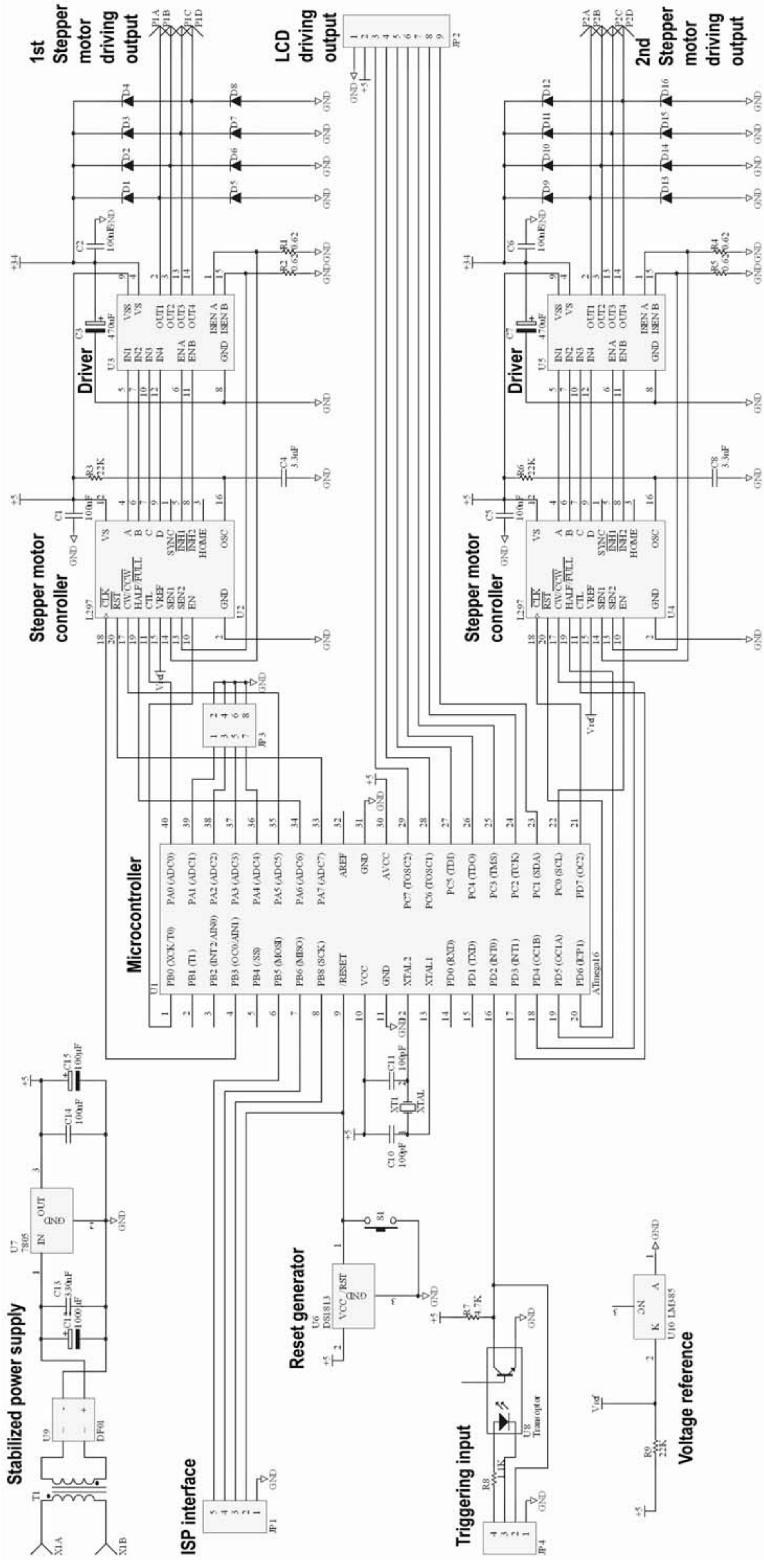

Figure A.2 Schematics of SPSfeed mainboard

The layout of SPSfeed mainboard is presented in Figure A.3

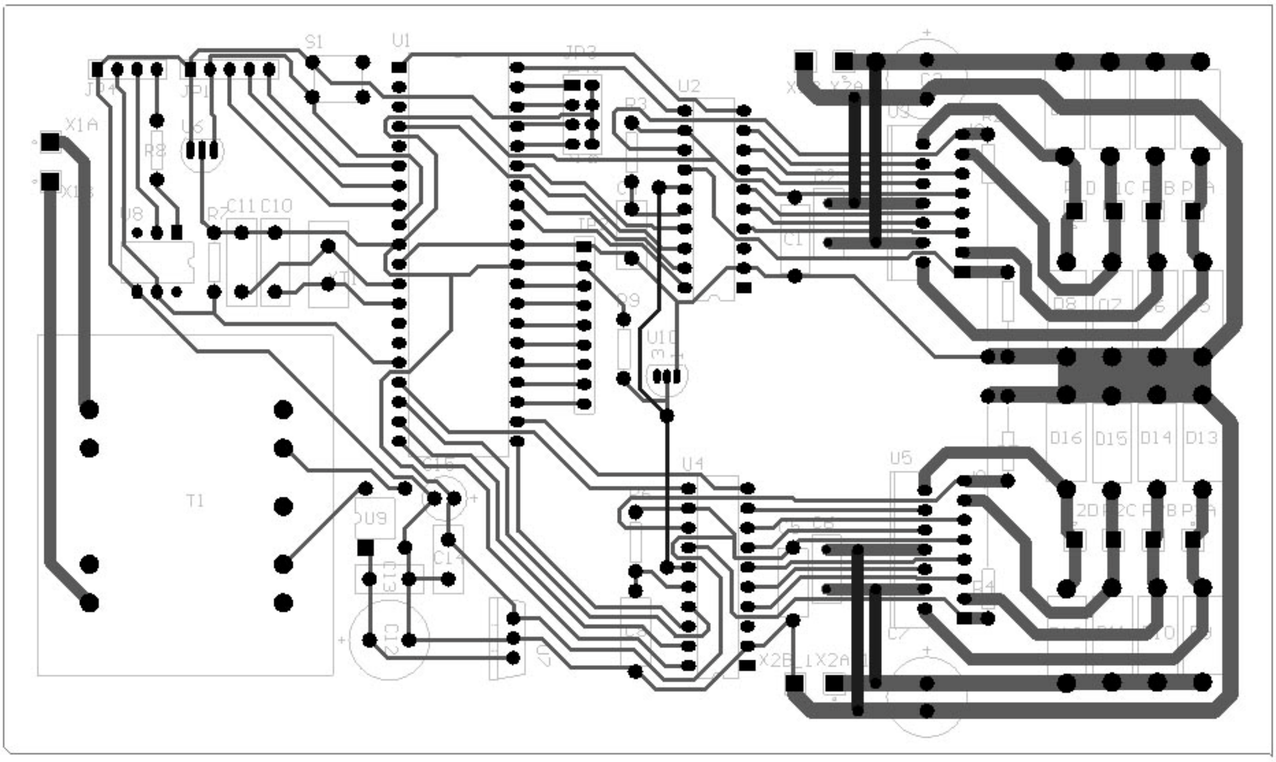

Figure A.3 PCB print of mainboard

Above-mentioned functions are supported by the software created by the author of this thesis.

```
Software of SPSfeed system for ATmega16 μ-controller

#include "c:\include\avr\io.h"
#include "c:\include\avr\pgmspace.h"
#include "c:\include\avr\signal.h"
#include "c:\include\avr\interrupt.h"

#define lcd_rs 1                          //defines bit of line RS for LCD
#define lcd_rw 2                          //defines bit of line R/W for LCD
#define lcd_en 3                          //defines bit of line EN for LCD

#define back 2
#define left 4
#define right 8
#define enter 16

#define CR 0x7c

#define cbi(port, bit) port &= ~(1 << bit)
#define sbi(port, bit) port |= (1 << bit)

unsigned char line=0;
unsigned char column=0;
int table[2][3];                          //holds flow rates: start, step,
number
unsigned int ver1,ver2;                   //menu selection triggers
unsigned int mode;                              //automatic or manual
double calib = 1;
```

```
int param;                              //parameter
int interrupt=0;                        //used for counting the interrupts
int sign;                               //sign of step value

void waitms (int ms)                    //delay function
{
#define tau 10.38
int cv;
 int cv1;
 for(;ms>0;ms--)
  for(cv=1;cv>0;cv--)
   for(cv1=10;cv1>0;cv1--)
    asm("nop");
}

//*************************** LCD ***************************************

void write_to_lcd(char data)            //writes instruction/data to LCD
{
 cbi(PORTC,lcd_rw);
 sbi(PORTC,lcd_en);
 PORTC=(PORTC&0x0f)|(data&0xf0);              //prepares older half-byte for
LCD
 asm("nop");                                  //pulse elongation
 asm("nop");
 cbi(PORTC,lcd_en);                           //synchronizing pulse
 waitms(10L);
 sbi(PORTC,lcd_en);
 PORTC=(PORTC&0x0f)|((data&0x0f)<<4);         //prepares younger half-byte for
LCD
 asm("nop");
 asm("nop");
 cbi(PORTC,lcd_en);                           //synchronizing pulse
 waitms(10L);
}

void write_instr_lcd(data)                    //writes instruction to LCD
{
 cbi(PORTC,lcd_rs);                           //sets instruction mode
 write_to_lcd(data);
}

void write_char_lcd(data)                     //writes data to LCD
{
 sbi(PORTC,lcd_rs);                           //sets mode of data transfer
write_to_lcd(data);
}


void lcdxy(unsigned char line, unsigned char column)       //sets cursor
coordinates {
 write_instr_lcd((line*0x40+column)|0x80);     //instruction of setting the
cursor
}

void write_text (char *text)            //sends whole text to LCD
{
 char value;
 char nr = 0;
 value = pgm_read_byte(&text[nr]);
 while ((value!=0)&&(value!=10))
```

```
 {
  if(value==CR)
   {
      lcdxy(1,0);
      nr++;
      value = pgm_read_byte(&text[nr]);
   }
  else
   {
    write_char_lcd (value);
    nr++;
    value = pgm_read_byte(&text[nr]);
   }
 }
}

void clear_lcd(void)                        //clears the LCD
{
 write_instr_lcd(0x01);                     //sends clearing instruction
 waitms(2*tau);                             //required delay >1,64ms
 line=0;
 column=0;
 lcdxy(0,0);
}

int LCD_busy (void) {                       // tests the busy bit of the LCD
Display
 int input;
 input=0;
 DDRC|=0x0E;
 sbi(PORTC,lcd_rw);
 sbi(PORTC,lcd_en);
 input = PINC&128;
 DDRC|=0xfe;
 cbi(PORTC,lcd_rw);
 return (input==128);                       // true if busy set !
}

void lcd_init(void)                               //LCD initialization
{
 unsigned int i;
 DDRC|=0xfe;
 cbi(PORTC,lcd_rw);
 waitms(255*tau);
 for(i=0;i<3;i++)
 {
  sbi(PORTC,lcd_en);
  PORTC=(PORTC&0x0f)|0x30;
  asm("nop");                                     //pulse elongation
  asm("nop");
  cbi(PORTC,lcd_en);
  waitms(5*tau);
 }
 sbi(PORTC,lcd_en);
 PORTC=(PORTC&0x0f)|0x20;
 asm("nop");                                      //pulse elongation
 asm("nop");
 cbi(PORTC,lcd_en);
 waitms(10L);
 write_instr_lcd(0x28);
 write_instr_lcd(0x08);
```

```
 write_instr_lcd(0x01);
 waitms(5*tau);
 write_instr_lcd(0x06);
 write_instr_lcd(0x0f);
}



//************************** PULSE GENERATOR **************************

// SILNIK 1 OC0

void motor1_init(void)
{
 PORTA|=0xC0;                              //sets CTL/CW/FULL/RST(for FULL-step
set 0x80)
// sbi(PORTB,0);                     //sets EN
 DDRA|=0xe1;                               //port direction for CTL/CW/FULL/RST
 DDRB|=0x09;                               //port direction for EN/OC0
}

// SILNIK 1 OC2

void motor2_init(void)
{
 PORTD|=0x60;                              //sets CTL/CW/FULL/RST (for FULL-step
set 0x40)
// sbi(PORTC,0);                     //sets EN
 DDRD|=0xF8;                               //port direction for
OC2/CTL/CW/FULL/RST
 sbi(DDRC,0);                              //port direction for EN
}

void pulse1(float FLOW1)
{
 int accu;
 FLOW1=FLOW1*4*2*calib;              //scaling & calibration factors
 if(FLOW1>3)
  {
   if(FLOW1<9)
    {
       sbi(PORTB,0);
       TCNT0=0x00;
       accu=TCNT2;
       if(TCCR0!=0x1C)
        {
         TCCR0=0x1C;                 //sets prescaler to 256
         sbi(SFIOR,0);
        }
       OCR0=515/FLOW1-1;
       TCNT2=accu;
    }
   else
    {
       if(FLOW1<65)
        {
       sbi(PORTB,0);
         TCNT0=0x00;
         accu=TCNT2;
         if(TCCR0!=0x1B)
          {
```

```
           TCCR0=0x1B;              //sets prescaler to 64
           sbi(SFIOR,0);
          }
       OCR0=2062/FLOW1-1;
         TCNT2=accu;
        }
       else
        {
         sbi(PORTB,0);
         TCNT0=0x00;
         accu=TCNT2;
         if(TCCR0!=0x1A)
          {
           TCCR0=0x1A;              //sets prescaler to 8
           sbi(SFIOR,0);
          }
       OCR0=16500/FLOW1-1;
         TCNT2=accu;
        }
    }
  }
 else
  {
   if(FLOW1>1)
      {
       sbi(PORTB,0);
       TCNT0=0x00;
       accu=TCNT2;
       if(TCCR0!=0x1D)
        {
         TCCR0=0x1D;                //sets prescaler to 1024
         sbi(SFIOR,0);
        }
     OCR0=129/FLOW1-1;
       TCNT2=accu;
      }
   else
    cbi(PORTB,0);
  }
}

void pulse2(float FLOW2)
{
 int accu;
 FLOW2=FLOW2*4*2*calib;             //scaling & calibration factors
 if(FLOW2>5)
  {
   if(FLOW2<17)
    {
     sbi(PORTC,0);
       TCNT2=0x00;
       accu=TCNT0;
       if(TCCR2!=0x1D)
        {
         TCCR2=0x1D;                //sets prescaler to 128
         sbi(SFIOR,1);
        }
     OCR2=1031/FLOW2-1;
       TCNT0=accu;
    }
   else
```

```
    {
       if(FLOW2<65)
       {
      sbi(PORTC,0);
        TCNT2=0x00;
        accu=TCNT0;
        if(TCCR2!=0x1B)
         {
          TCCR2=0x1B;                //sets prescaler to 32
          sbi(SFIOR,1);              //prescaler reset
         }
      OCR2=4125/FLOW2-1;
        TCNT0=accu;
       }
       else
       {
        sbi(PORTC,0);
        TCNT2=0x00;
        accu=TCNT0;
        if(TCCR2!=0x1A)
         {
          TCCR2=0x1A;                //sets prescaler to 8
          sbi(SFIOR,1);              //prescaler reset
         }
      OCR2=16500/FLOW2-1;
        TCNT0=accu;
       }
    }
  }
 else
  {
   if(FLOW2>0.5)
      {
       sbi(PORTC,0);
       TCNT2=0x00;
       accu=TCNT0;
       if(TCCR2!=0x1F)
        {
         TCCR2=0x1F;                 //sets prescaler to 1024
         sbi(SFIOR,1);               //prescaler reset
        }
     OCR2=129/FLOW2-1;
       TCNT0=accu;
      }
   else
        cbi(PORTC,0);
  }
}

//************************* KEYBOARD - LCD MENU ***********************
int key(void)
{
 unsigned int state1=0, state2=0;
 while((state1!=state2)|(state1==0))
 {
   state1=0;
   state2=0;
   state1=~(PINA)&0x1e;
   waitms(10*tau);
   state2=~(PINA)&0x1e;
 }
```

```
 return(state1);
}

void shift_left(void)
{
 if(column>4)
  {
   column-=6;
   lcdxy(1,column);
  }
}

void shift_right(void)
{
 if(column<10)
  {
   column+=6;
   lcdxy(1,column);
  }
}

int decrease(void)
{
 if((ver2==1)&&(param>-50))
  param-=1;
 if((ver2!=1)&&(param>0))
  param-=1;
}

int increase(void)
{
  if(param<50)
  param+=1;
}

void menu2(void)
{
 int c=1;
 int d=0;
 int zn10,zn1;
 clear_lcd();
 char *text4=PSTR("Start: Flow Rate");
 char *text5=PSTR("Step:  Flow Rate");
 char *text6=PSTR("Number of Steps:");
 char *text12=PSTR("Set Flow Rate...");
 char *text13=PSTR("Obtained Volume?");
 char *text14=PSTR("mL");
 char *text15=PSTR("Please Wait...");
 char *text7=PSTR("mL/min");
 if((ver2==3)||(ver2==4))
  param=table[0][0];
 else
  param=table[ver1][ver2];
 while(c)
  {
   lcdxy(0,0);
   switch(ver2)                     // Option (header) display
    {
     case 0:
      {
       write_text(text4);
```

```
            break;
         }
        case 1:
         {
          write_text(text5);
            break;
         }
        case 2:
         {
          write_text(text6);
            break;
         }
          case 3:
         {
          write_text(text12);
            break;
         }
        case 4:
         {
          write_text(text13);
            break;
         }
       }

      lcdxy(1,3);
      zn10=param/10;
      zn1=param%10;
      if(param<0)                     // displays "-" if step is negative
         {
          zn10=zn10*-1;
        zn1=zn1*-1;
          write_char_lcd(0x2D);
         }
      else
       write_char_lcd(0x20);                // clears "-" if number is positive
      write_char_lcd(zn10+0x30);
      write_char_lcd(zn1+0x30);
      lcdxy(1,9);

      switch(ver2)                    // Unit display
         {
          case 4:
         {
            write_text(text14);
            break;
           }
          case 2:
           {
            break;
         }
        default:
           {
            write_text(text7);
            break;
           }
         }


      switch(key())                   // Option selection (click)
       {
        case back:
```

```
      {
       c=0;
       break;
      }
     case left:
      {
       decrease();
       break;
      }
     case right:
      {
       increase();
       break;
      }
     case enter:
      {
         switch(ver2)
          {
             default:
              {
               table[ver1][ver2]=param;
               c=0;
               break;
              }
           case 3:
            {
           table[1][0]=param;      //********* CALIBRATION **********
               pulse1(table[0][0]);
           motor1_init();
               clear_lcd();
               write_text(text15);
               OCR1AH=0x3D;
           OCR1AL=0xA6;
           TCCR1B=0x0B;
           while(d<60)
                if((TIFR&0x10)==0x10)
                  {
                 sbi(TIFR,4);
                 d++;
                  }
               cbi(PORTB,0);
               cbi(PORTC,0);
               ver2=4;
               break;
              }
             case 4:
              {
               calib=table[0][0]/param;
               c=0;
               break;
              }
             }
       break;
      }
   }
  }
}


void menu1(void)
{
```

```
 int b=1;
 char *text2=PSTR("Pump1:|Start Step  No. ");
 char *text3=PSTR("Pump2:|Start Step  No. ");
 char *text10=PSTR("Configuration:|Auto Man. Calib.");
 char *text11=PSTR("Auto Mode Set...");
 char *text12=PSTR("Manual Mode Set.");
 clear_lcd();

while(b)
{
 switch(ver1)
  {
   case 0:
    {
     write_text(text2);
     lcdxy(1,column);
       break;
    }
   case 1:
    {
     write_text(text3);
     lcdxy(1,column);
       break;
    }
   case 2:
    {
       write_text(text10);
     lcdxy(1,column);
       break;
    }
  }
 switch(key())
 {
 case back:
 {
  b=0;
  break;
 }
 case left:
 {
  shift_left();
  break;
 }
 case right:
 {
  shift_right();
  break;
 }
 case enter:
 {
  switch(column)
   {
    case 0:
       {
       if(ver1==2)
        {
        mode=1;                     // selection of operation Auto MODE
        clear_lcd();
        write_text(text11);
        waitms(3000);
        clear_lcd();
```

```
        }
       else
        {
         ver2=0;
         menu2();
         clear_lcd();
      }
       break;
       }
    case 6:
       {
       if(ver1==2)                       // selection of operation Manual MODE
        {
        mode=0;
        clear_lcd();
        write_text(text12);
        waitms(3000);
        clear_lcd();
        }
       else
        {
         ver2=1;
         menu2();
         clear_lcd();
      }
       break;
       }
      case 12:
       {
        if(ver1==2)
         {
          ver2=3;
            menu2();
          clear_lcd();
         }
        else
         {
          ver2=2;
          menu2();
          clear_lcd();
         }
       break;
       }
   }
  break;
 }
 }
}
}


void menu(void)
{
 int a = 1;
 char *text1=PSTR("Menu:|Pump1 Pump2 Conf");
 clear_lcd();
while(a)
{
 lcdxy(0,0);
 write_text(text1);
```

```
 lcdxy(1,column);
 switch(key())
 {
 case back:
  {
   a=0;
   break;
  }
 case left:
  {
  shift_left();
  break;
  }
 case right:
  {
  shift_right();
  break;
  }
 case enter:
  switch(column)
   {
    case 0:
       {
       ver1=0;
       menu1();
       clear_lcd();
       break;
//     FLOW1=FLOW;
       }
    case 6:
       {
       ver1=1;
       menu1();
       clear_lcd();
       break;
//     FLOW2=FLOW;
       }
      case 12:
       {
       ver1=2;
       menu1();
       clear_lcd();
       break;
       }
   }
 }
}
}

SIGNAL(SIG_INTERRUPT0)
{
 int flowr1;
 int flowr2;
 char *text8=PSTR("Initialized...");
 char *text17=PSTR("Stopped...");
 clear_lcd();
 if(interrupt<(0x01+table[1][2]))
  {
   write_text(text8);
   flowr1=table[0][0]+table[0][1]*interrupt;   // Start value + Step * interrupt
   flowr2=table[1][0]+table[1][1]*interrupt;
```

```
   pulse1(flowr1);
   pulse2(flowr2);
   sbi(PORTB,0);
   sbi(PORTC,0);
  }
 else
  {
   write_text(text17);
   cbi(PORTB,0);
   cbi(PORTC,0);
  }
 interrupt++;
}

int main(void)
{
// sbi(GICR,6); do przerwan
 int stop;
 MCUCR=0x02;
 PORTA|=0x1e;
 DDRA&=~0x1e;
 sbi(PORTD,2);                     // triggering by robot
 cbi(DDRD,2);                            // triggering by robot
 cbi(PORTB,0);
 sbi(DDRB,0);
 cbi(PORTC,0);
 sbi(DDRC,0);
 char *text6=PSTR("GO!!");
 char *text16=PSTR("Waiting for|          Robot");
 char *text8=PSTR("Initialized...");
 char *text17=PSTR("Stopped...    ");
 sbi(MCUCSR,7);                    // disable JTAG debug interface
 lcd_init();
  while(1)
  {
   menu();
   interrupt=0;
   if(mode==0)
   {
    pulse1(table[0][0]);
    pulse2(table[1][0]);
    motor1_init();
    motor2_init();
    clear_lcd();
    write_text(text6);
      if(key()==back)
     {
      cbi(PORTB,0);
      cbi(PORTC,0);
     }
   }
   else
    {
       clear_lcd();
       motor1_init();
     motor2_init();
       cbi(PORTB,0);
     cbi(PORTC,0);
       stop=0;
       clear_lcd();
       while(stop==0x00)
```

```
       {
        if((~(PIND)&0x04)==0x04)
         {
          lcdxy(0,0);
          write_text(text8);
          pulse1(table[0][0]);
        pulse2(table[1][0]);
         }
        else
         {
          lcdxy(0,0);
          write_text(text17);
          cbi(PORTB,0);
        cbi(PORTC,0);
         }
        if((~(PINA)&0x1e)==back)
         {
          waitms(10*tau);
            if((~(PINA)&0x1e)==back)
             stop=0x01;
             cbi(PORTB,0);
         cbi(PORTC,0);
         }
       }
    }
   }
}
```

Available online at www.sciencedirect.com

SCIENCE DIRECT®

Surface & Coatings Technology 201 (2006) 45 – 56

SURFACE & COATINGS TECHNOLOGY

www.elsevier.com/locate/surfcoat

Microstructural characterization of plasma sprayed TiO_2 functional coating with gradient of crystal grain size

R. Tomaszek [a], L. Pawlowski [a,*], L. Gengembre [b], J. Laureyns [c], Z. Znamirowski [d], J. Zdanowski [d]

[a] *Service of Thermal Spraying at Ecole Nationale Supérieure de Chimie de Lille, BP 90108, F-59652 Villeneuve d'Ascq, France*
[b] *Laboratory of Catalyse of Lille at University of Science and Technology of Lille, F-59655 Villeneuve d'Ascq, France*
[c] *Laboratory of Infrared and Raman Spectrochemistry at University of Science and Technology of Lille, F-59655 Villeneuve d'Ascq, France*
[d] *Faculty of Microsystems Electronics and Photonics at Wroclaw University of Technology, Pl-50-372 Wroclaw, Poland*

Received 31 May 2005; accepted in revised form 25 October 2005
Available online 5 December 2005

Abstract

The paper aims at development of a coating with a gradient in grain size. A first layer was deposited directly onto stainless steel substrate by plasma spraying of a coarse TiO_2 powder. This layer had thickness in the range from 30 to 50 μm. A second layer was deposited on the first one using plasma spraying of different aqueous suspensions of two TiO_2 pigments. The layer had thickness smaller than 10 μm. Morphologies of TiO_2 powder and pigments were characterized using a scanning electron microscope (SEM) and their sizes were tested with a laser sizer. Phase analysis of powder and pigments, made by X-ray diffraction (XRD), enabled only rutile phase to be discovered. A mixture of rutile and anatase was found in the suspension sprayed coatings. The presence of anatase in sprayed coatings was an interesting and original result, which was also confirmed by Raman spectroscopy. The formation of this phase was tentatively explained by a high cooling rate of small splats. The suspension plasma spraying was optimized in order to obtain homogeneous and dense deposits. The morphology of sprayed coatings was characterized using SEM. Crystal grain sizes were estimated using XRD. The sizes were in the range of a few tenths to one hundred nanometers in the initial powders. They were clearly smaller in the coatings sprayed using coarse powder but remained quite similar in suspension sprayed layers. Finally, X-ray photoelectron spectroscopy (XPS) was used to analyze quantitatively the chemical composition of powders and coatings.

Keywords: Suspension plasma spraying; Atmospheric plasma spraying; TiO_2 coatings; XRD phase analysis; Raman spectroscopy; Thermally sprayed coatings microstructure; XPS chemical analysis

---

1. Introduction

TiO_2 is an oxide having a lot of applications such as, e.g.:

- Coloring agent in mixture for painting;
- Support for catalysis;
- High permittivity dielectrics in capacitors;
- Oxygen sensor;
- Coating for wavelength dependent optical transmission.

The material is often used as a thin film deposited by PVD or as a thick coating obtained by thermal spraying [1,2]. Among the emerging applications of the latter, two seem to be studied intensively at present:

- Photocatalytic coatings [2–6];
- Electronic emission coatings [7,8].

The photocalytic activity seems to be promoted mainly by an appropriate phase composition of coatings. The coating should possibly include anatase phase. The tested coatings were prepared by vacuum or atmospheric plasma spraying (APS) of powders and by atmospheric plasma spraying of suspension [3–6]. The coatings for electronic emission were prepared using TiO_2 pure and alloyed with Al_2O_3 by APS. Some of them were submitted to post spray laser treatment. The principal microstructural feature determining electronic field emission was the size of conducting grains [9]. Small size of the grains

---

* Corresponding author. Tel.: +33 320 33 61 65; fax: +33 320 33 61 65.
E-mail address: lech.pawlowski@ensc-lille.fr (L. Pawlowski).

0257-8972/$ - see front matter © 2005 Elsevier B.V. All rights reserved.
doi:10.1016/j.surfcoat.2005.10.033